

Copyright  
by  
Erin Colleen Rericha  
2004

The Dissertation Committee for Erin Colleen Rericha  
certifies that this is the approved version of the following dissertation:

## **Shocks in Rapid Granular Flows**

Committee:

---

Harry L. Swinney, Supervisor

---

Ernst-Ludwig Florin

---

Irena Gamba

---

William McCormick

---

Jack Swift

# Shocks in Rapid Granular Flows

by

Erin Colleen Rericha, B.S.

## DISSERTATION

Presented to the Faculty of the Graduate School of  
The University of Texas at Austin  
in Partial Fulfillment  
of the Requirements  
for the Degree of

## DOCTOR OF PHILOSOPHY

THE UNIVERSITY OF TEXAS AT AUSTIN

August 2004

Dedicated to Harry L. Swinney - I better advisor is unimaginable.

## Acknowledgments

While in graduate school, I have had the great fortune to study at the Center for Nonlinear Dynamics under the guidance of my advisor Harry Swinney. The CNLD is a special place full of collaborative, friendly people all striving for excellence in science. I feel privileged to be a member. I would like to thank the many people of the physics department and center who have been so helpful through the years. I owe a debt of gratitude to John DeBruyn whom I met at the Science Fair and who arranged for me to join the CNLD. Mark Shattuck and Chris Bizon were my mentors and coauthors during my first two years in the center. I had great fun working with Patrick Heil, Florian Merkt and Robert Deegan during my last two years at the center. Dan Goldman has been a friend and example through these years. I hope his enthusiasm, discipline, and persistence will be contagious to all who work with him. Thank you to Jon Bougie, Jenn Kreft, Matt Lane and Matthias Schroeder for all the fruitful discussions. I look forward to many more collaborations. I would like to especially thank Jack Clifford for his advice in assistance in building the experiments as well as being a great friend.

Outside of physics, I am blessed with a supportive and grounding family and friends. Thank you for all of your encouragement and patience. I would like to thank Jeff Van Dyke who helped in every possible way towards the

completion of this work from running errands to the occasional much needed poking to get me back to work. His company has made my experience better and brings me a new optimism for the future.

Finally, no student could ever have a better advisor than Harry Swinney. I am grateful for his quiet leadership, endless support, and continual example for the correct way to pursue science.

# Shocks in Rapid Granular Flows

Publication No. \_\_\_\_\_

Erin Colleen Rericha, Ph.D.  
The University of Texas at Austin, 2004

Supervisor: Harry L. Swinney

The speed of a pressure wave (the speed of sound) in rapid granular flows is typically only a few centimeters per second while the collective streaming motion of the particles is on the order of meters per second. In this supersonic regime, shocks form when a granular flow encounters an obstacle. This work examines the shocks formed in three geometries: the surface wake behind a cylinder, the oblique shock formed at a wedge and a normal shock propagating through a funnel. In each case we evaluate the applicability of a hydrodynamic description to shocks in rapid granular flows.

We study the V-shaped wake formed by a cylindrical rod moving through a vertically vibrated granular layer. The wake appears for rod velocities  $v_R$  greater than a critical velocity  $c$ . We measure the half-angle  $\theta$  of the wake as a function of  $v_R$  and layer depth  $h$ . We find that  $c$  and  $\theta$  can be described by a hydrodynamic description applied to shallow fluids, where  $c = \sqrt{gh}$  is the speed of a gravitational wave on a shallow fluid and  $\sin\theta = c/v_R$  is the Mach

relation. We find the decrease in the height of the wake  $h_{max}$  as it propagates away from the rod agrees with Landau's theory for the decay of shock waves far from their origin.

We measure the time-averaged velocity, density and temperature fields for a gravity driven granular flow past a wedge. The flow is supersonic with a sound speed less than 10% of the flow speed. We find the shock formed at the wedge tip is nearly identical to oblique shocks found in a supersonic, elastic gas. Molecular dynamics simulations of Newton's laws yield fields in quantitative agreement with experiment. A numerical solution of granular hydrodynamic equations is only in qualitative accord with experiment. We show that hydrodynamic theory fails because it does not include friction. We use molecular dynamics simulations to examine the effect of friction on the dissipation of energy and scattering angles in collisions.

We examine the propagation of a normal shock formed in a quasi-two dimensional funnel. For shocks propagating without change in a fluid, one can use the Rankine-Hugoniot approximation to predict the velocity of the shock and the difference in flow values across the shock. We show that inelastic collisions between particles cause the shock to continuously evolve, hence the Rankine-Hugoniot predictions are inadequate for describing the evolution of granular shocks.



# Table of Contents

|   |            |
|---|------------|
| <b>Acknowledgments</b>                                      | <b>v</b>   |
| <b>Abstract</b>   | <b>vii</b> |
| <b>List of Figures</b>                                      | <b>xii</b> |
| <b>Chapter 1. Introduction</b>                              | <b>1</b>   |
| 1.1 Motivation . . . . .                                    | 1          |
| 1.2 Overview of the Dissertation . . . . .                  | 2          |
| 1.3 Why shocks? . . . . .                                   | 4          |
| <b>Chapter 2. Review of Granular Flow Phenomena</b>         | <b>10</b>  |
| 2.1 Static Granular Materials . . . . .                     | 11         |
| 2.2 Experimental Granular Flows . . . . .                   | 12         |
| 2.2.1 Sheared Flows . . . . .                               | 12         |
| 2.2.2 Rotated Flows . . . . .                               | 13         |
| 2.2.3 Vibrated Flows . . . . .                              | 14         |
| 2.3 Shock Waves in Granular Materials . . . . .             | 16         |
| 2.4 Multiphase Flows . . . . .                              | 19         |
| 2.5 Molecular Dynamics Simulations . . . . .                | 19         |
| 2.6 Continuum Description . . . . .                         | 21         |
| 2.7 Jenkins and Richman Equations . . . . .                 | 26         |
| <b>Chapter 3. Wake Behind a Cylinder in a Granular Flow</b> | <b>32</b>  |
| 3.1 Abstract . . . . .                                      | 32         |
| 3.2 Introduction . . . . .                                  | 32         |
| 3.3 Experiment . . . . .                                    | 34         |
| 3.4 Results . . . . .                                       | 37         |
| 3.5 Shallow water theory . . . . .                          | 40         |

|                                     |   |           |
|-------------------------------------|---|-----------|
| 3.6                                 | Shock Decay . . . . .                   | 44        |
| 3.7                                 | Time Dependence . . . . .               | 49        |
| 3.8                                 | Conclusions . . . . .                   | 51        |
| <b>Chapter 4. Methods</b>           |   | <b>52</b> |
| 4.1                                 | Flow Past a Wedge Apparatus . . . . .   | 52        |
| 4.1.1                               | Particles . . . . .                     | 54        |
| 4.1.2                               | Hele-Shaw Cell . . . . .                | 54        |
| 4.1.3                               | Distribution . . . . .                  | 56        |
| 4.1.4                               | Lighting . . . . .                      | 57        |
| 4.1.5                               | Vacuum Apparatus . . . . .              | 58        |
| 4.2                                 | Particle Tracking . . . . .             | 59        |
| 4.2.1                               | Finding centers . . . . .               | 60        |
| 4.2.2                               | Determining Velocities . . . . .        | 63        |
| 4.2.3                               | Building average flow fields . . . . .  | 65        |
| 4.3                                 | Molecular Dynamics Simulation . . . . . | 71        |
| 4.4                                 | Continuum Equation Solver . . . . .     | 75        |
| 4.4.1                               | Boundary Conditions . . . . .           | 76        |
| <b>Chapter 5. Flow Past A Wedge</b> |   | <b>79</b> |
| 5.1                                 | Abstract . . . . .                      | 79        |
| 5.2                                 | Introduction . . . . .                  | 79        |
| 5.3                                 | Experiment . . . . .                    | 81        |
| 5.4                                 | Friction . . . . .                      | 90        |
| 5.4.1                               | Air Friction . . . . .                  | 91        |
| 5.4.2                               | Wall Friction . . . . .                 | 92        |
| 5.4.3                               | Inter-Particle Friction . . . . .       | 92        |
| 5.5                                 | Conclusion . . . . .                    | 95        |

|   |            |
|---|------------|
| <b>Chapter 6. Normal Shock Propagation in a Funnel</b>              | <b>97</b>  |
| 6.1 Abstract . . . . .  | 97         |
| 6.2 Introduction . . . . .  | 97         |
| 6.3 Normal shock propagation . . . . .                              | 102        |
| 6.4 Hugoniot-Rankine Approximation . . . . .                        | 105        |
| 6.5 Analytical Solution of a set of Inelastic Continuum Equations . | 109        |
| 6.6 Discussion . . . . .  | 112        |
| <b>Chapter 7. Conclusions and Suggestions for Future Work</b>       | <b>113</b> |
| 7.1 Wake Behind a Cylinder . . . . .                                | 114        |
| 7.2 Granular flow past a wedge . . . . .                            | 115        |
| 7.2.1 gap thickness . . . . .                                       | 115        |
| 7.2.2 boundary conditions . . . . .                                 | 116        |
| 7.2.3 higher dissipation . . . . .                                  | 116        |
| 7.3 Normal shock propagation in a funnel . . . . .                  | 117        |
| 7.4 velocity distributions . . . . .                                | 117        |
| 7.5 Conclusions . . . . .   | 118        |
| <b>Appendix</b>   | <b>119</b> |
| <b>Appendix 1. Shallow Water Equations</b>                          | <b>120</b> |
| <b>Bibliography</b>   | <b>125</b> |
| <b>Vita</b>   | <b>142</b> |

## List of Figures

|     |   |    |
|-----|---|----|
| 1.1 | <p><b>a)</b> Sand in an open container behaves as a liquid taking on the shape of the container. The surface can support some stress.</p> <p><b>b)</b> When the beaker is tilted, the sand flows out of the beaker resembling a fluid. The granular flow is <i>supersonic</i>: the mean flow velocity is greater than the speed of a pressure wave. When the sand hits the surface, inelastic collisions quickly dissipate energy and the sand forms a weak solid. . . . .</p>  | 5  |
| 1.2 | <p>Molecular dynamics simulation of a granular flow through a quasi 2D cell. The mean values of <b>a)</b> Temperature and <b>b)</b> Mach number are plotted versus distance from the bottom of the cell. Particles were injected into the top of the cell, <math>y = 300\sigma</math>, with an initial velocity chosen from a Gaussian distribution centered at <math>V_y</math>. The width of the distribution corresponds to the flows temperature. As the particles collide inelastically, <math>e = 0.97</math>, but without friction <math>\mu = 0</math> the temperature is dissipated and the sound speed decreases. Within 10 particle diameters the Mach number is greater than 1. . . . .</p> | 7  |
| 1.3 | <p>Molecular Dynamics simulation of elastic, frictionless particles interacting with an obstacle (<math>g=0</math>). The flow is incident onto a wedge with <math>M = 2.5</math>. Impenetrable boundary conditions at the surface of the wedge require the flow streamlines to be parallel. The interface between the incident and deflected flow is a shock, where the streamlines change. Behind the shock the flows volume fraction, temperature and pressure are greater than in front of the shock. . . . .</p>  | 9  |
| 2.1 | <p>An initially uniform mixture of glass beads of three sizes [0.5 mm (blue), 1 mm (gold), 2 mm (red)] segregated into bands. The particles were rotated about an axis perpendicular to gravity at 30 rpm for several hours [88]. . . . .</p>   | 14 |
| 2.2 | <p>Standing wave patterns in vertically vibrated granular layers: (a) stripes, (b) squares, and (c) hexagons. White corresponds to high points of the surface and black to low points. The patterns oscillate at half of the driving frequency [118]. . . . .</p>   | 15 |

|     |   |    |
|-----|---|----|
| 2.3 | Shock formation and propagation in an oscillated granular layer. The dimensionless temperature $T/g\sigma$ and volume fraction $\nu$ are plotted as functions of the dimensionless height $z/\sigma$ at four times $ft$ in the oscillation cycle. For each time, a snap shot from the MD simulation is shown in the left column with individual particles color coded according to temperature: high T in red, low T in blue, and the bottom plate of the container shaded solid gray. The right column shows the horizontally averaged $\nu$ (blue) and $T/g\sigma$ (red) for the same four times. The plate is shown as a horizontal black solid line, results from MD simulations are shown as dots, and continuum results are solid lines (From [14]) | 18 |
| 2.4 | Top view of a vibrated aqueous suspension of cornstarch (a-c) or glass spheres (d-f). Each image has a diameter of 9.4 cm. White corresponds to high points of the surface and black to depressions that reach near the container bottom. The layer depth is 0.5 cm for the cornstarch suspension and 0.2 cm for the glass suspension. For high forcing frequencies stable holes occur without Faraday waves: (a) acceleration amplitude $a = 12g$ , $f = 150$ Hz; (d) $30g, 100$ Hz. At lower frequencies stable holes are accompanied by the Faraday patterns: (b) $12g, 60$ Hz; (e) $27.3g, 92$ Hz. Delocalized state: (c) $30g, 120$ Hz; (f) $30g, 60$ Hz [81] . . . . .  | 20 |
| 2.5 | Forced granular materials produce qualitatively similar patterns as forced fluids: (a) stripe pattern formed by a vertically oscillated granular layer [80], (b) stripe pattern formed by a vertically oscillated layer of water [68], (c) stripe pattern formed in thermal convection of a fluid ( $CO_2$ ) [95]. . . . .  | 23 |
| 2.6 | Instabilities of patterns found in oscillating granular layers and Rayleigh-Bénard convection in a fluid. Cross roll instability in stripes: (A) Vibrated granular layer [31] and (a) Rayleigh-Bénard convection [20]. Skew varicose instability in stripes: (B) Granular layer [31] and (b) Rayleigh-Bénard convection [6]. Spiral defect chaos in: (C) vibrated granular layer [32] and (c) Rayleigh-Bénard convection [6]. . . . .   | 25 |
| 2.7 | Vibrated granular layers (A-D) [45] display coherent motion below the onset of patterns similar to the fluctuating thermal noise observed in Rayleigh-Bénard convection (a-d) [131]. Below onset, snapshots of the system below (A and a) and above (B and b) show no long range order but the modulus of the corresponding fourier transform (C and c) and (D and d) indicate each system fluctuates within a ring in phase space. Above onset, the intensity of the coherent motion increases and orientational emerges. . . . .  | 27 |

|     |  |    |
|-----|--|----|
| 3.1 | The dependence of the wake half-angle $\theta$ on the velocity of an object, $v_R$ , traveling through a surface-tensionless fluid of finite depth $h$ [53]. For $v_R < \sqrt{gh}$ , both transverse and diverging waves contribute to the wake leading, to the Kelvin wedge pattern (left inset). For $v_R > \sqrt{gh}$ , the transverse waves are not resonantly excited. A superposition of diverging waves leads to the formation of a shock (right inset). The opening angle decreases with increasing $v_R$ . . . . .  | 33 |
| 3.2 | The granular layer is confined in a plexiglass container (17.75 cm in diameter and 10.7 cm tall) with an aluminum base. A motor is attached to a plexiglass disk through a rotary motion feedthrough. A stainless steel rod is suspended from the disk at a radius of 5.1 cm. The motor spins the disk such that the rod moves with a constant speed $v_R$ in the range of 4-30 cm/s. Outside of the container, a thick aluminum plate also rotates with the rod. On each rotation the aluminum plate passes through a photo diode, triggering the CCD camera to record 52 images of the layer. . . . .  | 35 |
| 3.3 | The granular layer is vibrated by an electromagnetic shaker. The shaker is attached to the container via a 2.54 cm square air bearing. The bearing minimizes both rotational and horizontal motion, so the container is only forced vertically. The system is sensitive to the tilt of the container. The air bearing rests on an aluminum plate which is suspended above an air table. We adjust the length of the wires until the layer inside the container remains level while being shaken. . . . .   | 36 |
| 3.4 | (a) Schematic of the laserline scanning technique used to measure the displacement of the surface created by a rod moving through a granular layer. The rod travels in a circular path of $r = 5.1$ cm. A laser light sheet is incident downward onto an initially flat granular surface. When the rod passes through the laser line it triggers a CCD camera, held at a fixed angle with respect to the flat surface, that captures 52 digital images of the laser line separated in time by $\delta\tau = 2.2$ ms. For $v_R = 21.5$ cm/s, the distance between line scans is $\delta x = v_R * \delta\tau = 0.47$ mm. The inset shows an average over 400 periods of the rod motion. The location of the laser line is determined to subpixel accuracy by finding the center of a Gaussian fit to each vertical slice as shown in the inset (red line). The wake is a 3D reconstruction of the averaged laser lines. (b) The top view of the shock created by the rod, moving to the right, for $v_R = 21.5$ cm/s. The location of the maximum positive displacement for each laser line is indicated by the dots. A linear fit to the maxima (blue) reveals the wake's asymptotic half angle $\theta$ . . . . . | 38 |

|      |  |    |
|------|--|----|
| 3.5  | The maximum upward displacement of the layer determined from height profiles along the dashed line in Fig. 3.4 (b) behind the rod as a function of rod velocity for layer depth $h=4\sigma$ . For small $v_R$ the layer behind the rod remains flat to within experimental accuracy (dotted line). Above a critical velocity the deflection increases linearly (dashed line). The intersection of the dashed line with the horizontal axis indicates a non zero critical velocity. The noise level was determined by the peak to peak oscillations in the flat part of the layer. . . . .  | 39 |
| 3.6  | The dependence of the half-angle $\theta$ of the shock cone on $v_R$ . The ordinate is scaled so that a sinusoidal dependence yields a straight line. The slope yields the wave speed, $c$ . Inset shows dependence of $c$ on the layer depth $h$ . The error includes uncertainty in the depth due to leveling of the container (horizontal error bars) and uncertainty in the algorithm determining the angle (vertical error bars). The solid line is the prediction from shallow water theory, $c = \sqrt{gh}$ . . . . .   | 41 |
| 3.7  | Space-time plot of the horizontally averaged flow fields for (a) Temperature and (b) volume fraction from a MD simulation of a vertically vibrated granular layer ( $\Gamma = 2.2$ , $f^* = 0.39$ , $h = 4\sigma$ ). Each horizontal line shows the averaged field as a function of height in the cell. The crystal ordering of particles can be seen in the volume fraction curve. Red indicates high values of the field; blue indicates low values. For $t = 0$ the layer begins colliding with the plate (solid white line). Near the plate a compression shock forms, compressing and heating the grains. By $t = 0.25\tau$ , the shock has traveled through the layer. For the remainder of the cycle, the layer moves with respect to the plate, but the temperature and density profile do not change significantly. . . . . | 43 |
| 3.8  | The maximum height of the shock front as a function of $r$ , the distance from the shock front to the rod's axis of motion. The amplitude of the cylindrical sound waves excited by the rod decay as $1/\sqrt{r}$ , where $r$ is the radial distance from the origin of the wave. The shock formed by the coalescence of these waves does not extend into the fluid indefinitely, but decays as $r^{-3/2}$ . . . . .   | 44 |
| 3.9  | A shock profile propagating through a fluid can not be multi-valued. Instead, a discontinuity forms at $x = x_0$ . The location of the discontinuity is such that the two shaded areas will be equal [71] . . . . .  | 45 |
| 3.10 | Decay of a shock discontinuity as it travels through a material. The area of the shaded triangles must be equal . . . . .  | 47 |

|      |   |    |
|------|---|----|
| 3.11 | High speed images of the wake. The white circles indicate the approximate position of the rod. Red indicates high points of the layer and dark blue indicates depressions. The vertical oscillation of the layer imposes an additional feature on the wake. With each oscillation the depressed region behind the rod collides with the plate and fills forming a small peak at $x = x_0$ . The peak remains stationary while the rod continues to move with $v_R$ . On the next oscillation with the plate the old peak is damped and a new one will form at $x = x_0 + v_R/f$ . . . . . | 50 |
| 4.1  | A snap-shot of the experimental apparatus. Particles fall past obstacles (in this image two wedges) confined between two glass plates. The Hele-Shaw cell is set in a large, aluminum box that can be evacuated. . . . .  | 53 |
| 4.2  | Schematic of the experimental cell: a) the Hele-Shaw cell is formed by two 1.27 cm thick glass plates. b) Cross section of the clamps . . . . .   | 55 |
| 4.3  | image of the conveyor belt . . . . .  | 56 |
| 4.4  | schematic of the hopper system . . . . .  | 57 |
| 4.5  | Image of a white sheet of paper taken with the Kodak Motion-corder camera. The pixel array is noisy, showing a 2 by 2 square pixel pattern of varying intensity. . . . .  | 60 |
| 4.6  | <b>(a)</b> A snap shot of the experimental. The image shows an area $35\sigma \times 34\sigma$ taken from the top and center of the cell. The flow is viewed in transmission, so that particles are dark. Unfortunately the camera has a noise pattern so the particles do not appear as solid disks nor as a Gaussian reflection. The center is not necessarily reflected by the darkest pixel. <b>(b)</b> A background subtracted snap shot shows a more regularly illuminated image.   | 61 |
| 4.7  | <b>a</b> An image of the average particle, $ip$ detected by the camera. This image is used to deconvolve the original images, yielding bright pixels at the center of each particle in the frame <b>b</b> . Subpixel resolution is determined by minimizing the difference between the actual image from an image created by $ip$ 's. . . .   | 63 |
| 4.8  | Location of the particle center determined at each of the three stages: $p_1$ green, $p_2$ black, and $p_3$ white. . . . .  | 64 |
| 4.9  | We match particles from one frame to another. Red are particles in the first frame. Blue particles in the second. Arrow connects the dots. Particles are allowed to come in and leave through all of the walls. . . . .   | 66 |
| 4.10 | Average vertical velocity flow field determined from time-averaged particle tracks. The image shows a $125\sigma \times 100\sigma$ region. . . . .  | 67 |



|      |  |    |
|------|--|----|
| 4.11 | <p><b>Top</b> zoomed in region on the exit of a funnel. The black regions correspond to portions of two wedges defining the funnel. The bottom of the wedges are separated by <math>12\sigma</math>. Near the opening of the funnel, the grains are in a crystal configuration. We compute the voronoi tessellation, such that each polygon defines the area closest to the particle contained within the polygon. The density of the flow inside a polygon is <math>1/\text{area}</math>. We average over many realizations of this flow to determine the average flow field. <b>Bottom</b> The average volume fraction field determined by the tessellation technique. . . . .</p> | 69 |
| 4.12 | <p>MD simulation results for the temperature, <math>T</math>, at the top and middle of a quasi-2D cell. We plot the dependence of the measured <math>T</math> on the number of particle velocities used to compute <math>T</math>. For number of particles, <math>N &lt; 8</math>, the recorded value of the temperature is incorrect. . . . .</p>   | 70 |
| 4.13 | <p>The coefficient of restitution is velocity dependent (figure from [50]). . . . .</p>  | 73 |
| 4.14 | <p>Velocity Distribution of particles within <math>2\sigma</math> of the wedge tip determined from MD simulation. The Gaussians fits are determined from the temperature and mean values in the free stream region near the tip. . . . .</p>   | 77 |
| 4.15 | <p>Temperature fields for a). molecular dynamics simulation and b). continuum equations. Each simulation handles the tip differently, leading to poor agreement in the vicinity of the wedge tip. . . . .</p>  | 78 |
| 5.1  | <p>MD simulation of a supersonic <i>elastic</i> gas interacting with a wedge of half angle <math>\theta = 20^\circ</math>. The flow is incident on the wedge with a Mach number of 2.5. Impenetrable boundary conditions at the surface of the wedge require the flow stream lines behind the shock to be parallel to the wedge surface. The shock extends outward into the fluid at an angle <math>\beta</math> with respect to the incident flow. . . . .</p>  | 80 |
| 5.2  | <p>The <math>\theta-\beta-Mach</math> relationship for elastic, oblique shocks. Figure taken from Anderson [5]. . . . .</p>  | 82 |
| 5.3  | <p>An observed image of granular flow incident downward on a wedge, where the particle positions and velocities (denoted by arrows) are determined from images separated by 1 ms. The longest arrow corresponds to a velocity of 1.65 m/s. The figure <math>68\sigma</math> by <math>45\sigma</math> shows the top <math>30\sigma</math> of a wedge of total height <math>100\sigma</math>. . . . .</p>  | 83 |

|      |   |    |
|------|---|----|
| 5.4  | Horizontal component of the velocity field of a granular flow incident downward on a wedge, determined by three methods: (a) experiment, (b) MD simulations, and (c) integration of inelastic continuum equations. (d) MD simulation of an elastic gas in a gravitational field is included for reference. Each picture shows a region $130\sigma$ by $104\sigma$ . The solid lines with arrows denote streamlines. Quantitative comparisons along the dashed line in (a) are shown in figs. 5.6 and 5.7 [101]. . . . . | 84 |
| 5.5  | The horizontal velocity field measured for the expansion fan that formed when the supersonic granular flow reached the bottom of the wedge. The solid lines indicate selected streamlines. The total height of the region shown is $55\sigma$ . The white region below the wedge had too few particles for the velocity to be determined [101]. . . . .   | 85 |
| 5.6  | Shock profiles for granular flow past a wedge measured in an experiment (circles) are compared with results from molecular dynamics (solid lines): (a) volume fraction, (b) horizontal component of the velocity, and (c) temperature. The profiles are taken along the dashed line in fig. 5.4 [101]. . . . .  | 86 |
| 5.7  | Comparison of shock profiles for granular flow past a wedge obtained from molecular dynamics (solid lines) and inelastic continuum equations (dotted line), assuming no friction. (a) Volume fraction, (b) horizontal velocity profile, and (c) temperature along the dashed line in fig. 5.4(a). Experimental measurements (open circles) show similar qualitative behavior but disagree quantitatively. The difference between the simulations and the experiment is due to wall friction [101]. . . . .              | 89 |
| 5.8  | Experimentally measured free stream vertical velocity versus vertical distance (blue dots). The top of the cell corresponds to $y=0$ . The solid red line is a fit to the experimental data yielding a downward acceleration of $8.9 \text{ m/s}^2$ . . . . .   | 90 |
| 5.9  | Distribution of the measured downward accelerations for particles in the experiment with gap thickness $1.6\sigma$ and atmospheric pressure (green), gap thickness $1.1\sigma$ atmospheric pressure (red) and $1.1\sigma$ at 4 Pa (blue) . The accelerations were determined by fitting tracks from particles in the top portion of the cell. Only particles with smooth (collisionless) tracks over a vertical distance $30\sigma$ were considered. . . . .  | 93 |
| 5.10 | MD simulations showing the dependence of the shock shape on inelasticity and friction. For elastic particles, the shock extends straight into the fluid at a constant angle with constant parameters behind the shock. Adding inelasticity and friction causes the shock to curve in towards the wedge. The dashed lines show the location of the comparisons in Fig. 5.11. . . . .   | 94 |

|      |   |     |
|------|---|-----|
| 5.11 | Shock profiles taken from MD simulation results of particles moving through a thin cell with no gravity and interacting with a wedge. We compare the volume fraction <b>a</b> , temperature <b>b</b> , Mach number <b>c</b> profiles along the horizontal dashed line in Fig. 5.10 for elastic, frictionless particles $e_0 = 1, \mu = 0$ (blue line), inelastic, frictionless particles $e_0 = 0.97, \mu = 0$ (red line), and inelastic frictional particles $e_0 = 0.97, \mu = 0.15$ (green line). The flow values behind the shock for elastic frictionless particles are constant. Inelastic collisions cause the flow parameters to evolve behind the shock – as the temperature is dissipated, the volume fraction increases and the Mach number increases. Adding friction increases the dissipation of energy and exacerbates the effects. In <b>d</b> we plot the Mach Number of the free stream flow taken along the vertical dashed line in Fig. 5.10. Adding inelasticity and friction to the particles causes the temperature in the free stream to be dissipated, increasing the Mach number. . . . .   | 96  |
| 6.1  | Schematic of oblique shocks (blue lines) interacting in a region between two wedges. The dashed lines with arrows indicate the direction of the flow streamlines. The initial flow is incident downwards. Behind the shocks the flow is deflected through an angle $\theta$ and the Mach number of the flow decreases. The flow is deflected again by $\theta$ in the region of shock interaction. The maximum allowed deflection angle by an oblique shock depends on the Mach number in the incident region (see Chapter 5.2, Fig. 5.2). If the Mach number in region 2 is large, then $\theta < \theta_{max}$ , the incident shock waves are refracted at the interaction region ( <b>A</b> ). If the Mach number is small such that $\theta$ is greater than $\theta_{max}$ , a normal shock forms at the interface of the interaction region ( <b>B</b> ). The vertical velocity field from an experimental granular flow through a funnel formed by two wedges is shown in ( <b>C</b> ). The bottom of the wedges were separated by $25\sigma$ . A normal shock forms at the interaction region. The flow behind the normal shock is hotter, denser, and slower than the incident flow. . . . . | 99  |
| 6.2  | Volume fraction fields from an MD simulation of granular flow in a funnel for $e_0 = 0.9$ . The average fields were calculated using the tessellation technique described in Methods. . . . .   | 100 |

|     |  |     |
|-----|--|-----|
| 6.3 | MD simulation results ( $e_0 = 0.97$ ) for the propagation of the volume fraction wave up the funnel. Each profile is the mean volume fraction at time along the center between the two wedges. (Time $\tau$ is measured in units of $\sqrt{\sigma/g}$ .) Dark dots indicate the location of the shock and open circles indicate the front of the crystalline region. The shaded region is the realm inside the funnel. . . . .  | 101 |
| 6.4 | (MD simulation, $e_0 = 0.9$ ) The location of the shock as a function of time as the normal shock propagates upwards in the funnel (blue dots). The solid blue line is a fit to the linear, constant profile region. The slope of the line indicates the velocity of the shock. The red open circles indicate the front location of the crystalline region behind the shock and the red line is a fit to the linear, constant region. The growth rate of the crystalline region is equal to the shock velocity within our fitting accuracy | 103 |
| 6.5 | MD simulation results for the propagation of the temperature wave up the funnel. Dark dots indicate the location of the shock. The shaded region is the realm inside the funnel. . . . .   | 104 |
| 6.6 | schematic. The piston moves into the gas with a constant supersonic velocity $u_p$ . A normal shock separates the undisturbed region 1 from the compressed region 2. The shock propagates into the undisturbed region with a velocity $u_s$ . . . . .  | 106 |
| 6.7 | The vertical velocity ( <b>a</b> ) and pressure profiles ( <b>b</b> ) taken through the center of the funnel ( $e_0 = 0.9$ , $\tau = 56\sqrt{g\sigma}$ ). In the free stream the vertical velocity changes due to gravity. Behind the shock, the flow reaches a constant velocity and the pressure increases. The solid red line indicates the values predicted by the jump conditions and the solid green line indicates the asymptotic pressure predicted by the analytic solution. . . . .  | 108 |
| 6.8 | The shock location versus time for 4 values of $e_0$ . The shock front travels fastest while it is developing and eventually settles to an asymptotic value. The solid lines are a fit to the asymptotic region. The final velocity $u_s$ does not vary systematically with $e_0$ . . . . .  | 111 |

# Chapter 1

## Introduction

### 1.1 Motivation

Granular materials are conceptually simple. Any collection of particulate matter whose individual components interact via inelastic collisions qualify as a granular material. This definition includes a wide range of systems across many scales such as: sand, coal, pills, rice, basketballs, cake sprinkles, and asteroids.

The motion of granular materials frequently arises in industrial applications such as moving cereal through a plant, mixing the components in pharmaceuticals, or storing grains in silos. Granular materials are second only to water in the tons of material transported [33]. The equations of motion for fluids are well known, allowing water to be handled with great efficiency. For granular flows, however, there remains no accepted theory, severely limiting the ability to control their motion. A 1985 study on solid processing found the average performance of plants was less than 50% of design efficiency [37].

Our difficulty in understanding granular flows can be attributed to two major properties of the material. First, the macroscopic grain size limits the number of particles in a system. A  $\text{cm}^3$  volume element of air at STP contains

approximately  $10^{19}$  individual molecules. For a granular flow consisting of 160 micron spheres, a cubic centimeter, at the maximum density, contains only  $10^5$  particles. Since the statistical fluctuations of a system scale inversely with the square root of the number of particles, these fluctuations are much more prominent in granular fluids [44, 45].

More importantly, collisions between atoms in air conserve energy - collisions between grains do not. With each collision energy is lost to the creation of phonons, plastic deformation of the surfaces, and thermal heating of the grains. The continuous energy sink due to inelastic collisions destroys the spatial and temporal scale separation assumed by hydrodynamics [44, 133].

Despite these concerns researchers have looked to fluids for their inspiration and have developed continuum descriptions analogous to the Navier-Stokes equations of fluid mechanics. While the Navier-Stokes equations are well accepted with a centuries worth of experimental validation, granular continuum theory is still in its beginnings with many open questions and few quantitative experimental comparisons [21, 43]. More experiments are required to validate granular continuum theory, guide further theoretical developments and to understand the limits of its applicability.

## 1.2 Overview of the Dissertation

This dissertation explores the applicability of a hydrodynamic description to rapid granular flows. We study the granular analog of three well understood shock problems in fluid dynamics. For each geometry we ask two

questions: can a hydrodynamic theory describe the results and how well do the techniques developed for fluid mechanics apply to the granular flow? Chapters 3, 5, and 6 present our studies. In Chapter 2, I briefly review the literature on granular flows. In chapter 4 I describe the methods applied to the study of granular flow past an obstacle.

In Chapter 3, I present an experimental study of the wake formed behind a cylinder moving through a thin, vibrated granular layer. Above a critical rod velocity  $v_R$ , a bow shock forms in front of the rod and extends into a v-shaped wake. This system is well described by a continuum, shallow water theory. The wake is directly analogous to a shock wave formed on the surface of a fluid. Both the onset and the half angle of the shock agree with the Mach relation for supersonic flow. In addition, the maximum height of the shock wave decays as a cylindrical sound wave in a fluid.

In Chapter 5, I describe an experimental study of a granular flow interacting with a wedge. The flow is supersonic with the average flow speed more than 10 times the mean sound speed in the fluid. We compare the shock formed at the wedge to a numerical solution of granular continuum equations. The continuum description shows the same qualitative features as the experiment, however, it does not agree quantitatively. We attribute the disagreement in our study to frictional interactions with the confining sidewalls used in the experiment. Further work with MD simulations suggests inter-particle friction may also lead to disagreement between experiment and continuum theory.

In Chapter 6, I use particle simulations to investigate the propagation

of a shock wave through a funnel. For an elastic gas, the changes across a shock can be predicted by jump conditions derived from conservation laws. We find that the jump conditions do not describe the changes across a shock propagating in a granular fluid. Inelastic collisions cause changes in the shock profile that is unaccounted for in the jump conditions. An asymptotic solution of a continuum description including inelasticity shows similarities to our investigations and correctly predicts the shock speed dependence on inelasticity.

Our experiments agree surprisingly well with granular continuum theory, however, they highlight distinctions between inelastic and elastic fluids. Unlike elastic fluids, inelastic flows do not show scale separation; approximations assuming separation of time or spatial scales should be applied with care. In chapter 7 I conclude this study with suggestions for future improvements to the continuum theory and further experimental work.

### **1.3 Why shocks?**

Each of the studies presented in this dissertation investigates shocks found in granular flows. Inelastic collisions dissipate the energy in granular flows, hence, granular materials must be forced to maintain a fluid-like state. Shock waves provide a method to transfer energy from the boundaries into the bulk of the fluid. Understanding the propagation of energy by shocks is crucial to our understanding of granular flows [46].

Shock waves occur in nature when a fluid is perturbed faster than the sound speed in the material - the rate at which information can be transmitted.



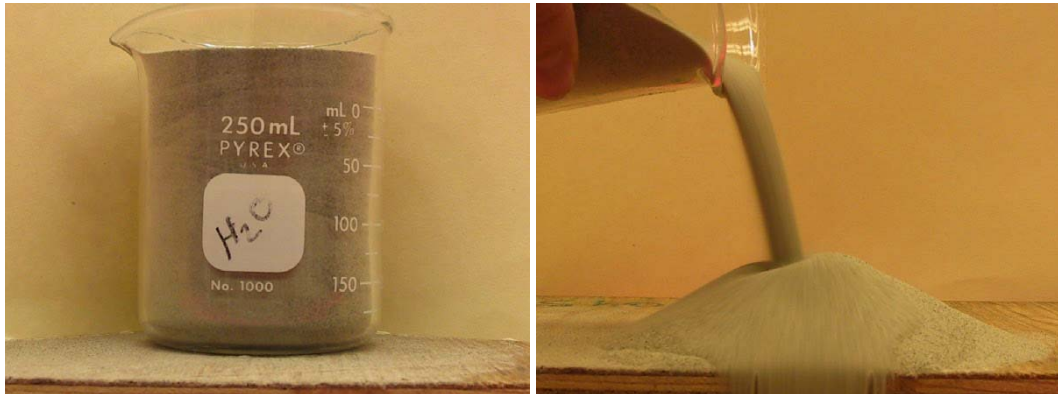


Figure 1.1: **a)** Sand in an open container behaves as a liquid taking on the shape of the container. The surface can support some stress. **b)** When the beaker is tilted, the sand flows out of the beaker resembling a fluid. The granular flow is *supersonic*: the mean flow velocity is greater than the speed of a pressure wave. When the sand hits the surface, inelastic collisions quickly dissipate energy and the sand forms a weak solid.

Since the sound speed in air or water is high, shocks are rare and occur under high energy conditions. For instance thunder is caused by the rapid heating of the air by 10,000 Amperes of current traveling through the air in a bolt of lightning. A shock forms at the nose of an airplane once it passes the speed of sound in air, 331 m/s at STP.

The sound speed in a granular medium is often much smaller than the streaming velocity. Hence shocks are common in granular media. Consider the sand pouring out of a beaker shown in Fig 1.1. Gravity accelerates the flow downward, creating an average velocity  $U$  that reaches 100 cm/s after the sand has fallen only 5 cm. In contrast, the sound speed  $c$  in the granular gas becomes small, typically 10 cm/s. The simple act of turning over a beaker full

of sand can easily generate a supersonic flow with Mach number,

$$M = U/c \tag{1.1}$$

equal to 10.

The sound speed in a gas can be determined from thermodynamic relations,

$$c = \sqrt{\left(\frac{\partial P}{\partial \rho}\right)_S} = \sqrt{\frac{c_p}{c_v} \left(\frac{\partial P}{\partial \rho}\right)_T}, \tag{1.2}$$

where  $\rho$  is the local density,  $S$  is the entropy,  $c_p$  is the specific heat at constant pressure,  $c_v$  is the specific heat at constant volume, and  $T$  is the temperature.

The constituent particles of granular flows are too large to be affected by thermal energy,  $k_B T \ll mg\sigma$ , where  $\sigma$  is the particle diameter. Instead, the temperature for a granular fluid is dominated by the random component of the kinetic energy,

$$T = \left(\frac{1}{D}\right) (\langle v^2 \rangle - \langle v \rangle^2), \tag{1.3}$$

where  $D$  is the dimension of the flow. It is the random component of the velocity that causes particles to collide and therefore is reduced by the coefficient of restitution  $e$ . Inelastic collisions dissipate  $T$ .

For a dense inelastic gas,  $c$  is given by [109]:

$$c = \sqrt{T\chi \left(1 + \frac{2}{3}\chi + \frac{\nu}{\chi} \frac{\partial \chi}{\partial \nu}\right)}, \tag{1.4}$$

where,  $\nu$  is the volume fraction,  $\chi = 1 + 2(1+e)G(\nu)$  is the dense gas correction to the equation of state and  $G(\nu)$  is the radial distribution function evaluated at contact.

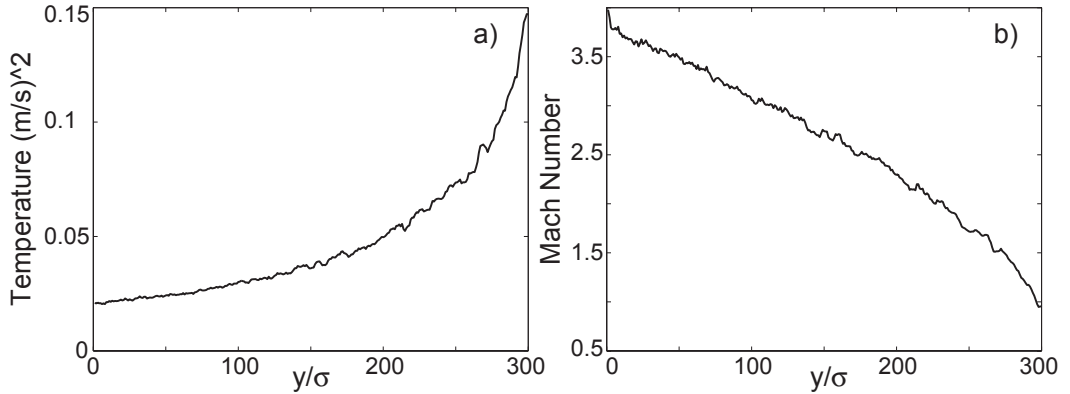


Figure 1.2: Molecular dynamics simulation of a granular flow through a quasi 2D cell. The mean values of **a)** Temperature and **b)** Mach number are plotted versus distance from the bottom of the cell. Particles were injected into the top of the cell,  $y = 300\sigma$ , with an initial velocity chosen from a Gaussian distribution centered at  $V_y$ . The width of the distribution corresponds to the flows temperature. As the particles collide inelastically,  $e = 0.97$ , but without friction  $\mu = 0$  the temperature is dissipated and the sound speed decreases. Within 10 particle diameters the Mach number is greater than 1.

Consider the results from our MD simulation shown in Fig. 1.2. More details regarding the simulation methodology are discussed in Chapter 4. In the simulation inelastic particles were injected with a velocity  $V_y$  and temperature  $T$  (the particles initial velocity was chosen from a Gaussian distribution with width  $T$ ). The temperature profile of the fluid continuously decayed as it moved away from the top boundary. Although the granular fluid entered the box with a Mach number less than one, within a few particle diameters inelastic collisions cooled the gas and the Mach number increased beyond unity.

When a supersonic flow encounters an obstacle a shock is created. The

shock separates two regions of the flow, an undisturbed region that is unaware of the obstacle, and a region where the streamlines have adjusted to fit the boundary conditions at the obstacle (Fig. 1.3). The flow behind a shock is changed compared with the undisturbed region. For free surface flows, the height of the surface behind the shock increases. For compression shocks in the bulk of a fluid, the density and temperature increase. In an ideal fluid with no viscosity, heat conduction, or dissipation, a shock is a zero-width surface of discontinuity. In a non-ideal fluid the shock has a finite width on the order of a particle's mean free path in the fluid [5].

When a fluid with velocity  $U > c$  impinges perpendicularly onto an obstacle, a *normal* shock forms and propagates in the  $-U$  direction. If, instead, the fluid velocity and the obstacle are not perpendicular, an *oblique* shock forms and propagates into the flow at an angle and with a speed determined by the local flow values.

In this dissertation, we look for the analogous behavior in granular shocks.

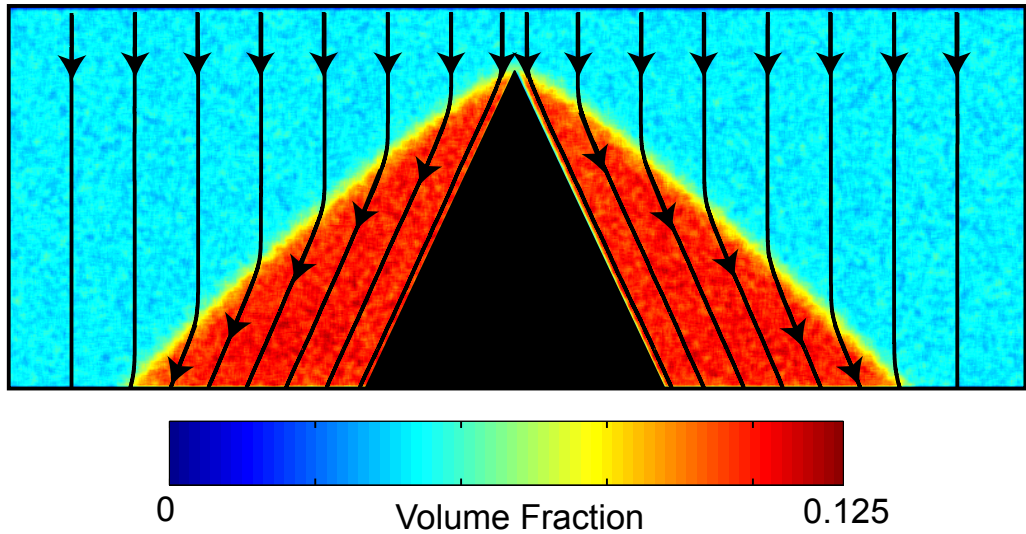


Figure 1.3: Molecular Dynamics simulation of elastic, frictionless particles interacting with an obstacle ( $g=0$ ). The flow is incident onto a wedge with  $M = 2.5$ . Impenetrable boundary conditions at the surface of the wedge require the flow streamlines to be parallel. The interface between the incident and deflected flow is a shock, where the streamlines change. Behind the shock the flows volume fraction, temperature and pressure are greater than in front of the shock.

## Chapter 2

### Review of Granular Flow Phenomena

*Portions of the contents of this chapter have been published in the Fermi School Papers [118].*

Granular materials have captured the interest of physicists for a long time. In 1773 Coulomb proposed the ideas of static friction, the force responsible for granular piles [26]. In 1831, Faraday discovered convection rolls in vibrated powders [40]. Prandtl noticed shock interactions in sawdust ejecting from a nozzle, which later led to his discovery of the expansion fan [5]. Reynolds introduced the notion of dilatancy, suggesting that in order to flow, a granular material must first expand [102]. A recent resurgence in physicist participation in the science of granular materials was sparked when Pierre-Gilles de Gennes recommended the field to French scientists [33, 118]. Since then the scientific literature on granular materials has boomed with more than 700 papers appearing in 2000-2003.

In sections 1 and 2 of this chapter, I briefly describe classes of experiments on granular materials and how they led the field to consider the applicability of continuum equations. In section 3 I review recent experimental and theoretical work on shock waves in granular flows. In section 4 I introduce

molecular dynamics simulations as a useful tool for understanding granular flows. Finally in section 5 I review the continuum description considered in this dissertation. I will save specific introductions to the experiments in this thesis for the chapters in which they are discussed.

## 2.1 Static Granular Materials

While the focus of this dissertation will be rapid granular flows, I want to acknowledge the vast amount of research devoted to static granular problems.

The natural state of a granular material is a pile. Even this simple structure of grains resting on each other contains a great richness of behavior and remains a current topic of research. For instance, Bagnold showed that the surface angle of a sand pile can have only two values, the static angle of repose  $\theta_s$  and the dynamic angle  $\theta_d$ . If one continued to add sand forcing a pile beyond  $\theta_s$ , a large avalanche would move an entire wedge of material down the pile. After the big avalanche, the pile would have an angle of  $\theta_d$  [7, 54]. While this picture worked for large piles, experiments later showed that small sand piles can have a power law distribution of static angles [54].

The forces in a sand pile are not uniformly distributed among the grains, but are carried by a small fraction of the particles along stress chains. The stress chains lead to history dependence for granular materials. If a sand pile is created by raining particles from a sieve, then the pressure distribution at the bottom of the pile is uniform. If instead, the pile is formed by turning over

a container of sand and then removing the container, the pressure distribution at the bottom of pile shows a dip at the center - less of the weight of the particles is carried down the center of the pile than at the edges [123].

When granular material is held inside a container, additional phenomena occur. For instance, above a critical depth, the frictional interaction between grains and between grains and the walls allow a portion of the pile's weight to be supported by the walls of the container. This leads to a pressure distribution that is independent of height. It is this feature that allows an hour glass to keep reasonable time; the flow rate through the orifice is nearly constant and not a strong function of the amount of material in the upper cone [59].

## **2.2 Experimental Granular Flows**

The distinguishing characteristic of granular materials is particles lose energy when they collide. Due to these inelastic collisions, it is not possible for a granular flow to be in equilibrium. Energy must be pumped in to offset the energy lost in collisions. Experimentally, there are limited options for adding energy into the system.

### **2.2.1 Sheared Flows**

Granular shear flows often exist in the intermediate regime between solid and fluid like behavior. In a Couette geometry used by [13, 74, 85, 124] a granular material is confined between two, rough cylinders. The outer



cylinder remains fixed while the inner cylinder rotates. The material closest to the boundary is dragged along as the inner cylinder rotates. The energy of this motion is transmitted to a band of particles, but damps within a few particle diameters [13]. The motion in a slowly sheared cell is dominated by the formation and breaking of stress chains [124]. Researchers have found history dependence in shear flows; the response of the grains depends on the direction of the most recent shear [13].

In gravity driven avalanches, the rapid motion of the particles is confined to a thin surface layer. The conditions governing the interaction of the surface layer and the solid material beneath are still unknown. The evolution of the velocity profile and depth of an avalanche are critical test problems for granular flow theory [65, 108, 109].

Surprisingly, avalanches on desert sand dunes can create acoustical energy; the amplitude of the induced low frequency booming of a fully developed avalanche has been compared to rumbling thunder [27, 30]. While the phenomenon has been known for centuries, the mechanism is not understood and is hampered by the inability to reproduce it in a laboratory setting.

### **2.2.2 Rotated Flows**

Granular flow in a horizontal rotating drum is an oft studied geometry rich in phenomena and industrial applications. In the experiments, a cylindrical container is partially filled with a granular material and rotated about an axis perpendicular to gravity. As the cylinder rotates, the granular material



Figure 2.1: An initially uniform mixture of glass beads of three sizes [0.5 mm (blue), 1 mm (gold), 2 mm (red)] segregated into bands. The particles were rotated about an axis perpendicular to gravity at 30 rpm for several hours [88].

moves as a rigid body - remaining static with respect to the container until the surface inclination angle reaches a critical value. At the critical angle, grains near the surface avalanche, flowing parallel to the surface [39, 58, 98]. The critical angle, depth of the flowing region, and velocity profiles have been studied for different materials and rotation rates.

Rotating flows with two or more different sized particles spontaneously segregate into bands with the finest particles in the center of each band and the coarsest on the outside (Fig. 2.1). The mechanism of segregation remains unknown [25, 88].

### 2.2.3 Vibrated Flows

One of the more popular methods for driving granular materials is to shake it. Large scale convective motions have been observed in vertically [38, 41, 72] and horizontally vibrated [120] granular layers. This convection is typically caused by frictional contact with the side walls of the container or due to interaction with an interstitial gas.

Under vertical, sinusoidal vibrations an initially flat granular layer

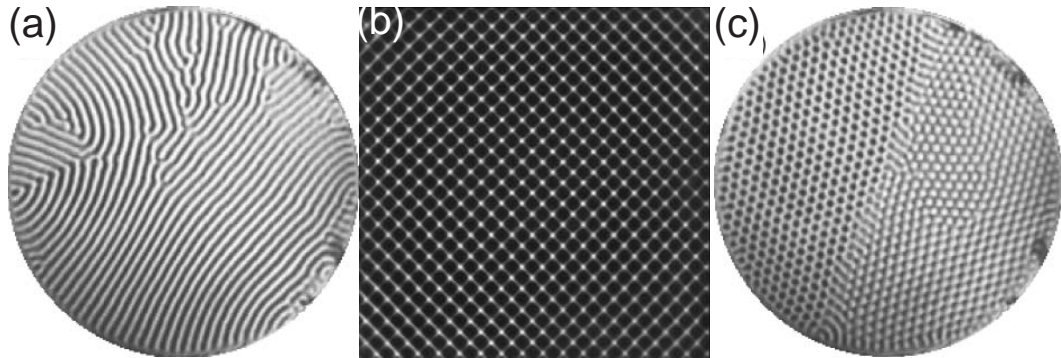


Figure 2.2: Standing wave patterns in vertically vibrated granular layers: (a) stripes, (b) squares, and (c) hexagons. White corresponds to high points of the surface and black to low points. The patterns oscillate at half of the driving frequency [118].

spontaneously forms a standing wave pattern at a critical acceleration of the driving. The patterns slosh subharmonically with respect to driving frequency. An initial array of peaks and valleys will switch places with each collision of the plate so that the pattern reoccurs every two cycles of the driving. These patterns arise only because of the inelastic and frictional interaction of the grains - side wall forcing or interstitial air is not required [11, 79, 122].

Vibrating granular materials of two or more species leads to segregation. In vertical vibration depending on the system parameters, large particles can be confined to either the top (The Brazil Nut Effect) [104] or the bottom of the layer (The Reverse Brazil Nut Effect) [15]. Horizontally vibrating binary mixtures separate particle species into wavy bands [87, 100].

## 2.3 Shock Waves in Granular Materials

Although granular materials often exist in the supersonic regime, few experimental studies on the shocks and their properties have been conducted. Since systematic granular experiments are difficult [21, 43], the majority of theoretical work is compared to numerical simulations.

Hurluck and Dimon have investigated two-dimensional, dense granular flow through a funnel. In their experiment the particles roll down an inclined plane tilted at an adjustable angle  $\theta$ . The inclined plane is bounded by rough, confining walls arranged in a funnel with opening angle  $\beta$ . For sufficiently dense flows, shock waves spontaneously form near the bottom of the funnel and propagate upstream. The researchers measure the shock speed as a function of the two angles, the roughness of the side walls, and the polydispersity of the flow [55–57, 125].

Amarouchene *et al.* photographed sand falling under gravity confined between two, vertical, parallel plexiglas flowing past obstacles. Shocks formed near the obstacles. They determined the shape of the interface and described the flow as a dynamic sand dune [4].

In their 1995 paper, Goldshtein *et al.* observed compression and expansion waves in a vibrated granular layer. They postulated that the shock is responsible for delivering the energy into the cell [49] as opposed to the conduction mechanism previously suggested by Hapf. Each time the layer collided with the plate a shock formed and propagated through the layer, transmit-

ting the energy of the collision upward to the surface. In order to estimate the amount of energy transmitted by the shock, the researchers theoretically examined the granular analog of a piston moving in a gas. They determined that as much as 1/2 of the work performed by the piston can be converted into granular temperature [46]. We investigate this problem further in Chapter 6.

Bougie *et al.* numerically studied the shock formed in an oscillated granular layer [14]. They compared numerical solutions of inelastic continuum equations [63] to frictionless molecular dynamics simulations (Fig. 2.3). The two simulations show good agreement throughout the cycle, despite the presence of large spatial gradients and a strong time dependence. In the dilute regimes above and below the layer, numerical solutions of the inelastic continuum equations are unstable unless artificial dissipation is added [14], following the example from numerical solutions of Knudsen gases [103]. The effect of the extra dissipation is most pronounced in the falling layer and accounts for the disagreement between MD and continuum at the top of the cell.

Researchers have used molecular dynamics simulations to investigate the interaction of two-dimensional granular flows and disks. In both simulations, one with a hard sphere model [18] and one using a soft sphere potential [129], a bow shock was observed in front of the disk. In the soft sphere simulation, a high temperature low density region formed directly between the shock front and the disk. In the hard sphere simulation a gap opened between the disk and the shock front. This phenomenon has not been observed experimentally.

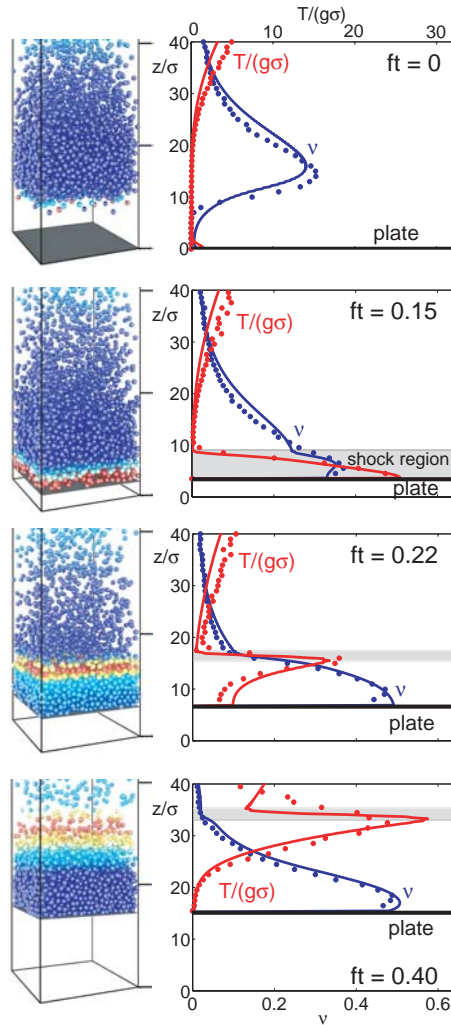


Figure 2.3: Shock formation and propagation in an oscillated granular layer. The dimensionless temperature  $T/g\sigma$  and volume fraction  $\nu$  are plotted as functions of the dimensionless height  $z/\sigma$  at four times  $ft$  in the oscillation cycle. For each time, a snap shot from the MD simulation is shown in the left column with individual particles color coded according to temperature: high  $T$  in red, low  $T$  in blue, and the bottom plate of the container shaded solid gray. The right column shows the horizontally averaged  $\nu$  (blue) and  $T/g\sigma$  (red) for the same four times. The plate is shown as a horizontal black solid line, results from MD simulations are shown as dots, and continuum results are solid lines (From [14])

## 2.4 Multiphase Flows

Adding an interstitial fluid between the grains complicates an already difficult problem. The surrounding fluid leads to long range interactions between particles and an additional source of temperature supplied by the motion of the fluid. When two nearby particles sediment in a fluid, the interaction of the particles and wakes leads to a transfer of linear momentum into horizontal momentum [42].

In our experiment with F. Merkt, R.D. Deegan and D. Goldman, we found that a vertically vibrated suspension of glass spheres (or cornstarch) and water displays a number of unexpected phenomena (Fig. 2.4) [81]. If the suspension is vibrated above a critical acceleration and then poked, the hole created by the perturbation will persist indefinitely. If the system is vibrated with an even greater acceleration, the initial perturbation grows into a wildly delocalized state characterized by the growth of finger-like protrusions. The mechanism for the stable holes and delocalized state is not known, but the shear thickening behavior due to jamming in dense suspensions may be responsible.

## 2.5 Molecular Dynamics Simulations

Molecular Dynamics (MD) simulations performed on personal computers provide an extremely useful tool to examine granular flows [35]. Event driven MD simulations model granular flows as collections of hard spheres that only interact via binary dissipative collisions. Between collisions, parti-

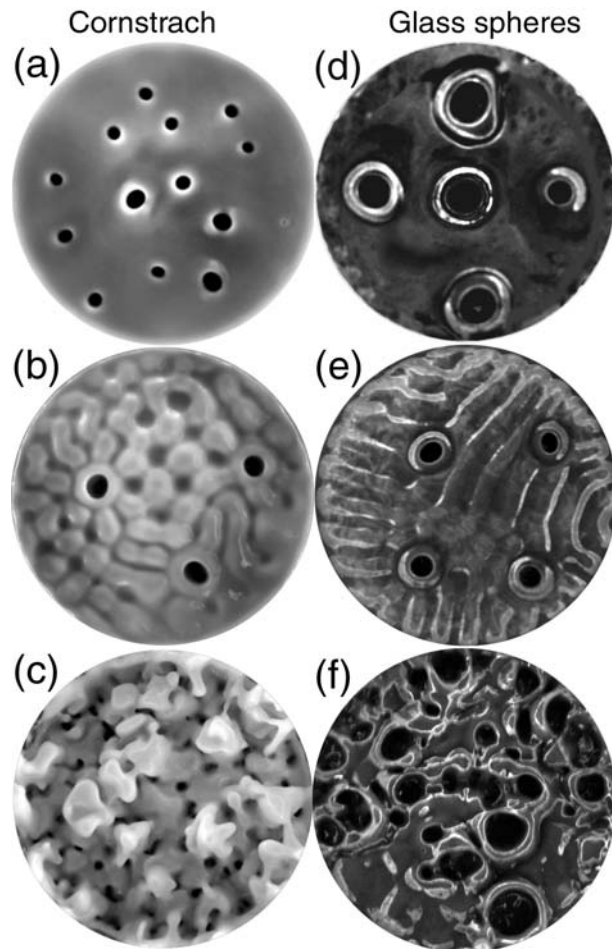


Figure 2.4: Top view of a vibrated aqueous suspension of cornstarch (a-c) or glass spheres (d-f). Each image has a diameter of 9.4 cm. White corresponds to high points of the surface and black to depressions that reach near the container bottom. The layer depth is 0.5 cm for the cornstarch suspension and 0.2 cm for the glass suspension. For high forcing frequencies stable holes occur without Faraday waves: (a) acceleration amplitude  $a = 12g$ ,  $f = 150$  Hz; (d)  $30g$ , 100 Hz. At lower frequencies stable holes are accompanied by the Faraday patterns: (b)  $12g$ , 60 Hz; (e)  $27.3g$ , 92 Hz. Delocalized state: (c)  $30g$ , 120 Hz; (f)  $30g$ , 60 Hz [81]



cle trajectories evolve in accord with Newton's laws. MD simulations allow researchers to peer into the interior of 3-D granular flows, a region not easily accessible with available experimental techniques. In addition, the collision parameters in the simulation can be changed systematically. Experimentally, one can not arbitrarily set the values of the coefficient of restitution or the strength of frictional interactions.

MD simulations captured the surface wave patterns on vibrated granular layers [11], discovered convective motion of the grains within the pattern [9] and illuminated the role friction plays in stabilizing the patterns [82].

## 2.6 Continuum Description

A complementary method for understanding granular flows is to model the macroscopic motion directly by a continuum field theory that describes the bulk motion of the flow in terms of the density, velocity and temperature fields. Unlike MD simulations, the continuum approach is not limited by particle number. A personal computer currently contains enough memory for useful MD simulations of laboratory experiments. However, industrial processes contain billions of particles, far outside the abilities of MD simulations. Another reason that a continuum approach is attractive is that it could exploit tools such as stability analysis, amplitude equations, and perturbation theory, which have been developed through more than a century of research on the Navier-Stokes equations and other partial differential equations.

Granular flows present many difficulties in developing a continuum the-

ory [119, 133]. Continuum theory requires a separation of length and time scales: variations over space should be small and occur over long distances, so that the behavior of local collections of individual particles can be averaged and replaced with small fluid elements. Changes in time for the flow should occur for times long compared to the mean time between particle collision so that particles moving between fluid elements do not affect the average values in a fluid element. Unfortunately, inelastic collisions between particles create an inherent lack of scale separation [43, 119]. Sufficient separation of scales may only be present for granular flows in the specific circumstances of low density and low dissipation [43, 66, 119].

The derivation of the continuum equations from kinetic theory makes assumptions about the underlying statistics of granular flows, assumptions which have not been verified by MD simulations. For instance, the velocity distribution function is assumed to have a steady state functional form that is nearly Gaussian. Since granular flows are dissipative, a steady state distribution function can only be achieved in the presence of forcing. Granular experiments have yielded velocity distributions that depend on the forcing characteristics and experimental geometry [69, 91, 106, 124, 132].

Also, most derivations of continuum equations assume Boltzmann's molecular chaos (particle velocities before collisions are uncorrelated), but strong velocity correlations have been found in MD simulations [12, 83].

Despite the reservations regarding a continuum approach in granular media, observations of granular media have revealed many phenomena simi-

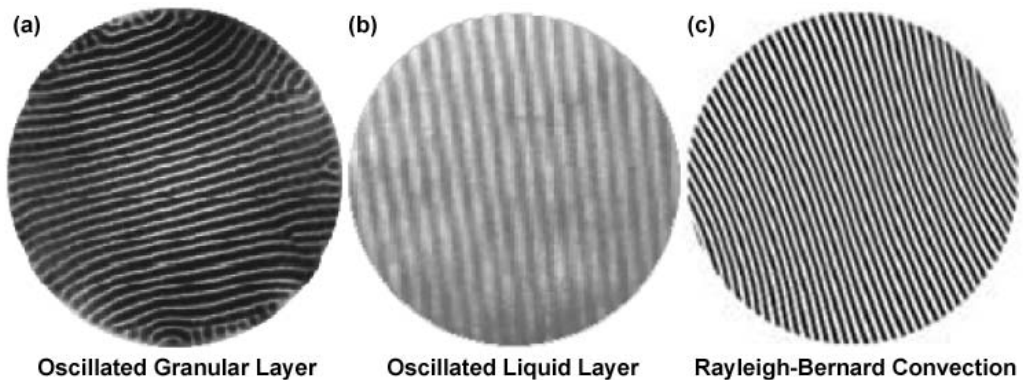


Figure 2.5: Forced granular materials produce qualitatively similar patterns as forced fluids: (a) stripe pattern formed by a vertically oscillated granular layer [80], (b) stripe pattern formed by a vertically oscillated layer of water [68], (c) stripe pattern formed in thermal convection of a fluid ( $CO_2$ ) [95].

lar to those observed in continuum systems. For example, the stripe patterns shown in Fig. 2.5(a) look like those in vertically oscillated liquid layers [68] (Fig. 2.5(b)), chemical reaction-diffusion systems [97], Rayleigh-Bénard convection in fluids [8](Fig. 2.5(c)), and liquid crystals [34].

Not only are the patterns similar for granular and continuum systems, but also some the same pattern instabilities have been observed. For example, when the wave number of parallel convection rolls (stripes) in a Rayleigh-Bénard convection becomes small, an instability leads to the formation of cross rolls with a larger wave number oriented perpendicular to the original rolls [29, 31]; the same instability has been observed for stripes in oscillated granular layers, as Fig. 2.6 illustrates. The cross rolls invade the region of small wave number stripes such that, after sufficient time, the region contains

a pattern of straight stripes perpendicular to the original pattern and with a larger wave number.

Granular stripe patterns also exhibit a skew varicose instability like that in convection roll patterns (Fig. 2.6). When the local wave number becomes too large, an initially straight pattern of stripes will develop a distortion which evolves into a dislocation defect. The defect propagates away, destroying one of the stripes and decreasing the local wave number of the pattern. The stability of the stripe pattern in fluid convection is well described by amplitude equations derived from the Navier-Stokes equations for fluids [29]. That the granular pattern shows the same behavior strongly suggests a continuum description for the vibrated system is applicable.

Aspects of the phase diagram for granular patterns have been reproduced by amplitude equation models. For example, a phenomenological continuum model requiring that the mass of the layer is conserved locally, produces stripe, square, and oscillon-like patterns similar to those found in experiment [22, 121]. A continuum, shallow water like model of the granular layer captures the patterns and yields a dispersion relation which agrees with experiment [36]. The success of these and other models [105, 107, 112, 126] provides further motivation for considering continuum equations derived for a granular gas.

Additional evidence for the applicability of continuum theory to granular media is provided by a recent study of noise in vertically oscillating granular layers. In the Rayleigh-Bénard system below the onset of convection, thermal

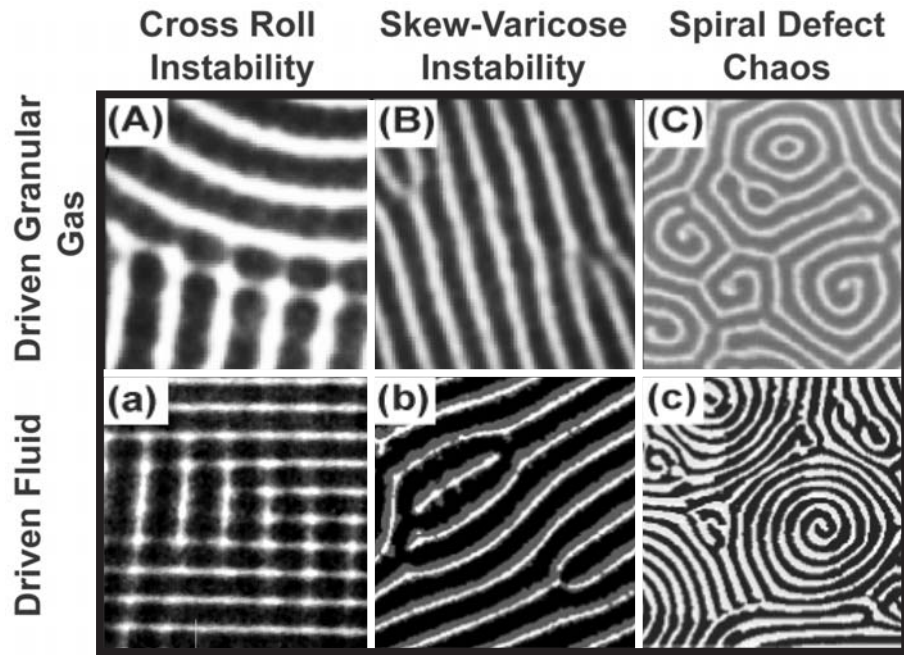


Figure 2.6: Instabilities of patterns found in oscillating granular layers and Rayleigh-Bénard convection in a fluid. Cross roll instability in stripes: (A) Vibrated granular layer [31] and (a) Rayleigh-Bénard convection [20]. Skew varicose instability in stripes: (B) Granular layer [31] and (b) Rayleigh-Bénard convection [6]. Spiral defect chaos in: (C) vibrated granular layer [32] and (c) Rayleigh-Bénard convection [6].

noise has been found to drive noisy transient disordered waves with a characteristic length scale (Fig. 2.6(a) and (c)). The intensity and coherence of these modes increase as the transition from conduction to convection is approached [89]. Above onset the coherent spatial motion develops orientational order (Fig. 2.6(b) and (d)). This behavior is well-described by the fluctuating hydrodynamic theory of Swift and Hohenberg [117]. Remarkably, the same noisy incoherent modes are observed just below the transition from a flat vertically oscillating granular layer to a square pattern (Fig. 2.6 A-D). The Swift-Hohenberg continuum theory describes the observations for the granular system very well, even though the noise is many orders of magnitude greater than thermal noise [45].

## 2.7 Jenkins and Richman Equations

Fired by the promise of quantitative predictive power and encouraged by the qualitative similarity of granular flows to fluid flows, researchers have proposed various continuum descriptions for rapid granular flows [1, 16, 48, 52, 63, 78, 110]. This dissertation focuses on one such description [63] and compares results from it to MD simulations and a granular flow experiment.

Jenkins and Richman derived a set of inelastic continuum equations in a manner similar to the derivation of the Navier-Stokes equations [63]. This approach begins with the single particle distribution function  $f^{(1)}(\mathbf{r}, \mathbf{v}, t)$ , which gives the probability of finding a particle at a position  $\mathbf{r}$  with a velocity  $\mathbf{v}$  at a given time  $t$ . Integrating  $f^{(1)}$  over all possible velocities gives the local

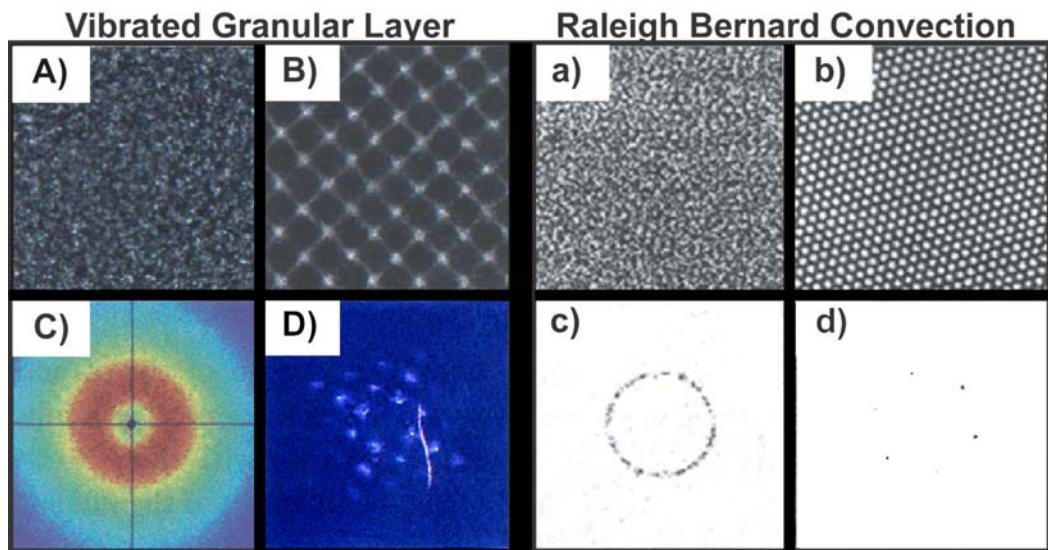


Figure 2.7: Vibrated granular layers (A-D) [45] display coherent motion below the onset of patterns similar to the fluctuating thermal noise observed in Rayleigh-Bénard convection (a-d) [131]. Below onset, snapshots of the system below (A and a) and above (B and b) show no long range order but the modulus of the corresponding fourier transform (C and c) and (D and d) indicate each system fluctuates within a ring in phase space. Above onset, the intensity of the coherent motion increases and orientational emerges.

number density,  $n(\mathbf{r}, t)$ . The ensemble averaged value of any particle property  $\psi$  is determined by

$$\langle \psi \rangle = \frac{1}{n} \int \psi(\mathbf{v}) f^{(1)}(\mathbf{v}, \mathbf{r}, t) d\mathbf{v}. \quad (2.1)$$

The Inelastic Enskog-Boltzmann equation describes how  $f^{(1)}$  changes in time. Particles can move in and out of volume elements due to streaming motion; particle velocities can change in response to external forces  $\mathbf{F}$ ; or particles can be scattered out of elements by collisions. The time rate of change for  $f^{(1)}$  is given by

$$\frac{\partial f^{(1)}}{\partial t} + \mathbf{v} \cdot \nabla_{\mathbf{r}} f^{(1)} + \mathbf{F} \cdot \nabla_{\mathbf{v}} f^{(1)} = \Theta(f^{(1)}), \quad (2.2)$$

where  $\Theta(f^{(1)})$  is the collision operator. Collisions are considered to be binary, frictionless, and inelastic with a constant coefficient of restitution  $e_0$  [63]. Integrating eq. (2.2) yields the balance law for the number density,

$$\frac{\partial n}{\partial t} + \nabla \cdot (n\mathbf{u}) = 0, \quad (2.3)$$

where  $\mathbf{u}(\mathbf{r}, t) = (1/n) \int \mathbf{v} f^{(1)}(\mathbf{r}, \mathbf{v}, t) d\mathbf{v}$  is the local average velocity. Multiplying by the velocity and then integrating gives the balance law for momentum,

$$n \left( \frac{\partial \mathbf{u}}{\partial t} + \mathbf{u} \cdot \nabla \mathbf{u} \right) = \nabla \cdot \underline{\mathbf{P}} - ng\hat{\mathbf{z}}, \quad (2.4)$$



Finally, multiplying by  $\mathbf{v}^2$  and integrating gives the balance law for the energy, where the *granular temperature*  $T$  is proportional to the average kinetic energy of the random motion of particles,

$$T = 1/3 (\langle \mathbf{v}^2 \rangle - \langle \mathbf{v} \rangle^2), \quad (2.5)$$

$$\frac{3}{2}n \left( \frac{\partial T}{\partial t} + \mathbf{u} \cdot \nabla T \right) = -\nabla \cdot \mathbf{q} + \underline{\mathbf{P}} : \underline{\mathbf{E}} - \gamma, \quad (2.6)$$

where  $\gamma$  is the energy loss rate due to inelastic collisions.

A series of approximations is required in order to derive the form of the pressure tensor  $\underline{\mathbf{P}}$ , the velocity gradient tensor  $\underline{\mathbf{E}}$ , and the heat flux  $\mathbf{q}$ . One assumes that  $f^{(1)}$  is nearly Gaussian, that spatial derivatives of  $n$ ,  $\mathbf{u}$ , and  $T$  are small, and that  $(1 - e_0)$  is small. With these assumptions, the components of the velocity gradient tensor  $\underline{\mathbf{E}}$  are given by:  $E_{ij} = \frac{1}{2} (\partial_j u_i + \partial_i u_j)$ . The components of the stress tensor  $\underline{\mathbf{P}}$  are given by the constitutive relation:

$$P_{ij} = \left[ -p + \left( \lambda - \frac{2}{3}\mu \right) E_{kk} \right] \delta_{ij} + 2\mu E_{ij}, \quad (2.7)$$

and the heat flux is given by Fourier's law:

$$\mathbf{q} = -\kappa \nabla T. \quad (2.8)$$

The transport coefficients are fully determined and are the same as for a dense gas of hard spheres. The bulk viscosity is given by

$$\lambda = \frac{8}{3\sqrt{\pi}} n \sigma T^{1/2} G(\nu), \quad (2.9)$$

the shear viscosity by

$$\mu = \frac{\sqrt{\pi}}{6} n \sigma T^{1/2} \left[ \frac{5}{16} \frac{1}{G(\nu)} + 1 + \frac{4}{5} \left( 1 + \frac{12}{\pi} \right) \right], \quad (2.10)$$

and the thermal conductivity by

$$\kappa = \frac{15\sqrt{\pi}}{16} n \sigma T^{1/2} \left[ \frac{5}{24} \frac{1}{G(\nu)} + 1 + \frac{6}{5} \left( 1 + \frac{32}{9\pi} \right) \right], \quad (2.11)$$

where

$$G(\nu) = \nu g_0(\nu), \quad (2.12)$$

and the radial distribution function at contact,  $g_0$ , is [47]:

$$g_0(\nu) = \left[ 1 - \left( \frac{\nu}{\nu_{max}} \right)^{\frac{4}{3}\nu_{max}} \right]^{-1}, \quad (2.13)$$

where  $\nu$  is the volume fraction of the flow and  $\nu_{max} = 0.65$  is the 3-dimensional random close-packed volume fraction.

The only difference between these equations and those for an elastic gas is  $\gamma$  in eq. (2.6), which accounts for the temperature loss due to inelastic collisions:

$$\gamma = \frac{12}{\sqrt{\pi}} (1 - e_0^2) \frac{n T^{3/2}}{\sigma} G(\nu). \quad (2.14)$$

The system is closed by an equation of state, proposed by Goldshtein *et al.* in [47],

$$p = nT [1 + 2(1 + e_0)G(\nu)]. \quad (2.15)$$

Direct experimental verification of the inelastic continuum equations has been slow in coming due to the complexity of solving the equations and also due to difficulties in finding an appropriate experimental system [21]. The presence of strong gradients in granular materials [43, 119] adds additional difficulty to solving continuum equations. For instance, simulations of the vertically vibrated layer find that the temperature varies by three orders of magnitude throughout the cycle [14]. Thus, unlike most Navier-Stokes simulations, the transport coefficients ( $\lambda$ ,  $\mu$  and  $\kappa$ ) cannot be treated as constants, but must be recomputed at each grid point at every time step. Additionally, a complete set of boundary conditions for granular flows is still not established and remains an active area of research [17, 61, 64, 65, 113, 114]. Without the correct boundary conditions, numerical solutions can be unstable and are not guaranteed to converge to a correct solution in the bulk. For a good discussion on the difficulties in determining the correct boundary conditions, see Goldhirsch's review paper [43].

In a 1990 review paper [21], Campbell made a resounding call for granular flow experiments to make quantitative tests of the inelastic continuum approach. The application of new technologies such as particle tracking in two and three dimensions is now making these measurements feasible, but granular flow experiments still present technical challenges. Plugs develop in pipe flow [2, 96], wall effects dominate in quasi-two-dimensional experiments [101, 132], and detailed bulk flow measurements are difficult to make in fully three dimensional experiments [13].

## Chapter 3

# Wake Behind a Cylinder in a Granular Flow

*Portions of the contents of this chapter have been submitted to PRE Rapid Communications*

### 3.1 Abstract

We study the V-shaped wake (Mach cone) formed by a cylindrical rod moving through a thin, vertically vibrated granular layer. The wake, analogous to a shock (hydraulic jump) in shallow water, appears for rod velocities  $v_R$  greater than a critical velocity  $c$ . We measure the half-angle  $\theta$  of the wake as a function of  $v_R$  and layer depth  $h$ . The angle satisfies the Mach relation,

$$\sin \theta = c/v_R = 1/M, \quad (3.1)$$

where  $M$  is the Mach Number and  $c = \sqrt{gh}$ , even for  $h$  as small as one particle diameter.

### 3.2 Introduction

We present a study of the shape of the wake behind a cylinder in a vertically vibrated granular layer. Wake flow was originally solved by Havelock for an infinitesimal disturbance moving on the surface of a dispersive

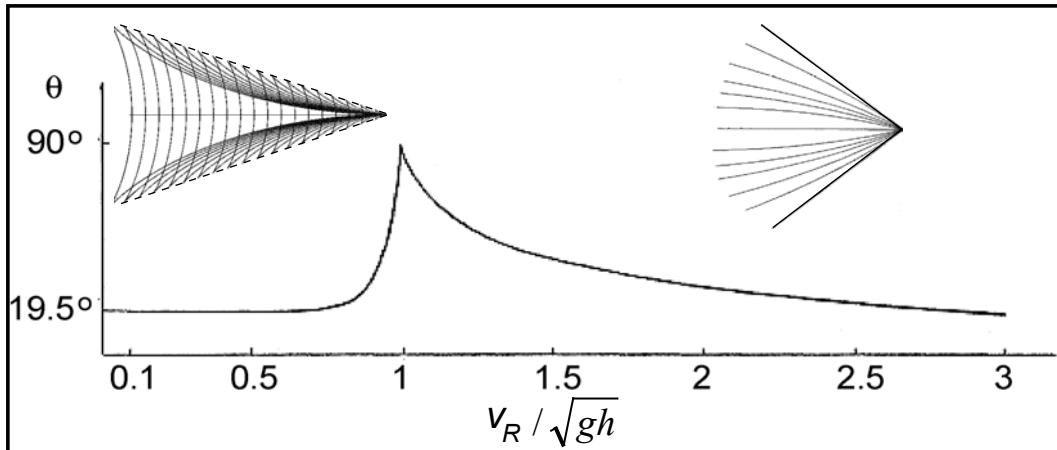


Figure 3.1: The dependence of the wake half-angle  $\theta$  on the velocity of an object,  $v_R$ , traveling through a surface-tensionless fluid of finite depth  $h$  [53]. For  $v_R < \sqrt{gh}$ , both transverse and diverging waves contribute to the wake leading, to the Kelvin wedge pattern (left inset). For  $v_R > \sqrt{gh}$ , the transverse waves are not resonantly excited. A superposition of diverging waves leads to the formation of a shock (right inset). The opening angle decreases with increasing  $v_R$ .

medium [53]. For water, neglecting surface tension, the dispersion relation of surface (gravity and capillary) waves is known, and the shape of asymptotic wake can be solved for analytically. The speed of a long gravitational wave on water (neglecting surface tension) is  $c = \sqrt{gh}$ . If the disturbance propagates with a speed  $v_R$  less than  $c$ , the far wake behind the disturbance is described by the Kelvin wedge (Fig. 3.1). The wake consists of transverse and longitudinal waves all contained within an envelope at a fixed angle of  $19.5^\circ$ . If the disturbance propagates with  $v_R > c$ , a shock wave forms. The transverse waves are no longer amplified and the angle of the wake envelope follows the Mach relation (Fig. 3.1).

Detailed studies of wakes in granular materials have not been performed. However, experiments and simulations have examined the drag force on an object inserted into a granular medium. When the granular medium is static, the drag force is found to be independent of [3, 23] or only weakly dependent [130] on the object velocity. When the granular medium is fluidized via external forcing, as in an experiment by Zik [134] and simulations by Buscholtz and Wassgren [18, 129], the drag is found to be proportional to the square of the object's velocity. The square dependence is consistent with a shock wave formed at the front of the object [71].

### 3.3 Experiment

A stainless steel rod of diameter  $D = 0.75$  mm is inserted into a shallow, vibrofluidized granular layer consisting of bronze spheres with a diameter  $\sigma =$

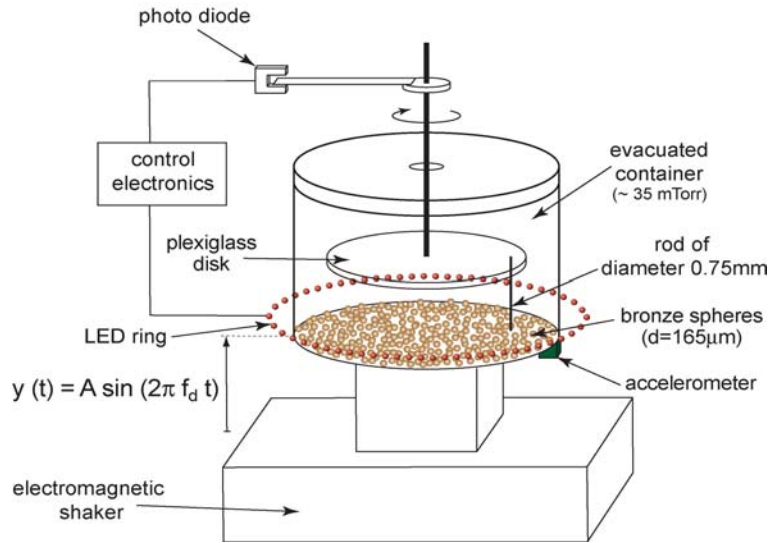


Figure 3.2: The granular layer is confined in a plexiglass container (17.75 cm in diameter and 10.7 cm tall) with an aluminum base. A motor is attached to a plexiglass disk through a rotary motion feedthrough. A stainless steel rod is suspended from the disk at a radius of 5.1 cm. The motor spins the disk such that the rod moves with a constant speed  $v_R$  in the range of 4-30 cm/s. Outside of the container, a thick aluminum plate also rotates with the rod. On each rotation the aluminum plate passes through a photo diode, triggering the CCD camera to record 52 images of the layer.

0.17 mm. The rod moves in a circular path of radius 51 mm with a constant speed  $v_R$  in the range 4-30 cm/s (Fig. 3.2).

The granular layer is vibrofluidized using an apparatus similar to the one described in [45, 79]. A schematic of the apparatus is shown in Fig. 3.3. For each layer depth  $h$ , the peak plate acceleration  $2.2g$  and the nondimensional frequency  $f^* = f_D \sqrt{h/g} = 0.39$  are chosen such that the layer is fluidized but remains below the onset of patterns [86]. The container is evacuated to less

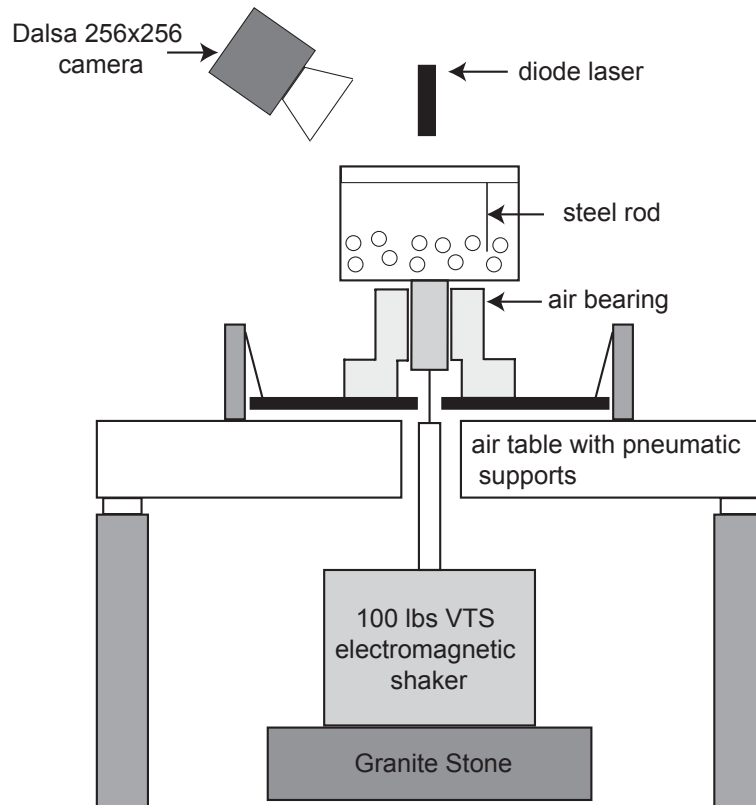


Figure 3.3: The granular layer is vibrated by an electromagnetic shaker. The shaker is attached to the container via a 2.54 cm square air bearing. The bearing minimizes both rotational and horizontal motion, so the container is only forced vertically. The system is sensitive to the tilt of the container. The air bearing rests on an aluminum plate which is suspended above an air table. We adjust the length of the wires until the layer inside the container remains level while being shaken.



than 4 Pa to reduce air effects [94]. The distance from the bottom of the container to the rod is held fixed at  $0.5h$  throughout the container oscillation.

We measure the time averaged height field of the layer behind the rod using a laserline technique similar to the one reported in [41]. A thin laser sheet (1 mm thick) is shone perpendicularly onto the granular layer and imaged by a CCD camera set at a fixed angle to the granular surface (Fig. 3.4). Deviations from a straight line indicate the variations of surface height. The resulting height field is shown in fig. 3.4(b) for  $h=4\sigma$  and  $v_R = 21.5 \pm 0.1$  cm/s.

### 3.4 Results

For small  $v_R$ , the time averaged layer remains everywhere flat to within our experimental error. For  $v_R$  greater than a critical velocity,  $c$ , the height field shows a bow shock structure: a rapid increase in surface height, analogous to a hydraulic jump, develops in front of the rod and extends downstream in a v-shaped wake (Fig. 3.4). The maximum deflection of the layer ( $\Delta h_{max}$ ), measured from the laser line directly behind the rod, as a function of  $v_R$  is shown in Fig. 3.5. For  $v_R$  greater than  $c$ , the layer height increases linearly with rod velocity. A fit to the data for a layer depth of  $h=4\sigma$  indicates a critical wave speed  $c = 8.4 \pm 0.7$  cm/s.

The transition from the subcritical flow without a shock, to a supercritical flow with a bow shock is not sharp, as indicated by the rounding of the transition seen in Fig. 3.5. As the flow accelerates around the rod, a small supercritical region develops for  $v_R$  less than but near  $c$ . A shock forms in this

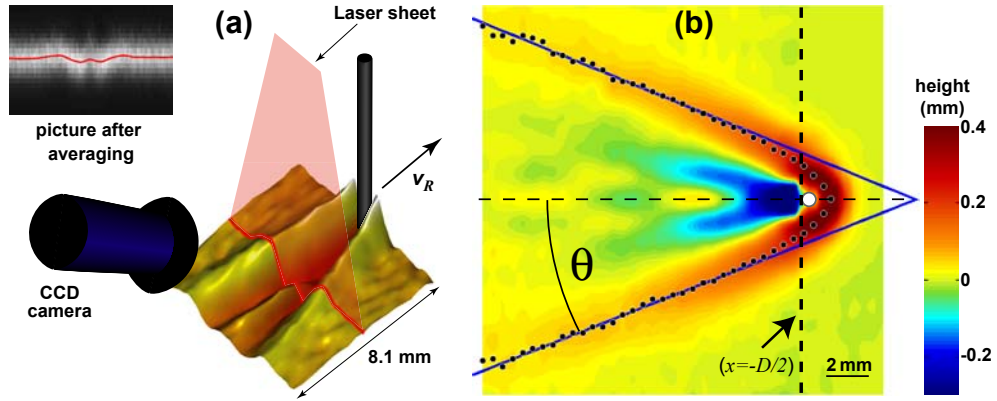


Figure 3.4: (a) Schematic of the laserline scanning technique used to measure the displacement of the surface created by a rod moving through a granular layer. The rod travels in a circular path of  $r = 5.1$  cm. A laser light sheet is incident downward onto an initially flat granular surface. When the rod passes through the laser line it triggers a CCD camera, held at a fixed angle with respect to the flat surface, that captures 52 digital images of the laser line separated in time by  $\delta\tau = 2.2$  ms. For  $v_R = 21.5$  cm/s, the distance between line scans is  $\delta x = v_R * \delta\tau = 0.47$  mm. The inset shows an average over 400 periods of the rod motion. The location of the laser line is determined to subpixel accuracy by finding the center of a Gaussian fit to each vertical slice as shown in the inset (red line). The wake is a 3D reconstruction of the averaged laser lines. (b) The top view of the shock created by the rod, moving to the right, for  $v_R = 21.5$  cm/s. The location of the maximum positive displacement for each laser line is indicated by the dots. A linear fit to the maxima (blue) reveals the wake's asymptotic half angle  $\theta$ .

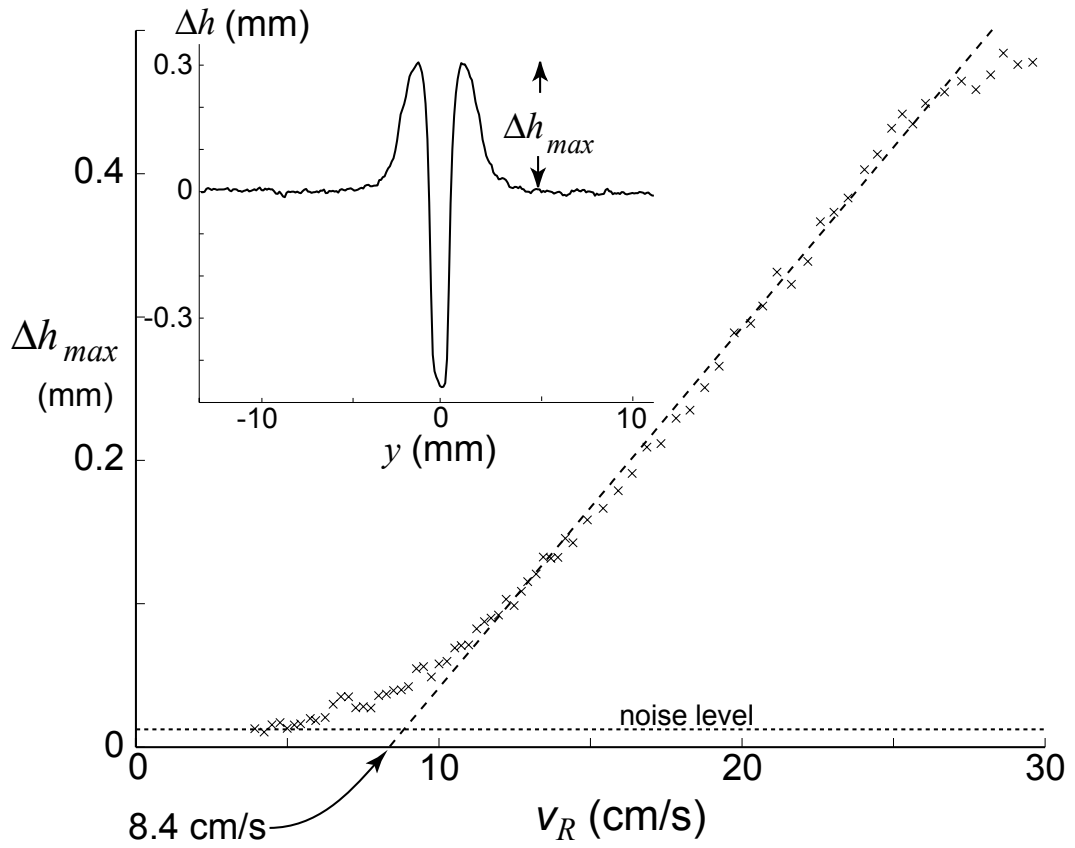


Figure 3.5: The maximum upward displacement of the layer determined from height profiles along the dashed line in Fig. 3.4 (b) behind the rod as a function of rod velocity for layer depth  $h=4\sigma$ . For small  $v_R$  the layer behind the rod remains flat to within experimental accuracy (dotted line). Above a critical velocity the deflection increases linearly (dashed line). The intersection of the dashed line with the horizontal axis indicates a non zero critical velocity. The noise level was determined by the peak to peak oscillations in the flat part of the layer.

region, but does not extend out into the fluid.

We measure the half-angle  $\theta$  of the shock with respect to the axis of the rod's motion as a function of  $v_R$ . We define the location of the shock by the maximum of the height field for each line scan. Near the rod the shock is curved; however, within a few rod diameters the shock straightens, creating a V-shaped wake with a well-defined half-angle. A linear fit through the maxima of the asymptotic shock yields  $\theta$  (Fig. 3.4). We find  $\theta$  is described well by the Mach relation (3.1) for a compressible gas. The linear dependence of the data plotted in Fig. 3.6 indicates a constant surface wave speed. For  $h = 4\sigma$  we find  $c = 7.9 \pm 0.4$  cm/s, which is consistent with the critical speed determined from the height measurement ( $8.4 \pm 0.7$  cm/s).

### 3.5 Shallow water theory

The results can be understood in terms of a shallow water approximation, similar to the approach applied to avalanches [51, 108] and granular free surface patterns [10]. When the depth of a fluid is small compared to the other dimensions in the system, one can neglect the fluid velocity in the vertical direction compared with the velocity components parallel to the surface. In this shallow water approximation, the equations describing the motion of a free surface of an incompressible, isothermal fluid in a gravitational field are equivalent to the equations for a compressible gas flow [71]. In both cases a shock forms when the relative velocity between the fluid and the obstacle is greater than a critical velocity. For waves on a free surface the critical velocity

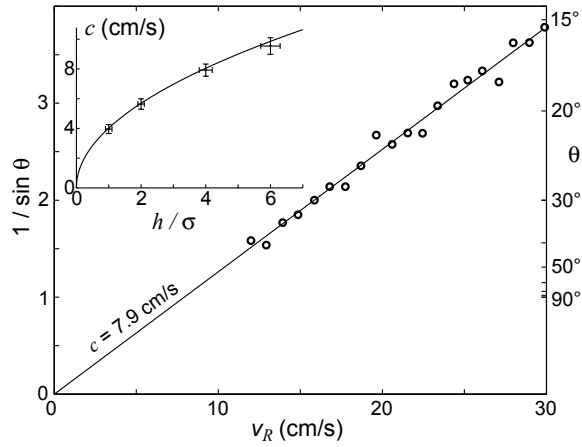


Figure 3.6: The dependence of the half-angle  $\theta$  of the shock cone on  $v_R$ . The ordinate is scaled so that a sinusoidal dependence yields a straight line. The slope yields the wave speed,  $c$ . Inset shows dependence of  $c$  on the layer depth  $h$ . The error includes uncertainty in the depth due to leveling of the container (horizontal error bars) and uncertainty in the algorithm determining the angle (vertical error bars). The solid line is the prediction from shallow water theory,  $c = \sqrt{gh}$ .

is the maximum gravitational wave speed,  $c = \sqrt{gh}$  for long waves without surface tension, and the shock is a discontinuity in height.

For completeness, the derivation of the hydraulic approximation from the Jenkins and Richman equation is included in the Appendix A.

We determined the critical wave speed as a function of layer height by finding the slope of the line from the angle measurements. For  $h = 1-6\sigma$  the surface wave speed follows  $c = \sqrt{gh}$  in agreement with the shallow water interpretation (inset to Fig. 3.6).

The agreement with shallow water theory is surprising. A vibrated granular layer is highly compressible [14, 48]; during each collision with the plate, a shock wave forms in the bulk of the fluid and travels through the layer compressing and heating the grains. Although the volume fraction and granular temperature across the shock can change by as much as a factor of 2 or 100 respectively [14], the energy is quickly dissipated by inelastic collisions [11]. Our molecular dynamics simulations for the conditions of our experiment show that throughout much of the cycle the bulk of the layer has an approximately constant density and temperature (Fig. 3.7). If the forcing of the plate is assumed to only fluidize the granular layer and does not play a strong roll in the propagation of waves on the surface, a shallow water approximation for granular flows is reasonable. Remarkably, the wave speed for a layer depth of only one particle diameter follows the prediction from the continuum, shallow fluid theory. Instead, deviations from the theory appear to occur for deeper layers ( $h=6d$ ). Keeping the container level is more challenging for deeper

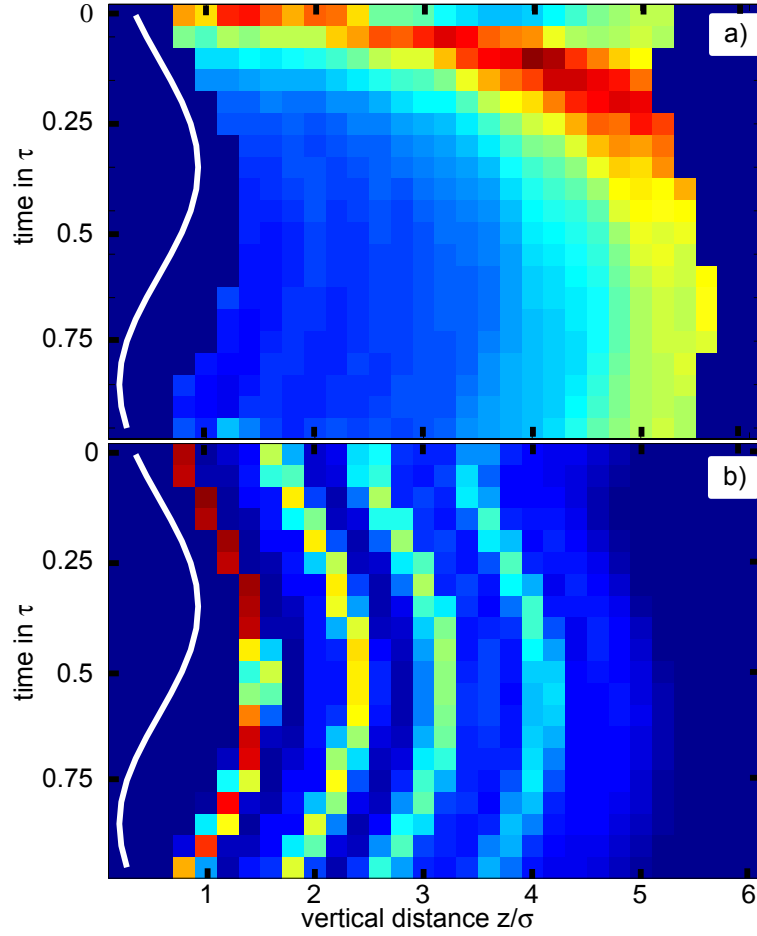


Figure 3.7: Space-time plot of the horizontally averaged flow fields for (a) Temperature and (b) volume fraction from a MD simulation of a vertically vibrated granular layer ( $\Gamma = 2.2$ ,  $f^* = 0.39$ ,  $h = 4\sigma$ ). Each horizontal line shows the averaged field as a function of height in the cell. The crystal ordering of particles can be seen in the volume fraction curve. Red indicates high values of the field; blue indicates low values. For  $t = 0$  the layer begins colliding with the plate (solid white line). Near the plate a compression shock forms, compressing and heating the grains. By  $t = 0.25\tau$ , the shock has traveled through the layer. For the remainder of the cycle, the layer moves with respect to the plate, but the temperature and density profile do not change significantly.

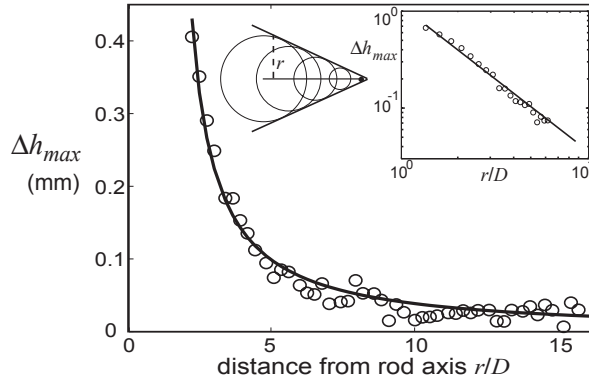


Figure 3.8: The maximum height of the shock front as a function of  $r$ , the distance from the shock front to the rod's axis of motion. The amplitude of the cylindrical sound waves excited by the rod decay as  $1/\sqrt{r}$ , where  $r$  is the radial distance from the origin of the wave. The shock formed by the coalescence of these waves does not extend into the fluid indefinitely, but decays as  $r^{-3/2}$ .

layers, increasing the error in the determination of  $c$ .

### 3.6 Shock Decay

The granular shock rapidly decreases intensity as it extends into the surrounding fluid. The maximum height of the shock versus  $r$ , the distance from the shock to the axis of motion of the rod, is plotted in Fig. 3.8. Within 3 rod diameters, the height of the shock decreases by a factor of two.

In his 1945 paper, Landau presented a scaling argument for the damping of shock waves far from the origin [70]. Here I present his argument for the shape of shocks at large distances from their origination. Then I apply the scaling to the cylinder wake profile.



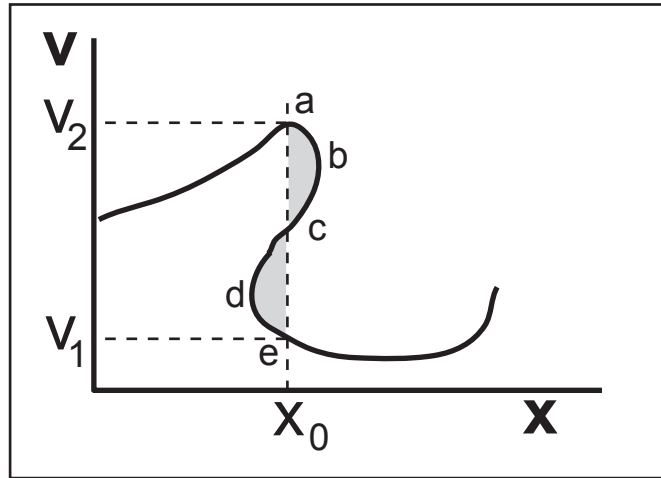


Figure 3.9: A shock profile propagating through a fluid can not be multi-valued. Instead, a discontinuity forms at  $x = x_0$ . The location of the discontinuity is such that the two shaded areas will be equal [71]

In the simplest approximation for the motion of a wave through a fluid, one assumes each point on the wave profile travels with a constant velocity  $u = c_0$ . For the motion of shock waves, this approximation is insufficient - the velocity of the wave depends on the local conditions, namely the local pressure. In the second order approximation

$$u = c_0 + \alpha v, \quad (3.2)$$

where  $\alpha = (\partial u / \partial \rho_0)_S \rho_0 / c_0$ . The first term in the equation describes the motion of the profile without change and the second term accounts for the distortion due to pressure differences in the fluid.

Consider the arbitrary wave shown in Fig. 3.9. Point **a** on the wave is traveling with a faster velocity than point **c**. Eventually, **a** will move ahead

of  $\mathbf{c}$  and the wave profile will be multi-valued. This evolution is prohibited, instead a discontinuity forms at the point  $x = x_0$ .

The location of the discontinuity can be determined by considering the conservation of mass. On either side of the discontinuity, the mass flux must be equal. Let the discontinuity move with a velocity  $u_0$  and the flow on either side of the discontinuity have velocities  $u_1$  and  $u_2$ . Conservation of mass requires

$$\rho_1 (u_1 - u_0) = \rho_2 (u_2 - u_0). \quad (3.3)$$

Solving for  $u_0$  yields,

$$u_0 = \frac{\rho_1 u_1 - \rho_2 u_2}{\rho_1 - \rho_2} = \left. \frac{d(\rho u)}{d\rho} \right|_{u=1/2(u_1+u_2)}. \quad (3.4)$$

Using Eq. 3.2 to evaluate the derivative gives the velocity of the discontinuity

$$u_0 = c_0 + 1/2 (v_1 + v_2). \quad (3.5)$$

The difference in the two shaded areas in Fig. 3.9 is found by integrating

$$\int_{v_1}^{v_2} (x - x_0) dv \quad (3.6)$$

along the curve. The change in area as the curve propagates is

$$\frac{d}{dt} \int_{v_1}^{v_2} (x - x_0) dv = \int_{v_1}^{v_2} ((c_0 + \alpha_0 v) - (c_0 + 1/2 (v_1 + v_2))) dv = 0. \quad (3.7)$$

Since the time derivative of the area is zero, the area of  $abc$  must equal the area of  $cde$ .

Far from the obstacle, the flow must return to the undisturbed state. Consider the velocity profile shown in Fig. 3.10. A triangle is a good approximation for a shock consisting of plane waves far from its origin, since the

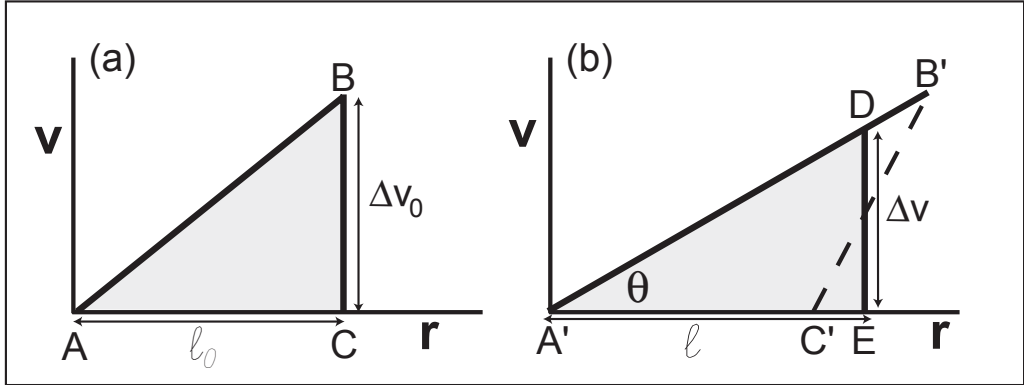


Figure 3.10: Decay of a shock discontinuity as it travels through a material. The area of the shaded triangles must be equal

compressed front moves faster than the relaxing flow behind it. Landau used the constant area of the profile to derive the intensity change of the shock front as it propagates.

In a given time  $t$  point **B** will move  $\alpha t \Delta v_0$  with respect to **C** yielding the triangle  $A'B'C'$  shown in Fig. 3.10(b). As before, the shock profile cannot be multivalued, instead the actual discontinuity will only travel to point **D**. Since the area defined by the discontinuity is constant,  $ABC = A'DE$  which implies

$$l_0 \Delta v_0 = l \Delta v. \quad (3.8)$$

Triangles  $A'DE$  and  $A'B'E$  are similar implying the ratio of any two sides must be equal.

$$\tan \theta = \frac{\Delta v_0}{l_0 + \alpha t \Delta v_0} = \frac{\Delta v}{l}. \quad (3.9)$$

Solving for  $\Delta v$  in terms of  $l, l_0, \Delta v_0$  and setting the area of  $ABC = A'DE$

gives

$$l = l_0 \sqrt{1 + \frac{\alpha t}{l_0} \Delta v_0} \quad (3.10)$$

$$\Delta v = \frac{\Delta v_0}{\sqrt{1 + \frac{\alpha t}{l_0} \Delta v_0}}. \quad (3.11)$$

For large  $t$ , the length of the shock  $l$  increases as  $\sqrt{t}$  and the shock intensity decays as  $\frac{1}{\sqrt{t}}$ .

The same geometric argument applies to discontinuities in cylindrical waves, such as those excited as the rod travels through the layer. The amplitude of any cylindrical wave decays as  $1/\sqrt{r}$ . This decay affects the propagation velocity so that any point in the profile moves with a velocity  $u = c_0 + \alpha v_0 \sqrt{r_0/r}$ .

Consider again the profiles described in Fig. 3.10. The point **B'** prime will exceed point **C'** by

$$\delta r = \int_{r_0}^r \frac{\alpha v_0}{c_0} \sqrt{r_0/r} \, dr \quad (3.12)$$

$$\delta r = \frac{2\alpha v_0}{c_0} \sqrt{r_0} (\sqrt{r} - \sqrt{r_0}). \quad (3.13)$$

Following the same method as used above for plane waves, we set the area of the triangles equal and determine the dependence of  $l$  on  $r$ .

$$l = l_0 \sqrt{1 + \frac{2\alpha v_0}{l_0 c_0} \sqrt{r_0} (\sqrt{r} - \sqrt{r_0})} \quad (3.14)$$

For  $r \gg r_0$ ,  $l \propto r^{1/4}$ . The decrease in intensity of the discontinuity scales as  $\sqrt{r} \Delta v \propto r^{-1/4}$ , yielding a total decrease in intensity of

$$\Delta v \propto r^{-3/4}. \quad (3.15)$$

For a shallow fluid  $\Delta v \propto \sqrt{\Delta h}$ , implying that

$$\Delta h \propto r^{-3/2}. \quad (3.16)$$

The solid line in Fig. 3.8 is a fit to  $\Delta h_{max}$  proportional to  $r^{-3/2}$ . The agreement with Landau's theory for the damping of a discontinuity in a dissipationless fluid is surprising. The bronze particles continuously dissipate energy via inelastic, frictional collisions between particles and between particles and the boundaries. Despite this innate energy loss, the system damps with the same scaling as a compressive shock in a gas with no viscosity.

### 3.7 Time Dependence

High speed images of the layer reveal time dependent behavior in the wake that can not be explained in terms of a simple shallow water approximation. As the rod moves through the layer, it displaces a portion of the granular medium, creating a hump in front of the rod and a dip behind. During the fraction of the driving cycle when the layer is in the air, the dip is prominent. When the layer collides with the plate particles rush in and close the dip creating a peak. The peak remains stationary while the rod continues to move through the layer (Fig. 3.11).

In the determination of the height field shown in Fig. 3.4, we made no effort to resolve the influence of the external driving. The fields are a time average over many cycles where the frequency of the averaging is incommensurate with the frequency of the external driving. Averaging over many plate

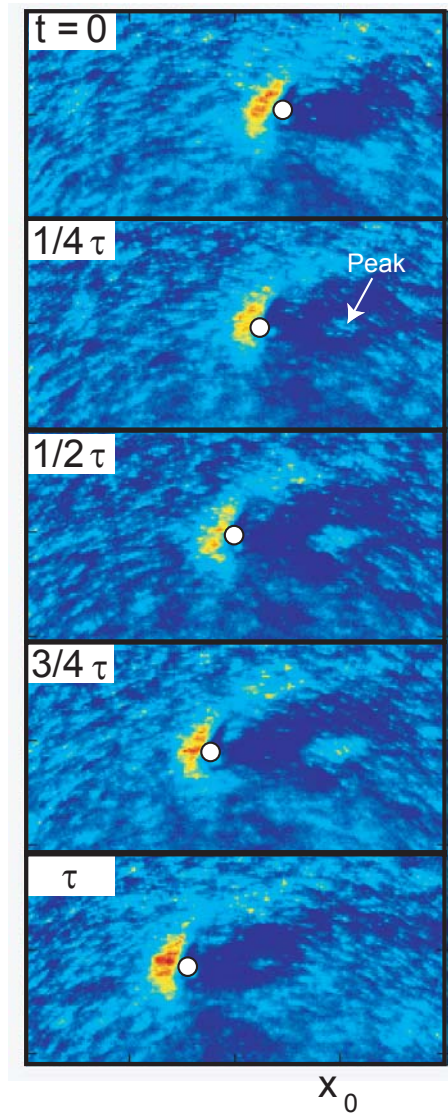


Figure 3.11: High speed images of the wake. The white circles indicate the approximate position of the rod. Red indicates high points of the layer and dark blue indicates depressions. The vertical oscillation of the layer imposes an additional feature on the wake. With each oscillation the depressed region behind the rod collides with the plate and fills forming a small peak at  $x = x_0$ . The peak remains stationary while the rod continues to move with  $v_R$ . On the next oscillation with the plate the old peak is damped and a new one will form at  $x = x_0 + v_R/f$ .

oscillations at an incommensurate frequency yields the additional, oval peak behind the rod seen in Fig. 3.4.

### 3.8 Conclusions

Our experiments demonstrate that a thin vertically vibrated granular layer is described well by shallow water theory for a surface-tensionless fluid. We find that a shock forms on the surface when an obstacle's velocity exceeds the speed of a gravity wave,  $c = \sqrt{gh}$ . The angle of the shock cone is determined by the Mach relation, and the damping of the shock follows the scaling derived by Landau for shocks traveling in a dissipationless fluid. Future experiments should study the applicability of this model as a function of layer depth and inelasticity. For deeper layers, the shock generated when the layer collides with the bottom plate may not travel to top of the layer [46], possibly changing the behavior.

The shocks formed in our experiment are an example of Cerenkov radiation generated by an object traveling through a medium faster than the wave phase velocity [60]. Such radiation leads to increased resistance (wave drag) when a critical velocity is exceeded. Future experiments should examine the dependence of drag on  $v_R$  near the onset of the shock because experiments [19, 134], simulations [18, 129], and theory [24, 99] disagree on this increase in drag.

# Chapter 4

## Methods

In this chapter I discuss the methods employed in our study of granular flow past an obstacle. In the experiment stainless steel particles confined between two glass plates fell under gravity and interacted with an obstacle. We determined the position and velocity of the particles from successive high speed images of the flow. Averaging over many frames yielded bulk flow fields of density, velocity and temperature. We compared the experimental fields to results from molecular dynamics simulations and a numerical solution of the inelastic continuum equations. In this chapter I describe the experimental apparatus, data analysis and simulation techniques.

### 4.1 Flow Past a Wedge Apparatus

A snapshot of the experimental apparatus is shown in Fig. 4.1. In the experiment particles fall through a Hele-Shaw cell (a quasi-2D cell with a width much greater than the plate separation [84]) . The particles are initially distributed on a conveyor belt located above the Hele-Shaw cell. For each experiment, particles fall off the belt into a hopper set on top of the Hele-Shaw cell, through the glass plates and are collected in an aluminum box. A



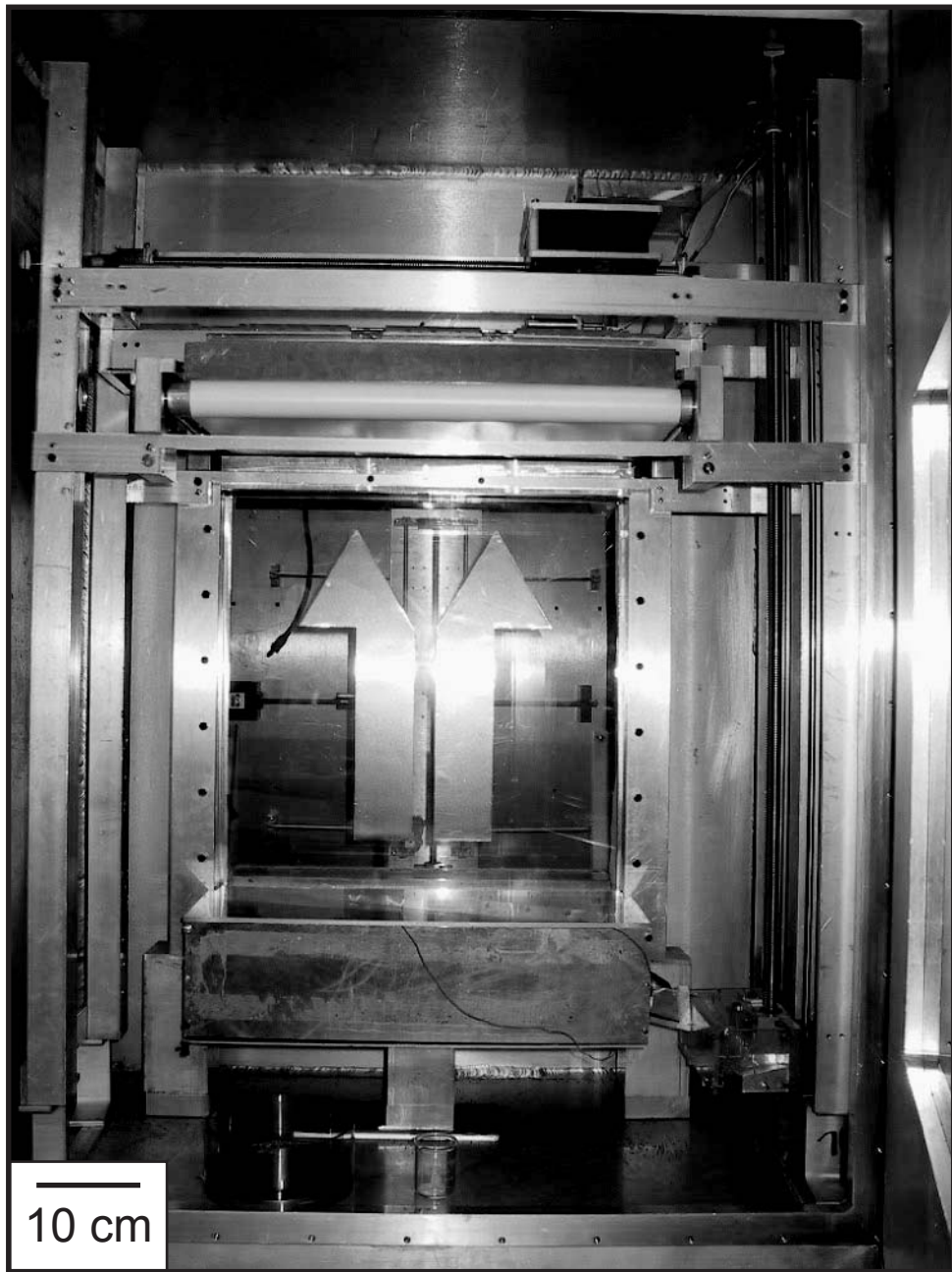


Figure 4.1: A snap-shot of the experimental apparatus. Particles fall past obstacles (in this image two wedges) confined between two glass plates. The Hele-Shaw cell is set in a large, aluminum box that can be evacuated.

detailed description of each of the components is provided below.

#### 4.1.1 Particles

We used stainless steel particles with a diameter  $\sigma = 1.191 \pm 0.002$  mm. The large, non-magnetic (302SS), metallic particles minimized magnetic, electrostatic, and air effects. Stainless steel has a high coefficient of restitution,  $e_0 = 0.96$  for an impact velocity of 1.2 m/s [73]. All of the obstacles and sidewalls were made from non-magnetic stainless steel flat stock.

#### 4.1.2 Hele-Shaw Cell

The granular flow was confined between two  $1.27 \text{ cm} \times 52.7 \text{ cm} \times 52.7 \text{ cm}$  float glass plates. The spacing between the plates was set by two strips of stainless steel flat stock that serve as the side walls for the granular flow. An obstacle made of the same flat stock is located within the experimental cell (Fig. 4.2a). The glass plates are supported and clamped on either side. The top and bottom of the cell remain open.

Float glass plates are rarely square and of uniform thickness. In order to account for these effects we designed a flexible clamping system. The plates rest in a 5.7 cm wide by 2.5 cm deep groove cut into the aluminum clamps set on either end of the glass plates. The stainless steel flat stock is sandwiched between the plates. A thin strip of rubber rests on the outside of each glass plate in order to smooth out the surface. Six screws are located on each side of the clamps. The bottom of the screws rest in shallow holes in the aluminum

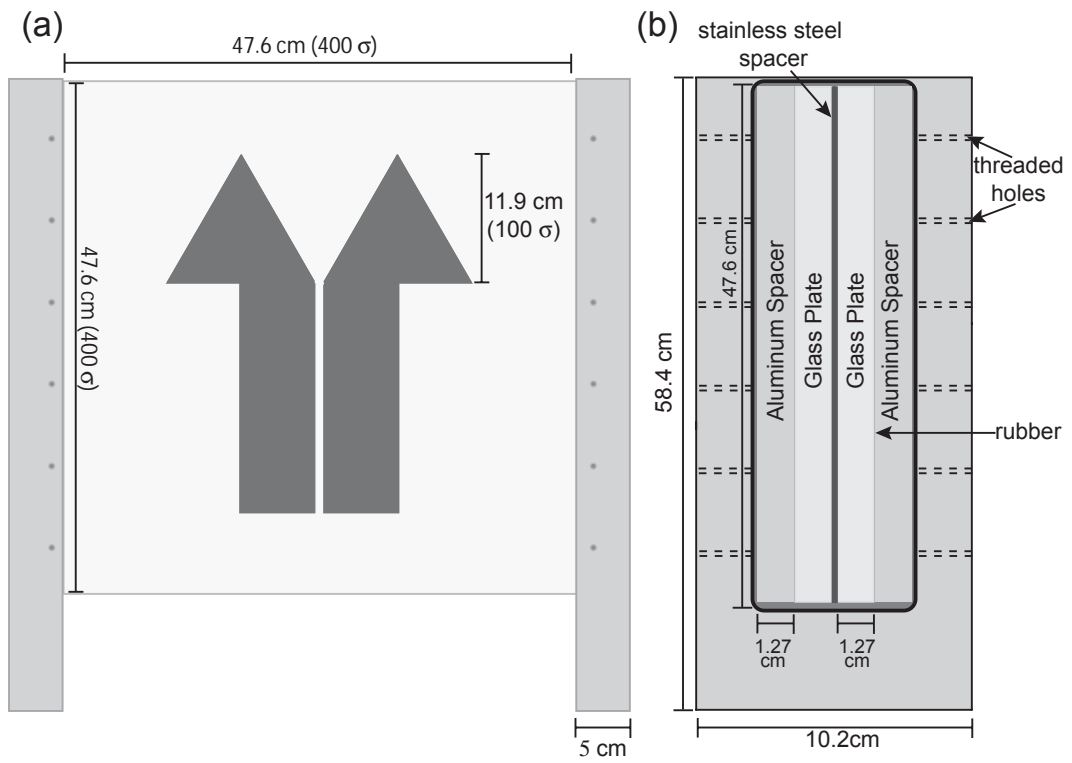


Figure 4.2: Schematic of the experimental cell: a) the Hele-Shaw cell is formed by two 1.27 cm thick glass plates. b) Cross section of the clamps

## Conveyor Belt

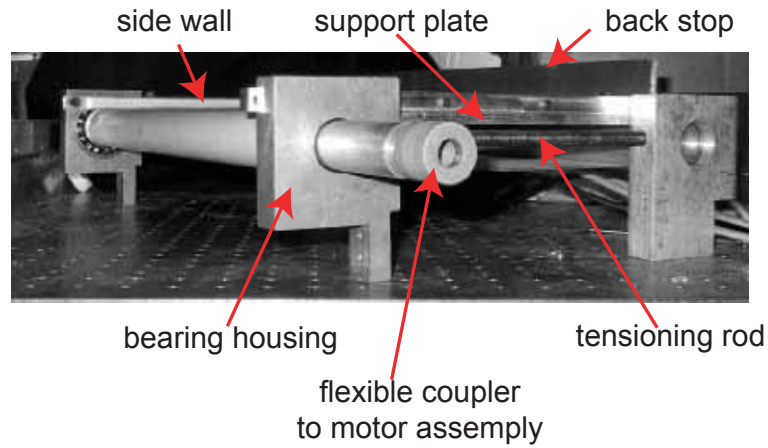


Figure 4.3: image of the conveyor belt

bars. As the screws are turned, the aluminum bars press against the glass clamping them in place. We tighten the screws using a random pattern until the obstacle is held in place purely by frictional forces.

### 4.1.3 Distribution

Before each run particles were distributed on a conveyor belt in a single layer hexagonal close pack crystal. As the belt turned, particles fell off the belt and into a hopper resting on top of the glass plates. The hopper was made of polished aluminum cut at a  $30^\circ$  angle. The edges of the aluminum pieces are set flush with the glass. Particles rattle around the hopper before entering the glass plates, so that the original crystal arrangement is randomized before the flow enters the Hele-Shaw cell.

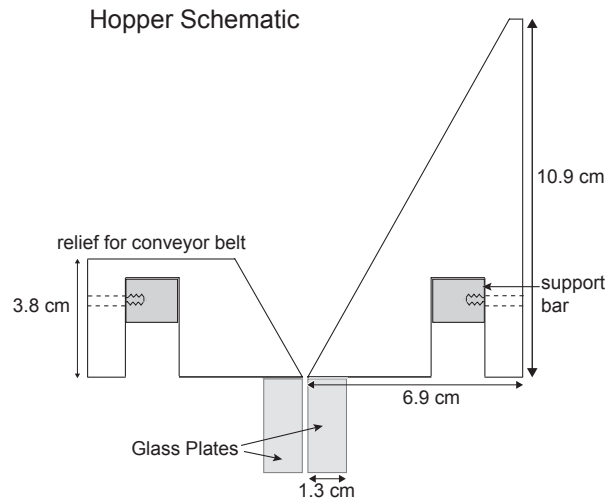


Figure 4.4: schematic of the hopper system

The particle flux into the Hele-Shaw cell was controlled by the conveyor belt velocity and the spacing between the two glass plates. For each gap width, we chose the maximum belt velocity that allowed particles to flow into the cell without jamming.

#### 4.1.4 Lighting

The system was illuminated from behind by a two dimensional array of red LED's with a  $45^\circ$  opening angle. The 1440 LED's are wired in parallel. In order to gain sufficient light for high speed imaging, the LED array requires 25 Amperes of current delivered by a Little Mite power supply. The light is further diffused by frosted glass taped onto the back of the Hele-Shaw cell.

### 4.1.5 Vacuum Apparatus

For the experiments reported in Chapter 5.4.1, we enclosed the Hele-Shaw cell in a vacuum chamber at a pressure 4 Pa. At this pressure the mean free path of a  $N_2$  molecule is 1.6 mm, which is slightly larger than the gap thickness of the Hele-Shaw cell.

The vacuum chamber was a rectangular box (121 cm tall by 91.4 cm wide by 45.7 cm deep) made of 1.27 cm thick aluminum plates. In order to strengthen the chamber, a 5 cm by 2.5 cm aluminum bar stock was welded along the center of each sidewall. At 4 Pa, the maximum deflection of the aluminum plates occurring at the center of the side walls was 0.5 cm.

Windows on either side of the chamber allowed the system to be illuminated from behind with LED array and imaged with a camera located outside the chamber. The windows were made from 7.6 cm thick Plexiglas and lexan. The lexan is slightly stronger but harder to polish than the Plexiglas. We imaged the cell through the Plexiglas window. Each 61 cm by 61 cm window was affixed to the chamber with an O-ring seal, held in place by 44 bolts. Once the windows were attached, they were never removed.

The entire front panel of the chamber served as a door allowing access to the interior. During a vacuum run, the door was sealed to the chamber with an O-ring and 46 bolts.

The chamber was evacuated with an oil based roughing pump. In order to reduce the contamination of the chamber by pump oil, a molecular sieve trap

was placed between the pump and the chamber. A Varian aluminum block valve allowed the chamber to be isolated from the pump. Before evacuating the chamber, the sieve was baked for 24 hours while under vacuum.

The rough pressure is measured inline with the vacuum pump via a convectron gauge. Once the chamber pressure fell below 13.4 Pa, a Varian HT100 sensor connected to a convectron gauge monitored the pressure. The sensor was not inline with the vacuum pump, leading to a more accurate measure of the interior pressure.

Mechanical motion to the conveyor belt was applied through an MDC direct drive rotary motion feed through. The vacuum is maintained by a preloaded o-ring shaft seal. The feed through can be rotated up to 300 rpm, however can only maintain vacuum for torque less than 70 N-cm. The feed throughs are sensitive to lateral and axial load.

## **4.2 Particle Tracking**

We record high speed images of the flow with a Kodak Motioncorder camera. For each experimental run the camera recorded 2173 images of particles separated in time by 1 ms. A series of scripts developed in Matlab with Mark Shattuck were used to locate the particles centers in each frame and to connect particles from one frame to the next. While particle tracking is a commonly used method in experimental physics, the flows studied here present unique difficulties.

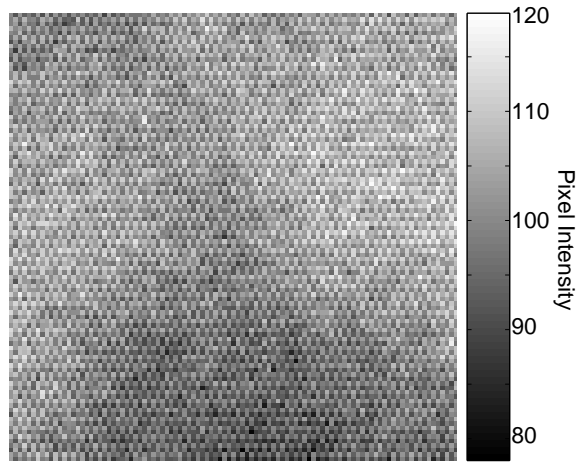


Figure 4.5: Image of a white sheet of paper taken with the Kodak Motioncorder camera. The pixel array is noisy, showing a 2 by 2 square pixel pattern of varying intensity.

First, the Kodak camera is noisy. An image of a white sheet of paper (Fig. 4.5) shows a clear pixel pattern of 2X2 squares of varying intensity. While the wavelength of the pattern remains constant, the pixel values vary in time and are always noticeable in the recorded images. Because of this noise pattern, center finding techniques such as weighted averaging [28, 92, 115] or edge detection [128] must be adapted.

#### 4.2.1 Finding centers

The first step in the image analysis accounts for the non uniform illumination by the LED arrays. Before each data run, we record 100 images of the cell without falling particles. The images are averaged together and serve as the background. We subtract each data image (Fig. 4.6a) from the background



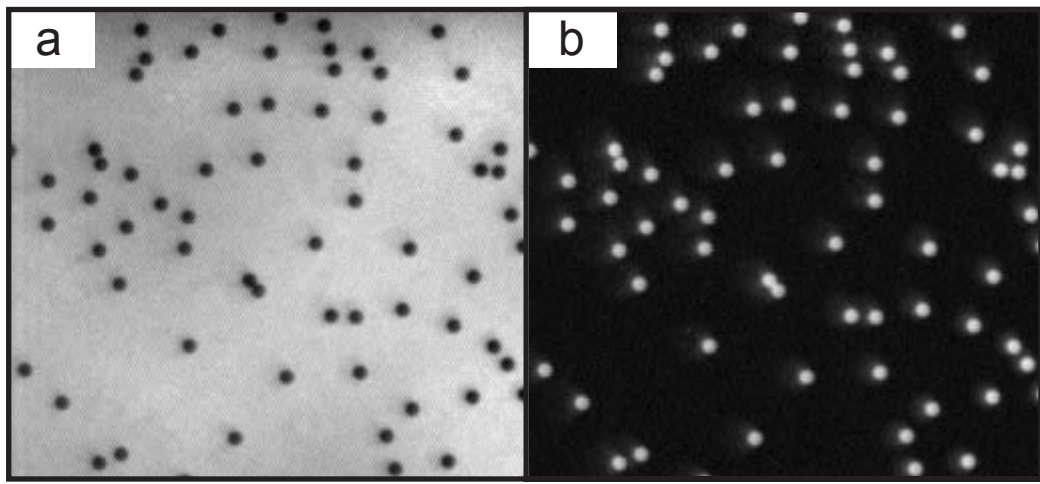


Figure 4.6: (a) A snap shot of the experimental. The image shows an area  $35\sigma \times 34\sigma$  taken from the top and center of the cell. The flow is viewed in transmission, so that particles are dark. Unfortunately the camera has a noise pattern so the particles do not appear as solid disks nor as a Gaussian reflection. The center is not necessarily reflected by the darkest pixel. (b) A background subtracted snap shot shows a more regularly illuminated image.

and divide the result by the background, yielding the more homogeneous image seen in Fig. 4.6b.

For coarse particle tracking, it is often sufficient to call the brightest pixel in a group the center of the particle. Sub-pixel accuracy is determined by weighting the intensities of the surrounding pixels by their distance from the center. The camera noise introduces too much uncertainty in pixel values for this method to return accurate centers. Although the background we subtracted from the image helps remove the variation in lightening, some still persists. Faster moving particles and particles near boundaries appear much darker than others. The brightest pixel technique misses too many particles in each frame, returning inaccurate densities and also causing difficulty determining velocities. We use the brightest pixels above a user adjusted threshold only as a first guess for the particle's center  $p_1$ . Using this guess we determine the typical intensity profile of a particle by averaging a box of pixels centered around  $p_1$  for each particle. The "ideal particle" ( $ip$ ) determined by this method is shown in Fig. 4.7(a).

The image in Fig. 4.6(b) can be thought of as a convolution of delta functions located at the particle centers and  $ip$ . In order to determine the location of the centers, we deconvolve the image with  $ip$ . The deconvolution of Fig. 4.6(b) and  $ip$  is shown in Fig. 4.7(b). The brightest pixels in the deconvolution, above a certain threshold, are considered the second guess for the particle centers  $p_2$ . This method resolves most particles including those in dense clusters.

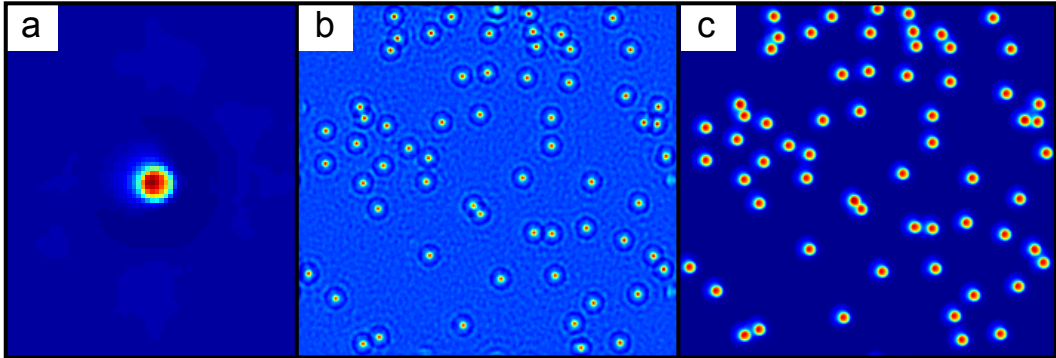


Figure 4.7: **a** An image of the average particle,  $ip$  detected by the camera. This image is used to deconvolve the original images, yielding bright pixels at the center of each particle in the frame **b**. Subpixel resolution is determined by minimizing the difference between the actual image from an image created by  $ip$ 's.

To refine the positions  $p_2$  to sub-pixel accuracy, we create an "ideal image" consisting of  $ip$  located at each point in  $p_2$ . We minimize the difference between the ideal image and the actual image.

#### 4.2.2 Determining Velocities

We determine the velocities of the particles by matching the location of a particle in one frame with its location in the next frame. Matching the particles is non trivial, as strong velocity gradients in the flow imply particles can move more than their diameter between frames. In addition particles can collide or pass each other between frames. Finally, particles are free to enter or leave the frame.

We determine particle pairings with a multi step process. First we

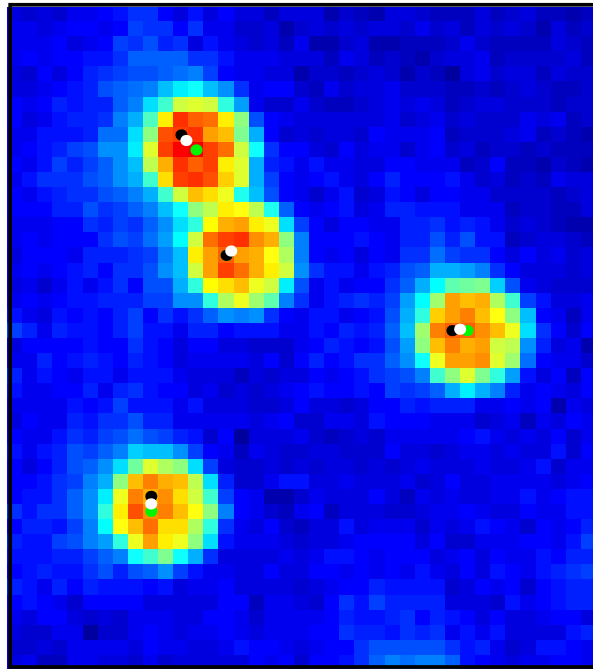


Figure 4.8: Location of the particle center determined at each of the three stages:  $p_1$  green,  $p_2$  black, and  $p_3$  white.

make an initial guess, matching a particle in frame  $n$  to the particle in frame  $n + 1$  closest to the original location. If the particle is closest to a boundary, the match is to that boundary. The pairing must be one to one. If two or more particles pair with a particle in  $n + 1$ , then the matches are readjusted to minimize overall distance between particles. This process is repeated until the pairing is 1 to 1. With the initial guess in hand, we average over all initial guesses and build an average flow field. The pairing process is repeated, however instead of choosing simply the closest particle, we use the velocity field to predict where a particle in frame  $n$  should be in frame  $n + 1$ . This process is repeated until no particle matches are changed. The typical number of repeats for dense systems is four. See Fig. 4.9.

### 4.2.3 Building average flow fields

For the flows considered in Chapter 5 we create average flow fields on a sub-pixel grid. Each time a particle is located in a grid, the number count is incremented by one and the velocity by the velocity of the particle. This procedure is repeated for at least 16000 frames. A particle should not simply be represented by its center, the whole particle contributes to the flow. We adjust for this by convolving the flow field with a Gaussian corresponding to the particle size. An example of an experimentally determined flow field is shown in Fig. 4.10.

The above method to compute the average flow fields works well for dilute flows. For high density flows, the finite size of the particles is evident

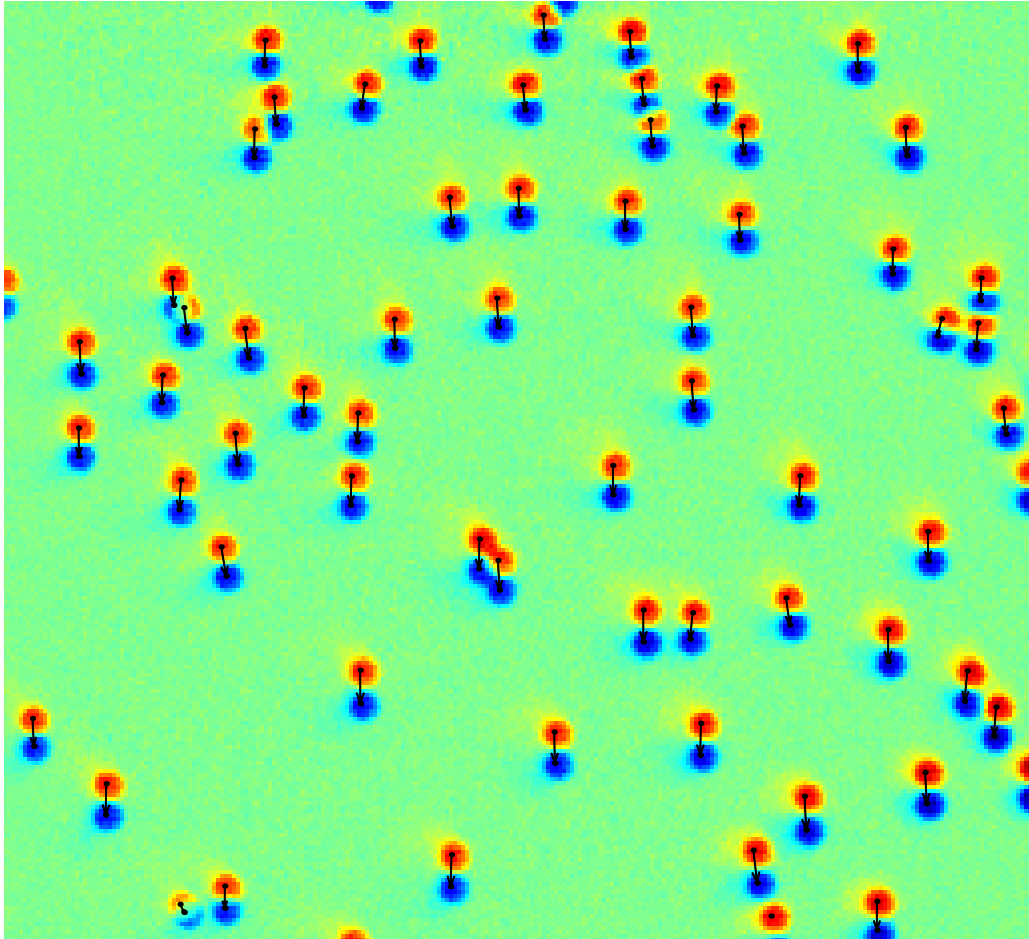


Figure 4.9: We match particles from one frame to another. Red are particles in the first frame. Blue particles in the second. Arrow connects the dots. Particles are allowed to come in and leave through all of the walls.

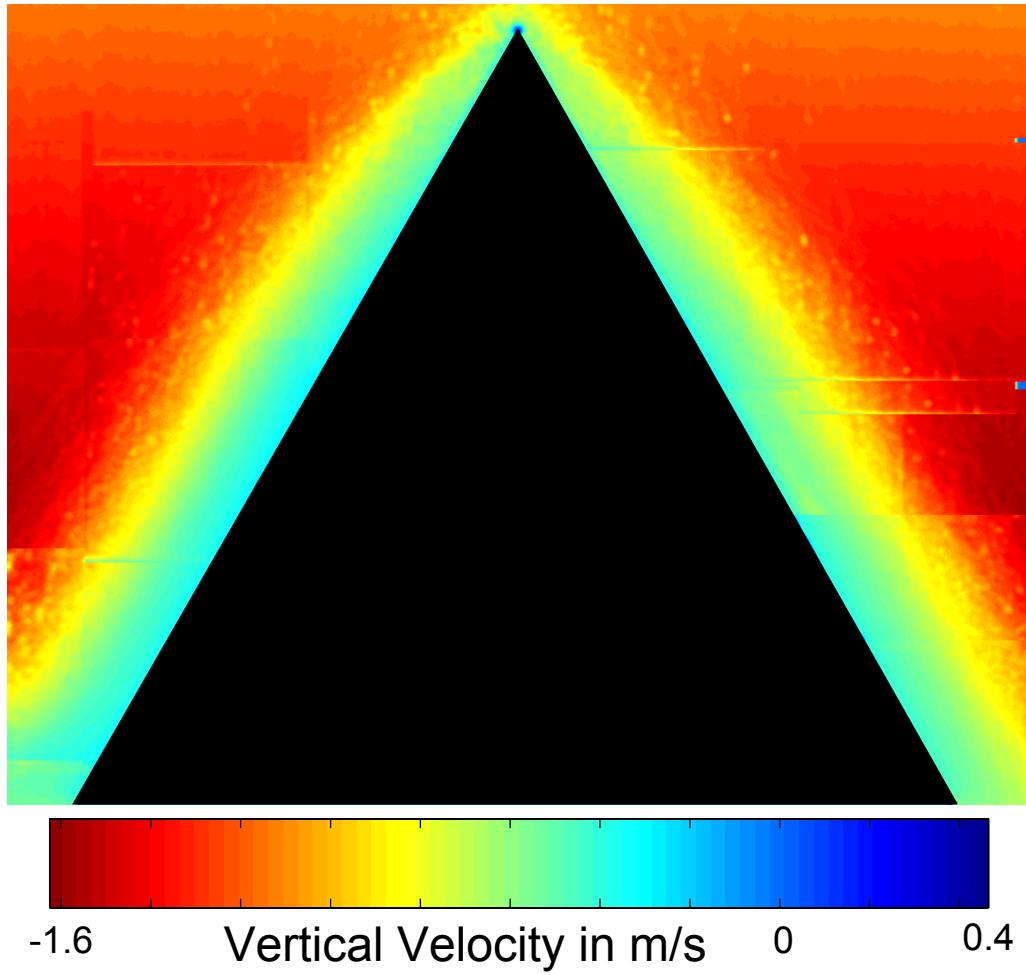


Figure 4.10: Average vertical velocity flow field determined from time-averaged particle tracks. The image shows a  $125\sigma \times 100\sigma$  region.

in the smooth fields making it difficult to compare to continuum theory which does not recognize a particle length scale in the flow fields. In this regime we compute the voronoi tessellation for all particle centers in a frame (Fig. 4.11). Each polygon represents the area of the cell which is closest to that particle. The flow density of each polygon equals  $1/\text{area}$  of the polygon, and the velocity of the polygon is the particle's velocity [90, 111].

In order to average over many realizations of a flow, the information contained in the tessellated frame must be mapped to a steady structure. We map each frame to a square grid with grid spacing equal to  $\sigma$ . If a grid spacing falls entirely within a polygon, the density and velocity associated with that polygon is assigned to the grid location. If instead, the grid spacing only partially falls within the polygon, we assign a fraction of the value associated with the polygon to the grid spacing. We determine the appropriate fraction by dividing the original grid space into a 10 X 10 rectangular array and computing how many of the vertices of the array fall within the polygon. Fig. 4.11 shows the average of 8 realizations of a flow computed in this manner.

We compare the experimentally determined averaged flow fields of volume fraction, velocity and temperature to continuum theory. The bulk temperature at a grid point is defined as the second moment of the local distribution function. In order to get a reliable temperature, we need to average over sufficient particles to adequately sample the local distribution function. The dependence of the measured temperature on the number of particles used to compute  $T$  is shown in Fig. 4.12. A reasonable  $T$  may be determined with 8



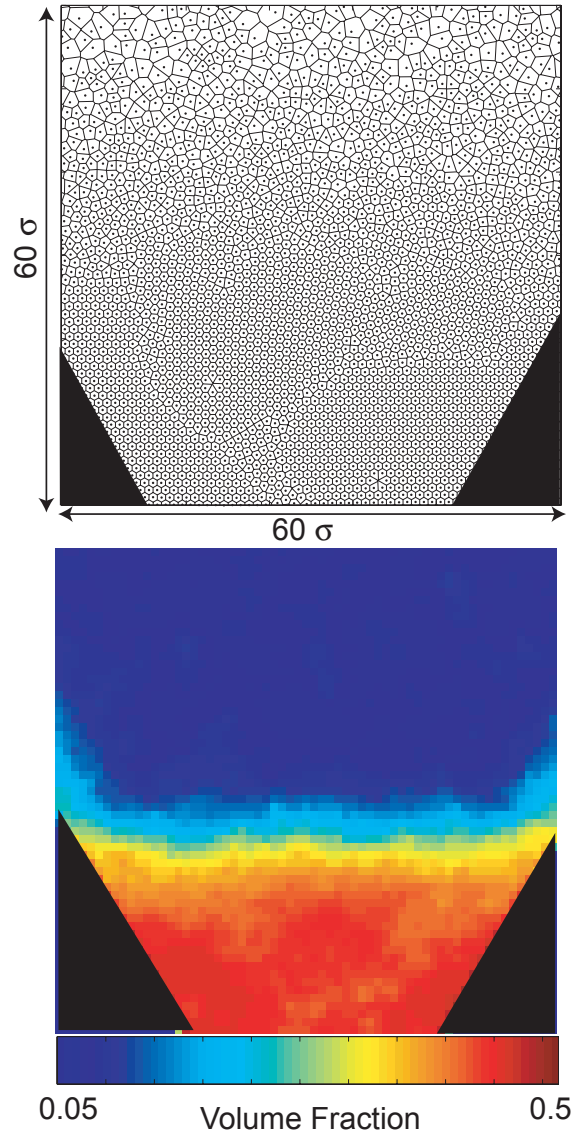


Figure 4.11: **Top** zoomed in region on the exit of a funnel. The black regions correspond to portions of two wedges defining the funnel. The bottom of the wedges are separated by  $12\sigma$ . Near the opening of the funnel, the grains are in a crystal configuration. We compute the voronoi tessellation, such that each polygon defines the area closest to the particle contained within the polygon. The density of the flow inside a polygon is  $1/\text{area}$ . We average over many realizations of this flow to determine the average flow field. **Bottom** The average volume fraction field determined by the tessellation technique.

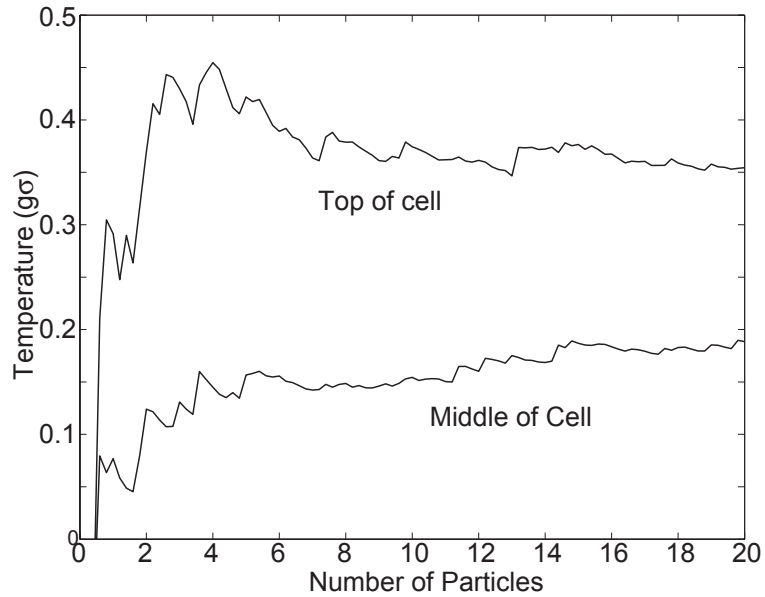


Figure 4.12: MD simulation results for the temperature,  $T$ , at the top and middle of a quasi-2D cell. We plot the dependence of the measured  $T$  on the number of particle velocities used to compute  $T$ . For number of particles,  $N < 8$ , the recorded value of the temperature is incorrect.

or more particles. For the results presented in this thesis, each  $T$  value was computed from at least 16 particles.

In order to have sufficient resolution for particle tracking, we can not image the entire  $400\sigma \times 400\sigma$  flow field at once. Instead, we piece together the field from smaller, zoomed in images of  $33\sigma \times 35\sigma$ . Before moving the camera, we image a ruler placed in the field of view of the camera. The ruler remains in place while the camera is moved. We can reconstruct the location of the field by matching the rulers from each region.

### 4.3 Molecular Dynamics Simulation

We compared experimental results to an event driven, hard sphere molecular dynamics simulation developed by Joe Newman and Chris Bizon. The code was validated against experiment for the vertically vibrated granular layers [11] and adapted by Bizon for the wedge geometry.

In the simulation, particles follow parabolic trajectories and interact through instantaneous, binary collisions. The collision model, developed in [127], conserves both linear and angular momentum but allows energy dissipation by inelastic and frictional collisions [127]. At a collision the velocities are decomposed into their relative normal ( $\mathbf{v}_n$ ) and tangential ( $\mathbf{v}_t$ ) components. The relative displacement vector  $\hat{\mathbf{r}}_{12}$  defines the distance between particles located at  $\mathbf{r}_1$  and  $\mathbf{r}_2$ .

$$\hat{\mathbf{r}}_{12} = (\mathbf{r}_1 - \mathbf{r}_2) / |\mathbf{r}_1 - \mathbf{r}_2|, \quad (4.1)$$

$$\mathbf{v}_n = ((\mathbf{v}_1 - \mathbf{v}_2) \cdot \hat{\mathbf{r}}_{12}) \hat{\mathbf{r}}_{12} \quad (4.2)$$

$$\mathbf{v}_t = \hat{\mathbf{r}}_{12} \times ((\mathbf{v}_1 - \mathbf{v}_2) \times \hat{\mathbf{r}}_{12}). \quad (4.3)$$

The relative surface velocity at the collision  $\mathbf{v}_s$  for spheres of diameters  $\sigma$  is

$$\mathbf{v}_s = \mathbf{v}_t + \hat{\mathbf{r}}_{12} \times \sigma/2 (\mathbf{w}_1 + \mathbf{w}_2), \quad (4.4)$$

where  $\mathbf{w}_1$  and  $\mathbf{w}_2$  are the particles angular velocities.

The change in a particle's normal velocity from a collision is found by conserving linear momentum and reducing the normal component of the

velocity by the coefficient of restitution:

$$\Delta \mathbf{v}_{1n} = \frac{m_{12}}{m_1} (1 + e) \mathbf{v}_n \quad (4.5)$$

$$\Delta \mathbf{v}_{2n} = -\frac{m_{12}}{m_2} (1 + e) \mathbf{v}_n, \quad (4.6)$$

where  $m_{12}$  is the average mass.

The tangential velocity is changed by two processes: it is reduced because of sliding friction and is coupled to the angular momentum because of rolling friction. The frictional interaction of the grains causes a reduction in the relative surface velocity between particles. In addition, energy of the collision can be stored in tangential strain at the contact region, causing a reversal in the relative surface velocity.  $\beta$  takes all of this into account

$$\beta = \min[\beta_0, -1 + \mu(1 + e)(1 + 1/K)v_n/v_s], \quad (4.7)$$

where  $\beta_0$  is the maximum tangential coefficient of restitution. For sliding friction, the tangential impulse is assumed to be given by the normal impulse multiplied by  $\mu$ .

$$\Delta \mathbf{v}_{1t} = \frac{m_{12}}{m_1} \frac{K(1 + \beta)}{(K + 1)} \mathbf{v}_s \quad (4.8)$$

$$\Delta \mathbf{v}_{2t} = -\frac{m_{12}}{m_1} \frac{K(1 + \beta)}{(K + 1)} \mathbf{v}_s \quad (4.9)$$

$$\Delta \mathbf{w}_1 = \frac{\sigma}{2I} \frac{m_{12}}{m_1} \frac{K(1 + \beta)}{(K + 1)} \hat{\mathbf{r}}_{12} \times \mathbf{v}_s \quad (4.10)$$

$$\Delta \mathbf{w}_2 = -\frac{\sigma}{2I} \frac{m_{12}}{m_2} \frac{K(1 + \beta)}{(K + 1)} \hat{\mathbf{r}}_{12} \times \mathbf{v}_s, \quad (4.11)$$

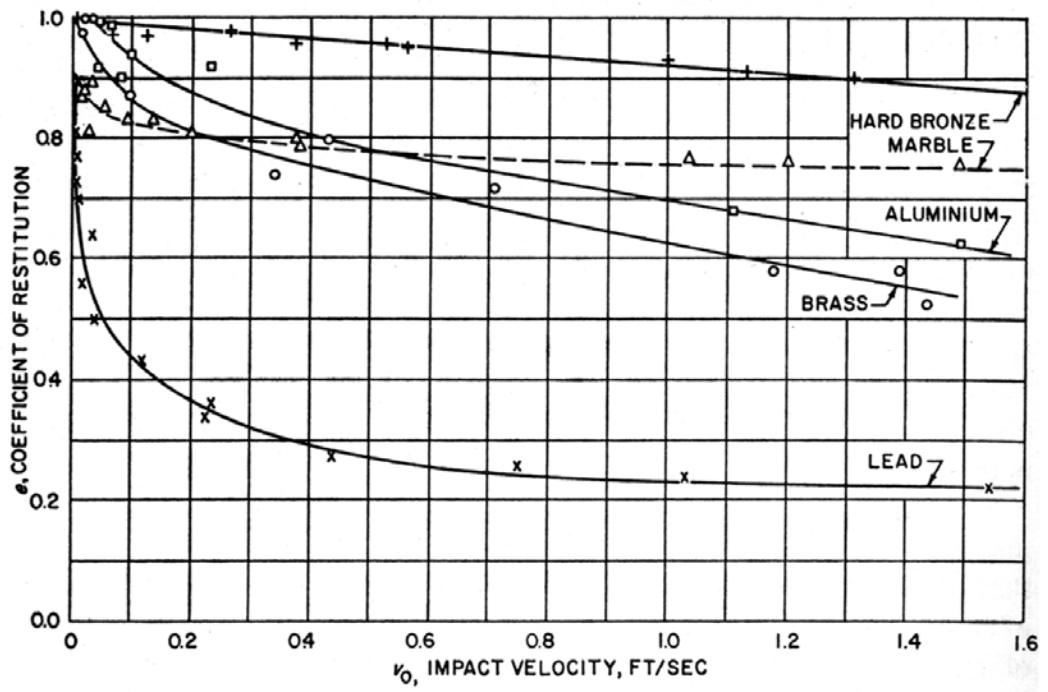


Figure 4.13: The coefficient of restitution is velocity dependent (figure from [50]).

where  $I$  is the momenta of inertia about the center of a sphere ( $\frac{1}{10}m\sigma_2$ ) and  $K = 4I/(m\sigma^2)$  is a geometrical factor relating the momentum transfer from translational to rotational momentum.

Experimental studies of the impact of spheres show that the coefficient of restitution depends on the relative velocity of the impact, as Fig. 4.13 illustrates. As the relative collision velocity tends to zero,  $e$  tends to unity. For the initial study of rapid granular flow past a wedge presented in chapter 5, the granular flow fields did not show any difference between velocity independent and velocity dependent runs. For our initial comparison with hydrodynamic theory (which assumes a constant  $e$ ) we set  $e = e_0$ . However for dense granular flows a constant  $e$  causes a numerical instability referred to as inelastic collapse [75, 76], where a particle can have an infinite number of collisions in a finite time. To prevent this artifact we allow the coefficient of restitution to be 1 if a particle collides within a time  $3 \times 10^{-4} \sqrt{\sigma/g}$  of the previous collision [77]. For collisions with small relative velocities  $v_n < \sqrt{0.2g\sigma}$ , the coefficient of restitution varies as  $1 - (1 - e_0) (v_n/\sqrt{g\sigma})^{3/4}$ . Otherwise,  $e = e_0$ .

Collisions with the boundaries are treated in the same way as collisions with other particles, however the boundary has infinite mass and the collision parameters  $e, \beta$ , and  $\mu$  are defined independently.

The molecular dynamics simulation mimics the experimental geometry. Particles are introduced into the top of the box at a specified rate. The initial horizontal location of the particle is chosen randomly and the initial velocity of the particle is chosen from a Gaussian distribution with a nonzero mean

velocity in the direction parallel to gravity. The width of the distribution, the input rate of particles, and the mean vertical velocity are chosen in order to match the measured experimental conditions of  $\nu, v_z$  and  $T$  measured  $42\sigma$  above the wedge. The width of the Gaussian distribution perpendicular to the confining plates was reduced by  $\alpha$ , where  $\alpha$  was altered in order to fit the free stream flow.

#### 4.4 Continuum Equation Solver

We compare experimental results for the wedge geometry with a numerical solution of the Jenkins and Richman equations presented in Chapter 2. The initial code was written by Mark Shattuck and reported in [101]. The equations were solved on a 2-D grid via a second order space and first order time accurate finite difference solver. We solved the 3D equations, but all derivatives along the third direction (perpendicular to the plates) were assumed to be zero. Euler time stepping was applied. Since the experimental flow reaches a steady state, the continuum simulation is run from the initial conditions until the system reaches a steady state where the mass flux is constant to 0.01%

We use a rectangular grid with spacing such that the grid points fall exactly on the wedge boundary. For the experimental comparison presented in Chapter 5, we used a wedge with half-angle  $\theta = 30^\circ$  centered on a  $504 \times 194$  grid where  $\Delta x = 0.61\sigma$  and  $\Delta z = 1.0417\sigma$ .

#### 4.4.1 Boundary Conditions

The boundary conditions at the inlet to the Hele-Shaw cell were specified from the experiment ( $\nu_0 = 0.0145$ ,  $V_0 = 0.6387$  m/s,  $T_0 = 0.0176$  (m<sup>2</sup>/s<sup>2</sup>) and at the outlet were unspecified. At the side walls, the boundary conditions were periodic.

Along the wedge we used a slip boundary condition on the velocity, such that the ratio of the tangential strain to normal strain was equal to one. The wedge is "colder" than the surrounding granular fluid, so there is a net heat flux into the wedge. We followed Jenkins and Askari [62] and set the heat flux to be proportional to the local volume fraction  $\nu$  and  $T^{3/2}$ . This relationship is only expected to hold true for dilute flows. We measured the proportionality constant directly from the MD simulations and found  $k = 0.2$ .

The appropriate boundary condition at the wedge tip was difficult to determine. Three regions of the granular flow converge on the wedge tip: the free stream particles which have not yet interacted with the wedge and particles bouncing off either side of the wedge. Results from MD simulations show the velocity distributions within  $2\sigma$  of the wedge have a different functional form than the surrounding flow.

We designed the grid so that the wedge tip falls between evaluated points. At the wedge tip, the flow parameters are set to be equal to the value found in MD simulations. However, results from the MD and continuum simulation are most different near the tip. The MD simulation shows a bulb of



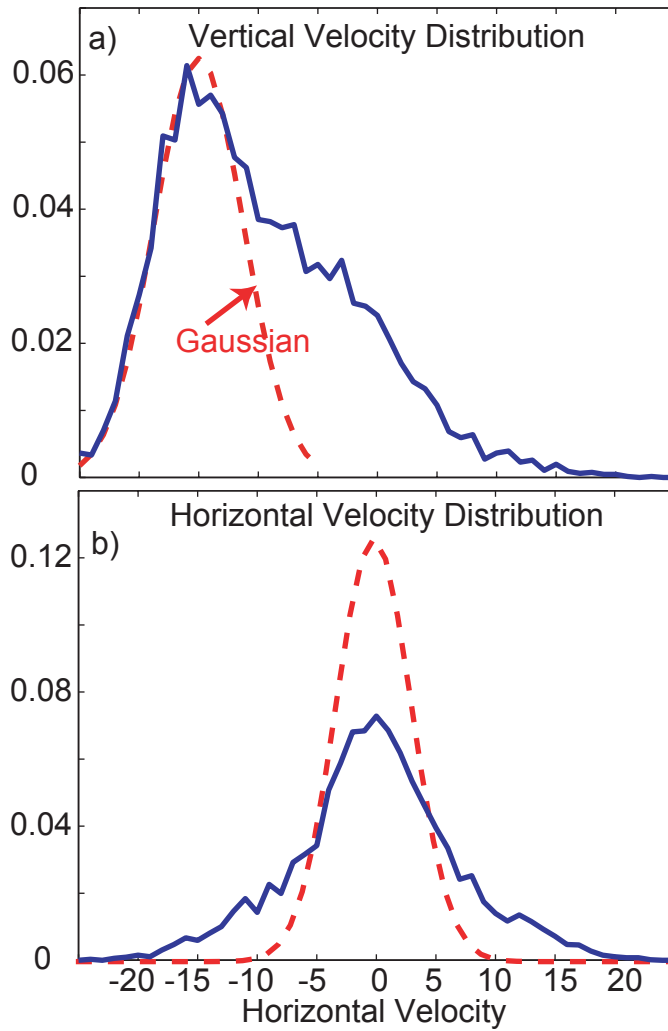


Figure 4.14: Velocity Distribution of particles within  $2\sigma$  of the wedge tip determined from MD simulation. The Gaussians fits are determined from the temperature and mean values in the free stream region near the tip.

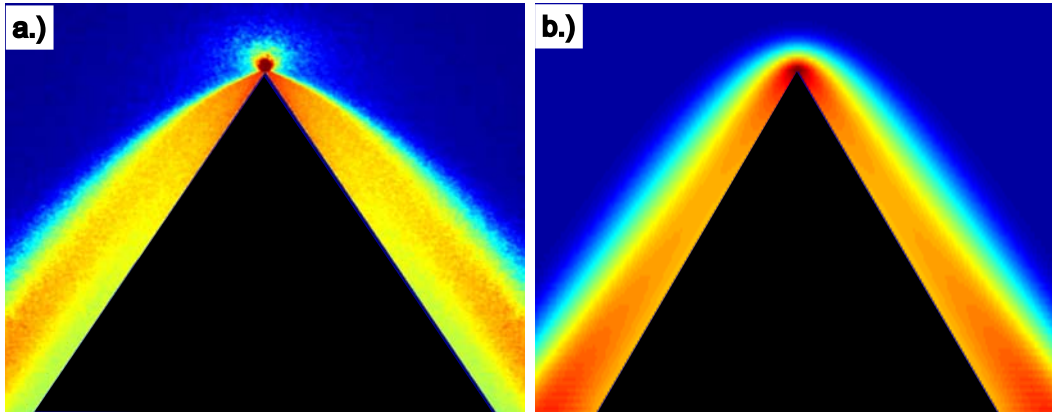


Figure 4.15: Temperature fields for a). molecular dynamics simulation and b). continuum equations. Each simulation handles the tip differently, leading to poor agreement in the vicinity of the wedge tip.

hot material with a rapidly cooling halo. The continuum results gives a more typical bow shock structure.

The slip boundary condition applied along the wedge causes difficulties at the bottom corners. This condition allows the boundary to exert an unphysical pull on the granular fluid. Because of the inappropriate boundary conditions, the flow at the bottom corners was unstable. We chose not to compare to the continuum solution within  $2\sigma$  of the bottom of the wedge. Future work will employ a different boundary condition on the surface, which should improve stability.

# Chapter 5

## Flow Past A Wedge

*Portions of this chapter have been published in Physical Review Letters [101]*

### 5.1 Abstract

We measure time-averaged velocity, density and temperature fields for steady granular flow past a wedge. We find the flow to be supersonic with a speed of granular pressure disturbances (sound speed) equal to about 10% of the flow speed, and we observe shocks nearly identical to those found in a supersonic gas. Molecular dynamics simulations of the experimental geometry yield fields in quantitative agreement with experiment. A numerical solution of the inelastic continuum equations is only in qualitative accord with the experiment, but agrees quantitatively with a molecular dynamics simulation for the experimental conditions excluding wall friction.

### 5.2 Introduction

A classic problem for supersonic flows of an elastic gas is the shock formed when the flow encounters a wedge [5]. In the free stream the flow stream

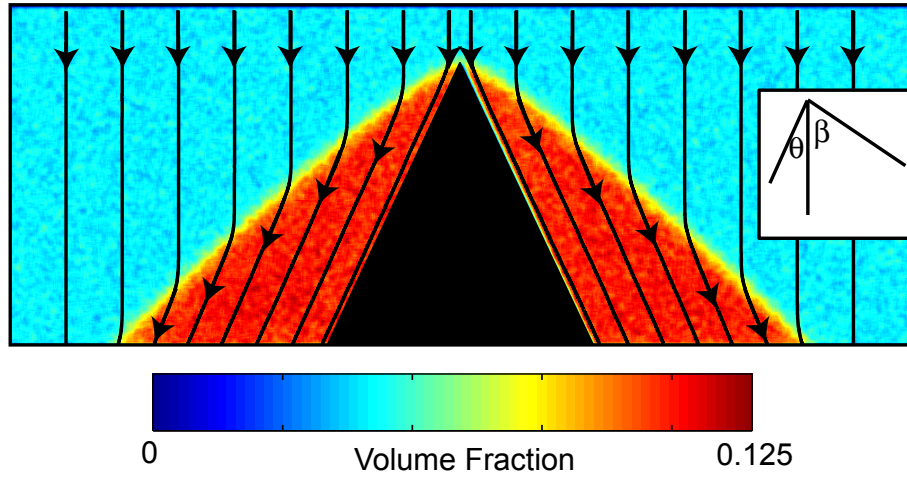


Figure 5.1: MD simulation of a supersonic *elastic* gas interacting with a wedge of half angle  $\theta = 20^\circ$ . The flow is incident on the wedge with a Mach number of 2.5. Impenetrable boundary conditions at the surface of the wedge require the flow stream lines behind the shock to be parallel to the wedge surface. The shock extends outward into the fluid at an angle  $\beta$  with respect to the incident flow.

lines are parallel and incident on the wedge. At the shock the streamlines are deflected through an angle  $\theta$  and aligned parallel to the wedge surface. Across the shock the Mach number decreases and the pressure, temperature and volume fraction increase. The shock surface extends outward into the flow with at an angle  $\beta$  with respect to the initial incident streamlines (Fig. 5.1).

If the incident flow is steady, inviscid, and isothermal, than the shock angle  $\beta$  may be determined by the free steam Mach number and the half-angle of the wedge  $\theta$ . The  $\theta - \beta - Mach$  relation for an elastic gas is shown in Fig. 5.2. For each incident Mach number, there exists a maximum deflection angle  $\theta_{max}$ . If the geometry requires the stream lines to be deflected through

an angle  $\theta > \theta_{max}$ , then no straight line shock solution exists, instead a normal shock is created in front of the obstacle, curving as it extends into the fluid. For a Mach 5 flow,  $\theta_{max} = 41.5^\circ$ .

In this chapter we examine the shock formed when a granular flow encounters a wedge. We first present the experimental setup and the results. We compare experimental shock profiles with those computed via MD simulation and the inelastic continuum equations. Finally we describe how the oblique shock formed in the granular flow differs from the elastic gas analog.

### 5.3 Experiment

In the experiment, stainless steel spheres (particle diameter  $\sigma = 1.2$  mm) fell under gravity past a wedge sandwiched between two glass plates separated by  $1.6\sigma$ . The particles were initially distributed uniformly on a conveyor belt. As the conveyor turned, particles fell off into a hopper that guided the particles into the cell formed by the closely spaced plates; the wedge was located a distance of  $42\sigma$  below the top of the cell. The positions and velocities of the particles were determined from high speed images of the falling particles, and data from many thousands of particles were averaged to obtain the time-independent velocity, volume fraction, and temperature fields.

We computed the average free stream speed of sounds from our measurements according to Eq. 1.4. The sound speed for flow incident on the wedge was 0.09 m/s. The flow entered the top of the cell with a Mach number of 7 and accelerated under gravity to a Mach number of 12 at the tip of the

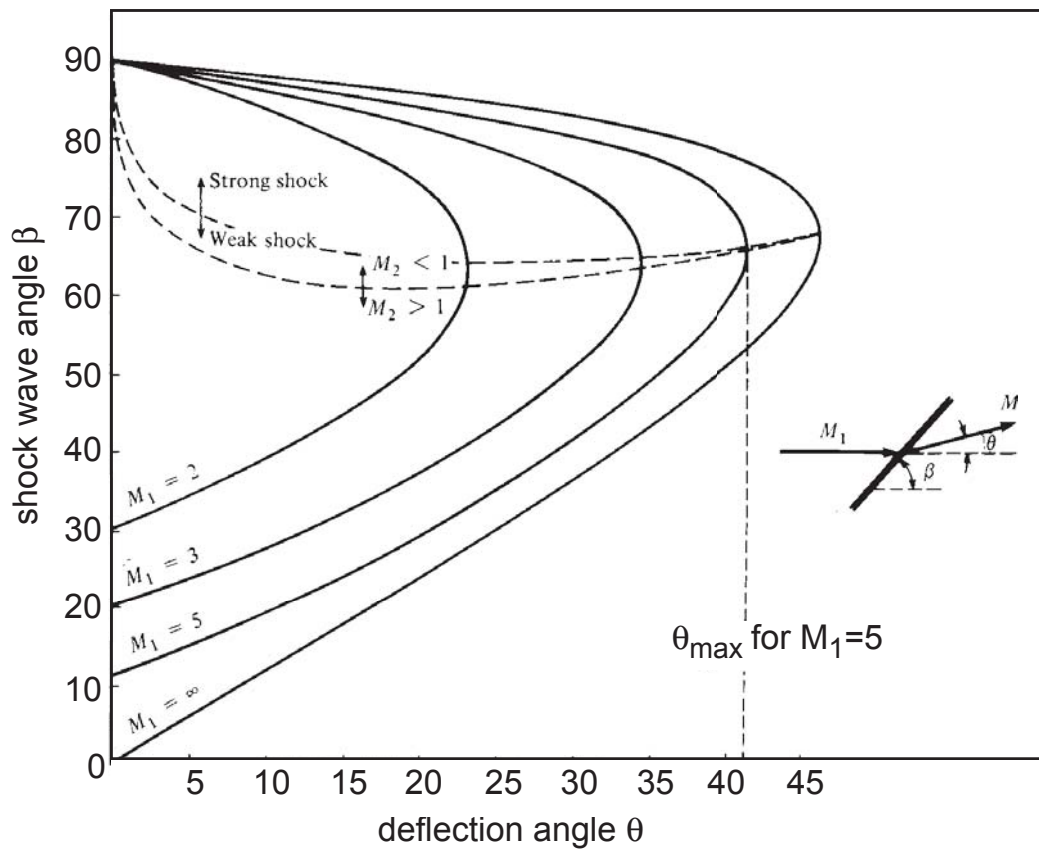


Figure 5.2: The  $\theta - \beta - Mach$  relationship for elastic, oblique shocks. Figure taken from Anderson [5].

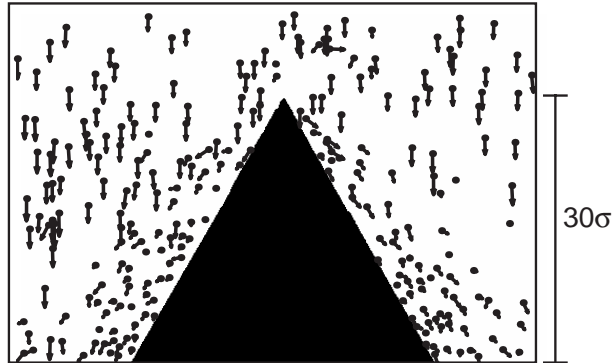


Figure 5.3: An observed image of granular flow incident downward on a wedge, where the particle positions and velocities (denoted by arrows) are determined from images separated by 1 ms. The longest arrow corresponds to a velocity of 1.65 m/s. The figure  $68\sigma$  by  $45\sigma$  shows the top  $30\sigma$  of a wedge of total height  $100\sigma$ .

wedge.

The horizontal velocity field measured in the experiment is shown in fig. 5.4(a). A shock separates the undisturbed region, where the horizontal velocity is nearly zero, from the compressed region, whose stream lines follow the flow around the obstacle. Because of gravity and inelasticity, the shock does not extend out at a constant angle but curves towards the wedge.

At the bottom of the wedge the compressed gas expands in a fan-like structure as the volume available to the flow increases (fig. 5.5). In an expansion fan the density and temperature decrease and the Mach number increases. The expansion fan is a smooth transition radiating from the bottom corner of the wedge.

The flow was computed numerically in a three-dimensional MD simu-

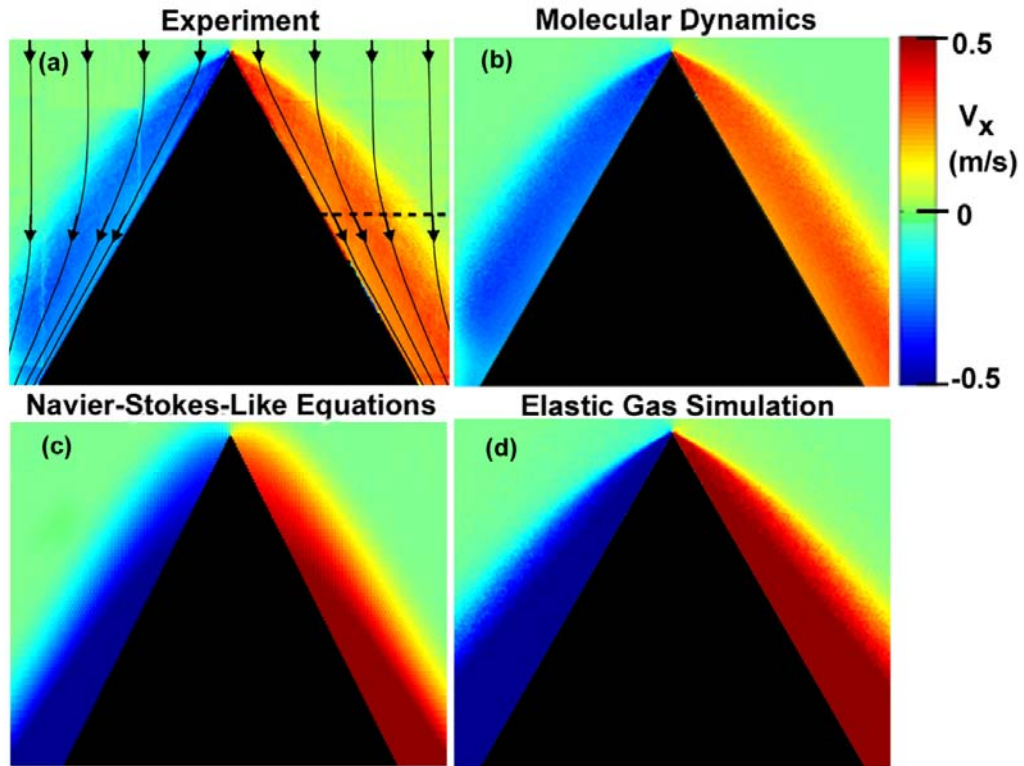


Figure 5.4: Horizontal component of the velocity field of a granular flow incident downward on a wedge, determined by three methods: (a) experiment, (b) MD simulations, and (c) integration of inelastic continuum equations. (d) MD simulation of an elastic gas in a gravitational field is included for reference. Each picture shows a region  $130\sigma$  by  $104\sigma$ . The solid lines with arrows denote streamlines. Quantitative comparisons along the dashed line in (a) are shown in figs. 5.6 and 5.7 [101].



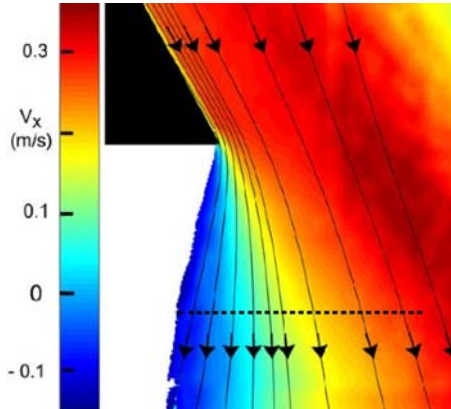


Figure 5.5: The horizontal velocity field measured for the expansion fan that formed when the supersonic granular flow reached the bottom of the wedge. The solid lines indicate selected streamlines. The total height of the region shown is  $55\sigma$ . The white region below the wedge had too few particles for the velocity to be determined [101].

lation (fig. 5.4(b)) and in a two-dimensional finite difference simulation of the inelastic continuum equations (fig. 5.4(c)). The two simulations yield results for the horizontal component of velocity in qualitative accord with experiment: a shock forms at the tip of the obstacle, and behind the shock the flow is compressed, has a higher temperature, and lower mean velocity. Quantitative comparisons among the methods are plotted in figs. 5.6 and 5.7 for values of the fields along the dashed line shown in fig. 5.4(a).

Three parameters were adjusted in the MD simulation to achieve the agreement with the experiment shown in figs. 5.6. The same coefficient of restitution  $e_0 = 0.97$  and friction coefficient  $\mu = 0.15$  were used to model inter-particle and particle-wall collisions. The initial conditions of the experi-

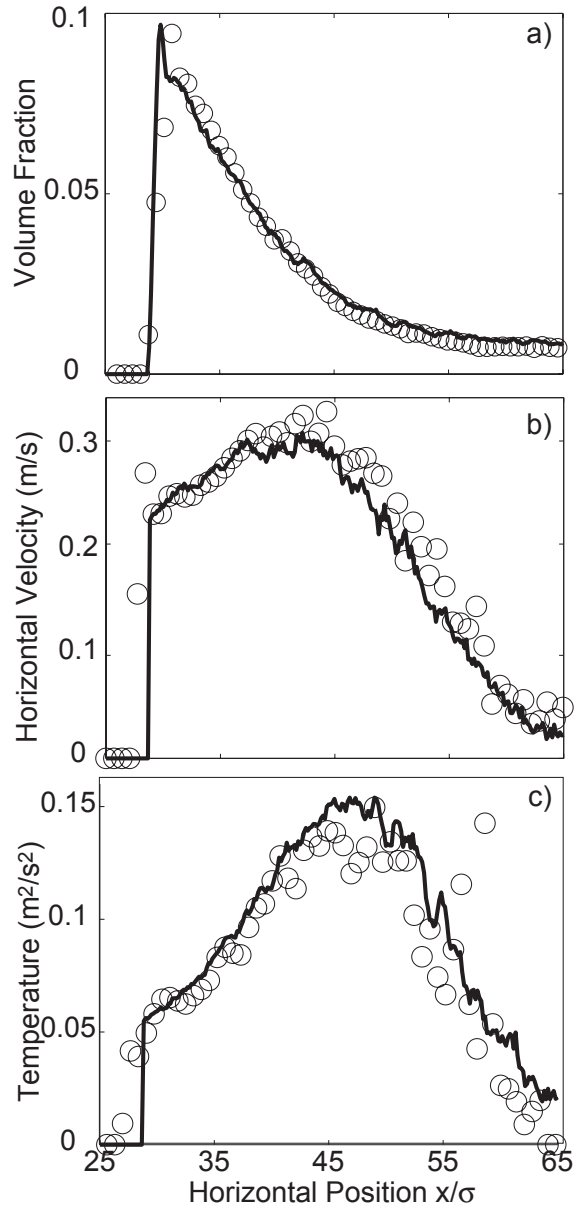


Figure 5.6: Shock profiles for granular flow past a wedge measured in an experiment (circles) are compared with results from molecular dynamics (solid lines): (a) volume fraction, (b) horizontal component of the velocity, and (c) temperature. The profiles are taken along the dashed line in fig. 5.4 [101].

ment were modeled by placing particles into the top of the cell at a constant rate. Incoming particles were placed randomly at the top of the cell with a mean downward velocity measured from the experiment, and fluctuations were chosen from a Gaussian distribution determined by the measured temperature. An additional parameter  $\alpha$ , defined as the ratio of temperature perpendicular to the wall to that parallel to the wall, was set to 0.8. These parameters, which were not measured in the experiment, were adjusted to provide agreement in the full flow fields, including the free-stream velocity. The parameters are set to provide good agreement with the experiment throughout the full plane, including the incident free stream velocity.

Results from the MD simulation are compared with experiment in fig. 5.6 for the volume fraction, horizontal velocity component, and temperature. The agreement is quite good with a root mean square difference between experiment and simulation of less than 2% for the volume fraction and velocity fields and 10% for the temperature field.

The simple geometry and steady state behavior of the experiment provided a good system for testing the inelastic continuum equations. We compare a two-dimensional simulation of the Jenkins and Richmann equations to the experiment and MD simulations.

The continuum equations were numerically solved by a second-order accurate, finite difference method. The only fit parameter in the equations was the coefficient of restitution, which was set to the same value of  $e_0 = 0.97$  used in the MD simulation. Boundary conditions at the inlet were determined by

the experiment and at the outlet were free. Slip velocity boundary conditions were used along the wedge boundary. The heat flux at the wedge was taken to be proportional to the local  $\nu$  and  $T^{3/2}$  [64]. Euler time stepping was used to increment the simulation until the flow reached a steady state where the horizontally averaged mass flux was constant to 0.01%.

Both the experiment and continuum simulation showed a shock and an expansion fan, but the shape of the profiles differed and the magnitudes of the fields disagree by as much as a factor of two (fig. 5.7). We attribute the disagreement to the frictional drag of the confining side walls in the experiment.

The confining glass sidewalls in the experiment affect the flow. The average vertical velocity of the experimental free-stream is shown in fig. 5.8. The measured average acceleration inside the cell is  $8.9 \text{ m/s}^2$ , while a particle outside the cell falls with the expected downward acceleration of  $9.8 \text{ m/s}^2$ . This difference could be due to an increase in air drag because of the thin channel geometry, wall friction, or a combination of the two effects. The molecular dynamics simulation is three dimensional, including the confining walls, and allows for friction during ball-wall collisions. Unfortunately, the computational time for a full three dimensional continuum simulation was prohibitive for this work and a two-dimensional model for frictional drag does not exist for these flows.

We can evaluate, indirectly, the capability of the continuum model. We compare the continuum simulation to the molecular dynamics with  $\mu = 0$  for ball-wall collisions. The two simulations agree to within 1% in the bulk

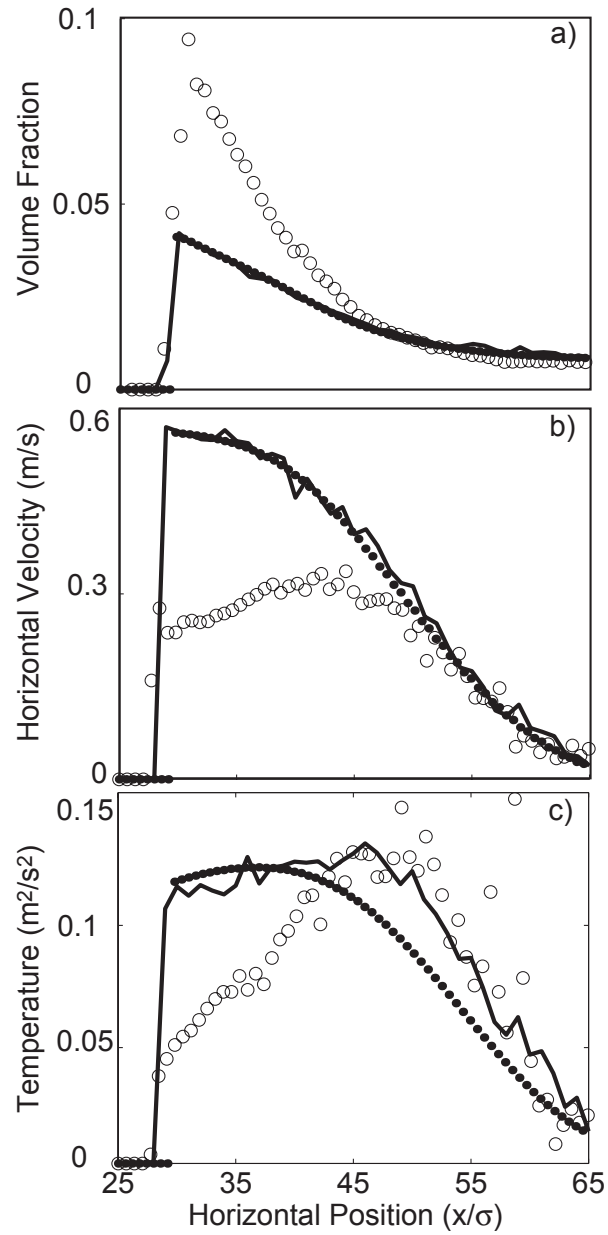


Figure 5.7: Comparison of shock profiles for granular flow past a wedge obtained from molecular dynamics (solid lines) and inelastic continuum equations (dotted line), assuming no friction. (a) Volume fraction, (b) horizontal velocity profile, and (c) temperature along the dashed line in fig. 5.4(a). Experimental measurements (open circles) show similar qualitative behavior but disagree quantitatively. The difference between the simulations and the experiment is due to wall friction [101].

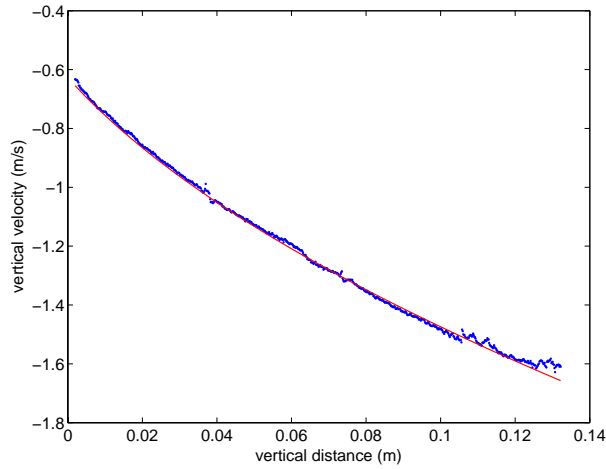


Figure 5.8: Experimentally measured free stream vertical velocity versus vertical distance (blue dots). The top of the cell corresponds to  $y=0$ . The solid red line is a fit to the experimental data yielding a downward acceleration of  $8.9 \text{ m/s}^2$ .

flow. Near the tip of the wedge, the simulations disagreed with a maximum error of 10%. The larger errors indicate a problem with the simple boundary conditions used in this study. However, the excellent agreement in the bulk confirms the applicability of the continuum equations and validates the kinetic theory approach.

## 5.4 Friction

The inelastic continuum equations agree qualitatively with experiment, but they fail to agree quantitatively due to the lack of friction in the model equations. The inclusion of friction in the continuum equations takes an already difficult problem and complicates it further requiring three additional

coupled partial differential equations for the exchange of angular momentum. Researchers have suggested that more simple modifications to the continuum model such as a tangential coefficient of restitution or viscous boundary conditions may be sufficient to bring the continuum description in quantitative accord with experiment. In the experiment, there are three sources of friction: air drag on the particles, friction between particles and the boundaries, and friction between the particles. In this section, we use the experiment and MD simulations to discern the effect of each type of friction on the shock profiles.

#### 5.4.1 Air Friction

The air drag on a 1.2 mm sphere falling in an infinite volume is negligible. In the experiment, the particles fall with speeds in the range of 0.6–3 m/s. For these velocities the corresponding Reynolds numbers  $Re = 50 - 250$  imply the air drag on the particles is proportional to the velocity squared. We find that the drag force is in the range of 0.1–2.6  $\mu\text{N}$ , less than 3% the force of gravity on the particles.

The drag force, however, is unknown for particles confined in a narrow channel. In order to eliminate air resistance, we evacuated the experimental cell to 4 Pa. The distribution of downward accelerations for particles falling between glass plates separated by  $1.1\sigma$  is shown in Fig. 5.9. There was no statistical difference between particles falling through air at atmospheric pressure and those falling through air at 4 Pa; particles fell in air with a mean downward acceleration  $a_y = 9.2 \pm 0.93 \text{ m/s}^2$ , and in vacuum with  $a_y = 9.02 \pm .96 \text{ m/s}^2$ .

### 5.4.2 Wall Friction

In the experiments reported in this chapter, the width of the Hele-Shaw cell was  $1.6\sigma$ . At this width particle-particle collisions can be significantly off axis, scattering particles into the walls. The distribution of individual particle tracks reveals a wide range of accelerations felt by the particles (Fig. 5.9). Narrowing the gap thickness to  $1.1\sigma$  reduces the possibility of off axis collisions, increasing the mean of the distribution of accelerations. The mean downward acceleration for a  $1.1\sigma$  gap thickness was  $9.2 \pm 0.93 \text{ m/s}^2$  – much greater than for a gap of  $1.6\sigma$  where  $a_y = 7.1 \pm 0.75 \text{ m/s}^2$ . This effect does decrease in the free stream as particles expand and the collision frequency decreases. However, behind the shock the collision frequency increases, presumably increasing the effect of the wall friction. Future experiments will be performed with a gap thickness of  $1.1\sigma$ .

### 5.4.3 Inter-Particle Friction

Results from our study of granular flow past a wedge were dominated by the effect of wall friction. Researchers have suggested that the disagreement between the continuum solution and the experiment may be resolved with inclusion of a viscous boundary condition [46]. However, recent experiments have shown inter-particle friction also plays a vital role in granular flows [82]. To elucidate the effect of inter-particle friction, we performed MD simulations without wall friction and gravity, varying only the particle properties. As expected, an elastic frictionless gas shows a straight shock formed at the wedge



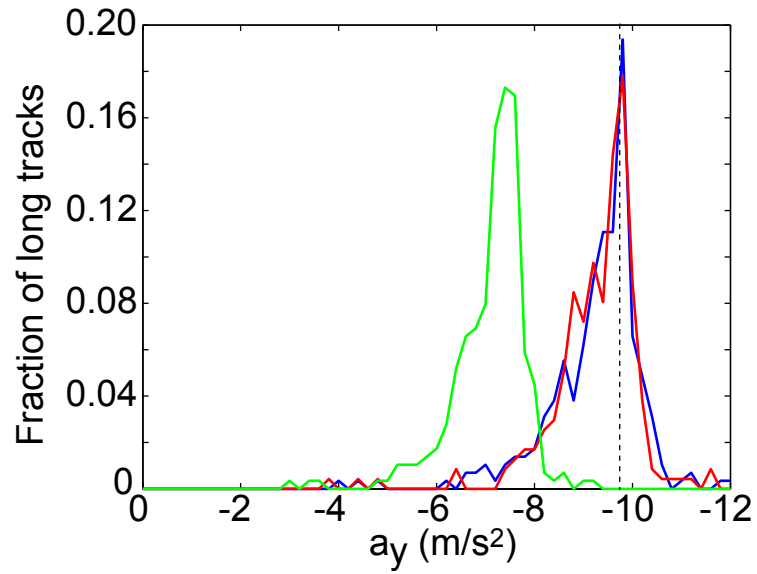


Figure 5.9: Distribution of the measured downward accelerations for particles in the experiment with gap thickness  $1.6\sigma$  and atmospheric pressure (green), gap thickness  $1.1\sigma$  atmospheric pressure (red) and  $1.1\sigma$  at 4 Pa (blue). The accelerations were determined by fitting tracks from particles in the top portion of the cell. Only particles with smooth (collisionless) tracks over a vertical distance  $30\sigma$  were considered.

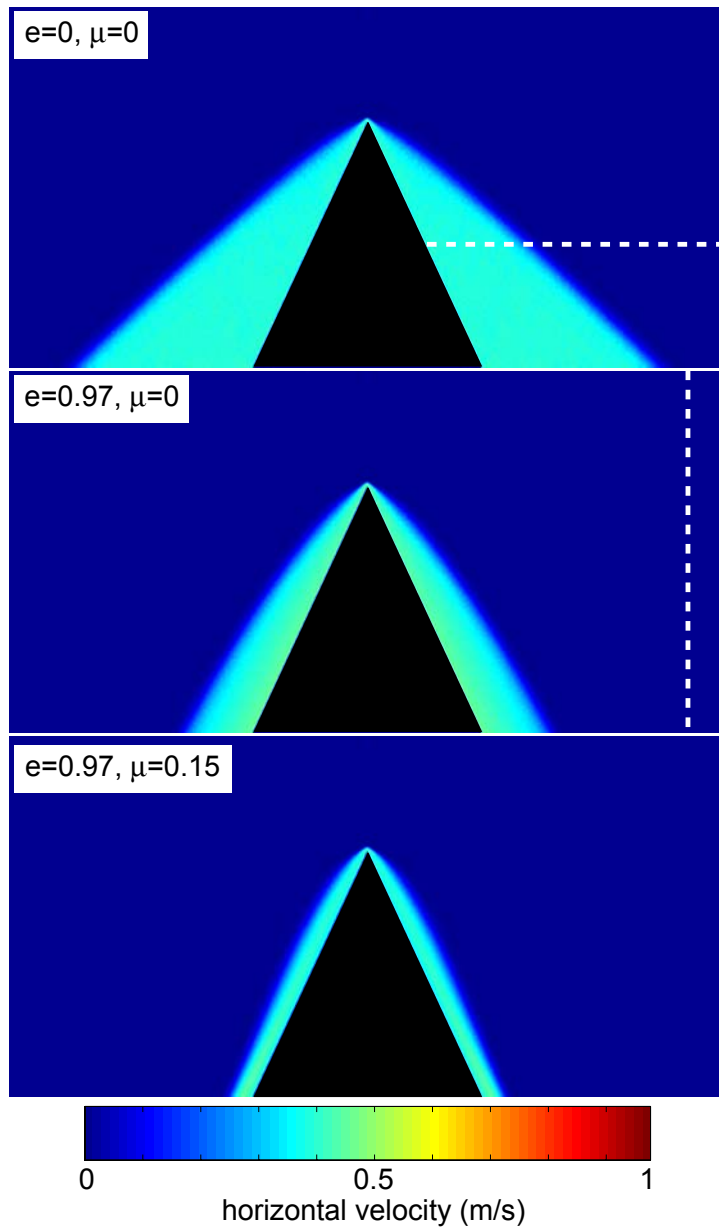


Figure 5.10: MD simulations showing the dependence of the shock shape on inelasticity and friction. For elastic particles, the shock extends straight into the fluid at a constant angle with constant parameters behind the shock. Adding inelasticity and friction causes the shock to curve in towards the wedge. The dashed lines show the location of the comparisons in Fig. 5.11.

tip (Fig. 5.10). The shock profiles for  $\nu$ ,  $T$ , and Mach number are shown in Fig 5.11. For an elastic frictionless gas (blue line), the shock is sharp and the flow parameters behind the shock are constant. For an inelastic frictionless gas, the shock curves closer to the wedge. Behind the shock the increased temperature due to shock compression is rapidly dissipated and the volume fraction continues to increase (blue line). With the addition of inter-particle friction, the region behind the shock narrows, the maximum temperature in the shock decreases and the dissipation rate increases (green line).

## 5.5 Conclusion

Our experiments on granular flow past a wedge reveal shocks that are analogous to those in gas dynamics. We find that both molecular dynamics and continuum equations predict the quantitative behavior of a supersonic, frictionless granular flow past an obstacle in the regime of low dissipation and low volume fraction. The disagreement between experiment and continuum modeling is a consequence of the confining sidewalls. While a thin cell geometry is useful in experiment because it facilitates imaging, most real applications will be fully three dimensional with negligible wall interactions. However, further MD simulations of the flow geometry without gravity and wall friction show that inter-particle friction may still complicate direct comparison between frictionless continuum theory and physical granular flows.

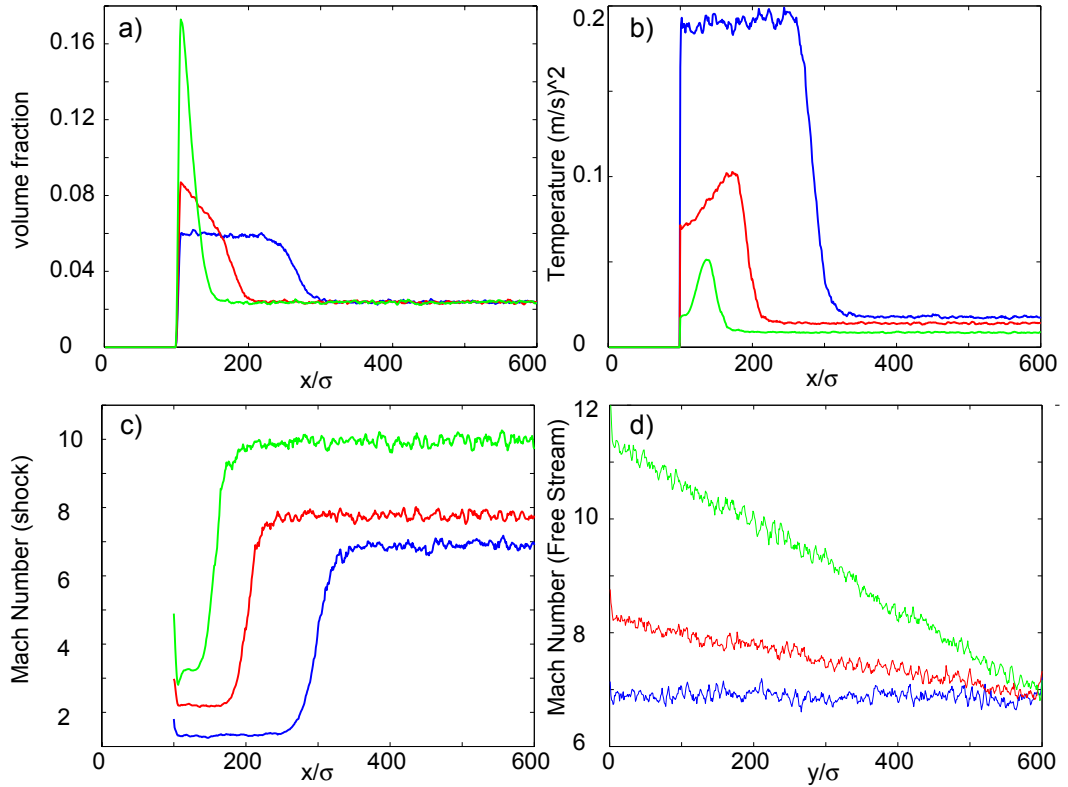


Figure 5.11: Shock profiles taken from MD simulation results of particles moving through a thin cell with no gravity and interacting with a wedge. We compare the volume fraction **a**, temperature **b**, Mach number **c** profiles along the horizontal dashed line in Fig. 5.10 for elastic, frictionless particles  $e_0 = 1, \mu = 0$  (blue line), inelastic, frictionless particles  $e_0 = 0.97, \mu = 0$  (red line), and inelastic frictional particles  $e_0 = 0.97, \mu = 0.15$  (green line). The flow values behind the shock for elastic frictionless particles are constant. Inelastic collisions cause the flow parameters to evolve behind the shock – as the temperature is dissipated, the volume fraction increases and the Mach number increases. Adding friction increases the dissipation of energy and exacerbates the effects. In **d** we plot the Mach Number of the free stream flow taken along the vertical dashed line in Fig. 5.10. Adding inelasticity and friction to the particles causes the temperature in the free stream to be dissipated, increasing the Mach number.

## Chapter 6

# Normal Shock Propagation in a Funnel

### 6.1 Abstract

We study the propagation of a normal shock wave formed at the intersection of two oblique shocks. We compare results from MD simulations to a Hugoniot-Rankine type approximation of the inelastic continuum equations. The MD simulations show behavior similar to the simplified equations, but inelastic collisions cause evolution of the shock unaccounted for in the approximation. We find the shock speed as a function of inelasticity and compare results to an asymptotic solution of a set of inelastic continuum equations.

### 6.2 Introduction

In the previous chapter we described an oblique shock formed as a granular flow interacts with a wedge. In this chapter we examine a flow that travels through a funnel defined by two wedges. This geometry is often found at the end of a wind tunnel [5]. As before, the free stream flow is incident downwards on the wedges (Fig. 6.1). At each wedge tip, an oblique shock wave forms. At the shock the streamlines are deflected through an angle  $\theta$  to flow parallel to the wedge surfaces. Near the opening of the funnel, the shocks

interact. In the interaction region the streamlines are again deflected by  $\theta$  and flow out of the funnel. For sufficiently strong shocks, the second deflection can not be achieved through an oblique shock front, instead a normal shock forms at the intersection region [5]. Behind the normal shock, the flow streamlines return to the original orientation.

We observe the identical phenomena in our experiments (Fig. 6.1C) and MD simulations (Fig. 6.2). As in the previous chapter, a granular flow fell under gravity past two 30 degree wedges. Two identical oblique shocks form at each wedge tip and interact near the opening. A normal shock forms in the interaction region. Behind the shock the flow is denser, hotter and slower.

An oft studied problem in supersonic fluid mechanics is the shock tube where a piston moves with supersonic velocity into an initially undisturbed gas. The motion of the piston creates a normal shock that propagates into the undisturbed region. This geometry is difficult to achieve for granular flows, however we exploit the normal shock formed in the funnel described above in order to study this problem. If we reduce the distance between the bottom of the wedges such that the incoming mass flux into the funnel is greater than the flow rate into the channel, the normal shock will propagate upstream, similar to the shock propagating in a tube.

In the MD simulations, particles are injected into the Hele-Shaw cell with an initial mean vertical velocity  $u = -5.8\sqrt{g\sigma}$  and temperature  $T = 0.024 g\sigma$ . The particles accelerate under gravity into a funnel composed of two 30° wedges (Fig. 6.2). The bottom corners of the wedges are separated

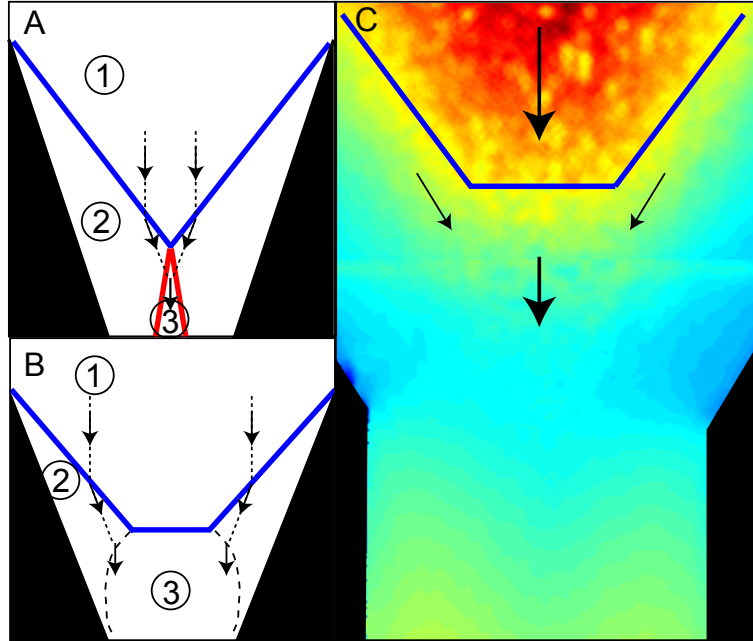


Figure 6.1: Schematic of oblique shocks (blue lines) interacting in a region between two wedges. The dashed lines with arrows indicate the direction of the flow streamlines. The initial flow is incident downwards. Behind the shocks the flow is deflected through an angle  $\theta$  and the Mach number of the flow decreases. The flow is deflected again by  $\theta$  in the region of shock interaction. The maximum allowed deflection angle by an oblique shock depends on the Mach number in the incident region (see Chapter 5.2, Fig. 5.2). If the Mach number in region 2 is large, then  $\theta < \theta_{max}$ , the incident shock waves are refracted at the interaction region (**A**). If the Mach number is small such that  $\theta$  is greater than  $\theta_{max}$ , a normal shock forms at the interface of the interaction region (**B**). The vertical velocity field from an experimental granular flow through a funnel formed by two wedges is shown in (**C**). The bottom of the wedges were separated by  $25\sigma$ . A normal shock forms at the interaction region. The flow behind the normal shock is hotter, denser, and slower than the incident flow.

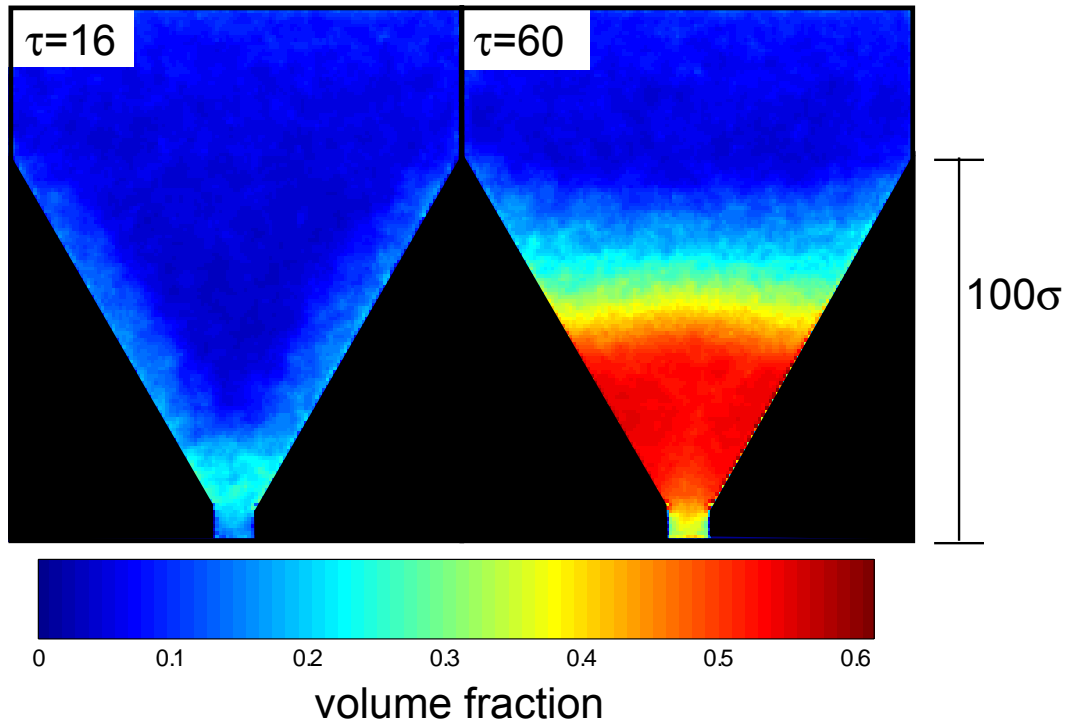


Figure 6.2: Volume fraction fields from an MD simulation of granular flow in a funnel for  $e_0 = 0.9$ . The average fields were calculated using the tessellation technique described in Methods.



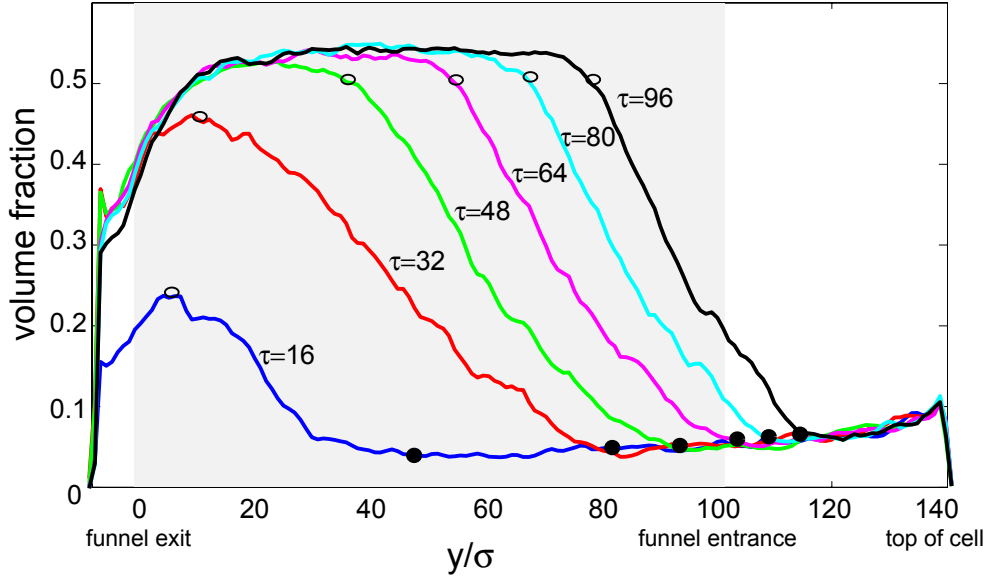


Figure 6.3: MD simulation results ( $e_0 = 0.97$ ) for the propagation of the volume fraction wave up the funnel. Each profile is the mean volume fraction at time along the center between the two wedges. (Time  $\tau$  is measured in units of  $\sqrt{\sigma/g}$ .) Dark dots indicate the location of the shock and open circles indicate the front of the crystalline region. The shaded region is the realm inside the funnel.

by  $12\sigma$ . Within a time  $\tau = 16\sqrt{\sigma/g}$ , we observe an oblique shock at each wedge tip and a normal shock near the funnel exit. The mass flow rate into the interaction region is greater than the flow rate exiting into the vertical channel, causing the normal shock to propagate upwards.

### 6.3 Normal shock propagation

Volume fraction profiles through the center of the funnel are shown in Fig. 6.3. A dilute granular flow ( $\nu_0 = 0.09$ ) enters into the Hele-Shaw chamber at  $y = 140\sigma$  and expands due to gravity. Near the exit of the funnel at  $y = 0$  a normal shock forms. The strength of the shock increases as it propagates upstream from  $\tau = 0 - 30 \sqrt{\sigma/g}$  until the volume fraction behind the shock reaches the maximum allowed value (0.5496 corresponds to a single layer of hexagonally packed spheres confined in a cell with gap thickness  $1.1\sigma$ ). For  $\tau > 40 \sqrt{\sigma/g}$  the shape of the volume fraction profile remains constant as it propagates. At  $\tau = 60 \sqrt{\sigma/g}$  the shock approaches the opening of the funnel.

The front edge of the shock occurs where the volume fraction changes from expanding under gravity to increasing because of shock compression. To find the shock location, we subtract the free stream evolution of  $\nu$  from the volume fraction profiles. We define the leading edge of the shock as where the adjusted volume fraction profiles  $\delta\nu$  increase above 0.05 (solid black dots shown in Fig. 6.3). The dense, crystalline region begins where the profile reaches the maximum volume fraction (open circles shown in Fig. 6.3).

The shock front location versus time is plotted in Fig. 6.4. For small times,  $\tau < 20 \sqrt{\sigma/g}$ , the shock is developing and propagates quickly. Once the maximum volume fraction behind the shock is reached, the shock velocity decreases and the profile propagates without change. The solid line is a linear fit to the shock locations for  $\tau = 30 - 60 \sqrt{\sigma/g}$ . Shock locations after  $60 \sqrt{\sigma/g}$  were excluded because the shock front moved beyond the funnel. For  $e = 0.9$

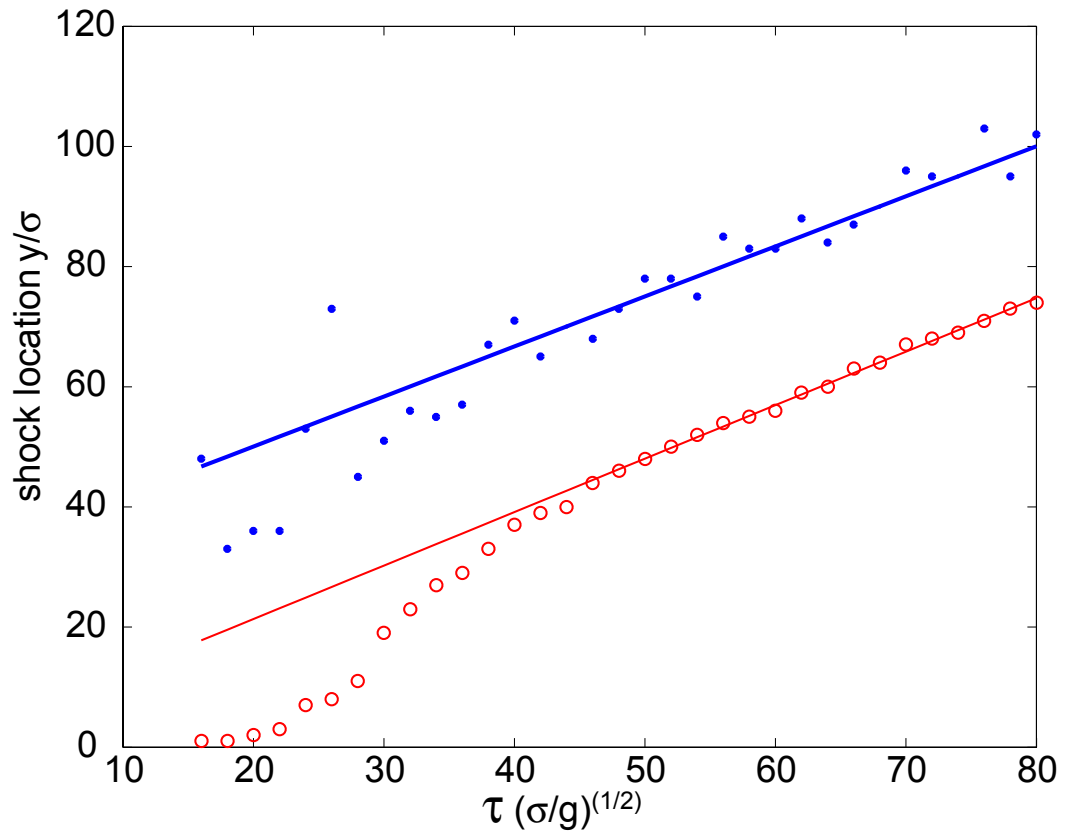


Figure 6.4: (MD simulation,  $e_0 = 0.9$ ) The location of the shock as a function of time as the normal shock propagates upwards in the funnel (blue dots). The solid blue line is a fit to the linear, constant profile region. The slope of the line indicates the velocity of the shock. The red open circles indicate the front location of the crystalline region behind the shock and the red line is a fit to the linear, constant region. The growth rate of the crystalline region is equal to the shock velocity within our fitting accuracy

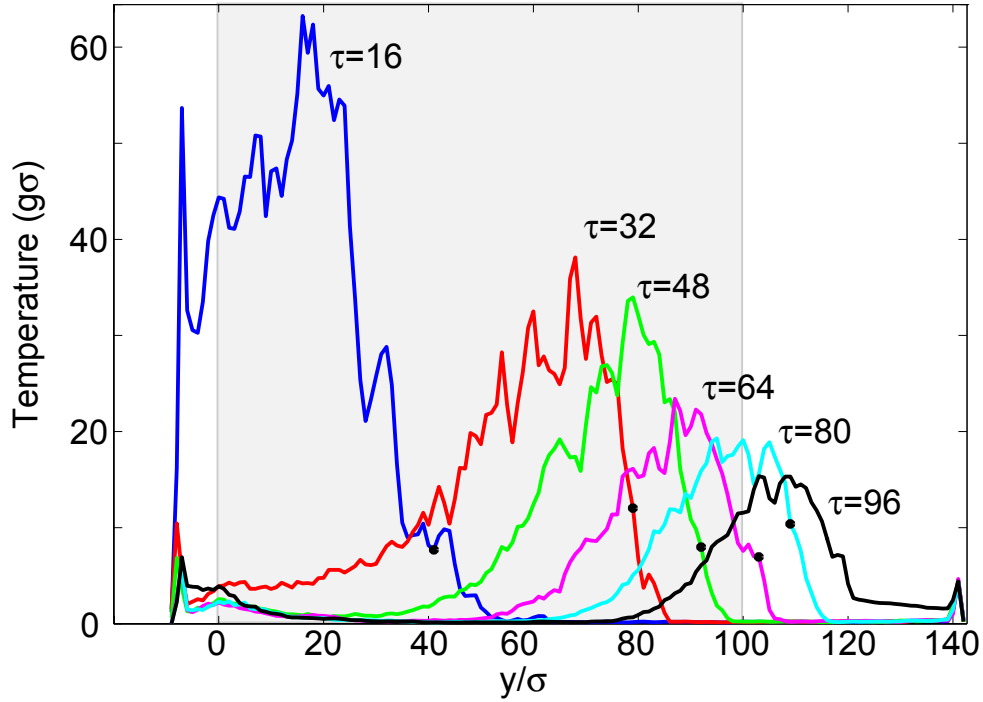


Figure 6.5: MD simulation results for the propagation of the temperature wave up the funnel. Dark dots indicate the location of the shock. The shaded region is the realm inside the funnel.

and opening width  $12\sigma$  the asymptotic shock velocity equals  $0.83 \sqrt{g\sigma}$ . The front edge of the crystalline region travels with a velocity  $0.89 \sqrt{g\sigma}$ .

At the leading edge of the shock wave, the temperature of the flow increases dramatically by more than 2 orders of magnitude (Fig. 6.5). As the temperature and density increase, so does the collision frequency. The greater numbers of inelastic collisions rapidly reduce the temperature, such that once the maximum volume fraction is reached behind the shock, the temperature has cooled to less than the free stream value. At the exit of the funnel, the temperature again increases as the particles streaming velocity increases. As

the shock wave propagates upstream, the maximum value of the temperature decreases.

## 6.4 Hugoniot-Rankine Approximation

The full equations of motion for a compressible gas flow are complicated and difficult to solve. For several problems of interest in elastic flows, the flow is constant both before and after the shock, changing only at the shock wave. For these systems, a series of approximations greatly simplify the equations. What was once five coupled partial differential equations requiring a computer to solve is reduced to one-dimensional jump conditions, the Hugoniot-Rankine equations, only needing algebra to find the solution [5, 71].

For instance consider the one-dimensional problem of a piston moving with constant, supersonic velocity  $u_p$  into a gas. Far from the piston, the gas is undisturbed with an initial density  $\rho_1$ , velocity  $u_1$  and pressure  $P_1$ . Near the piston, no slip boundary conditions require the gas to move with the piston velocity,  $u_2 = u_p$ . A normal shock separates regions 1 and 2 (Fig. 6.6). If we assume the gas to be inviscid and non-conducting with no body forces, and assume the flow has reached the asymptotic steady state where the shock propagates without change, then the compressible Navier-Stokes equations reduce to the Hugoniot-Rankine jump conditions [5, 71]. The conservation of mass requires the mass flux to be constant:

$$\rho_1 u_1 = \rho_2 u_2 = j. \tag{6.1}$$

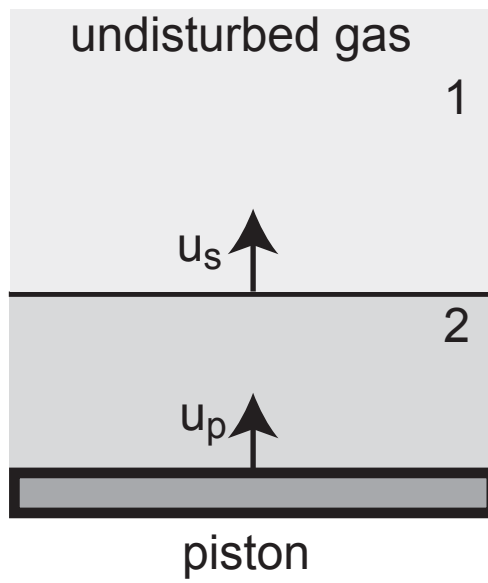


Figure 6.6: schematic. The piston moves into the gas with a constant supersonic velocity  $u_p$ . A normal shock separates the undisturbed region 1 from the compressed region 2. The shock propagates into the undisturbed region with a velocity  $u_s$ .

Applying conservation of momentum yields

$$P_1 + \rho_1 u_1^2 = P_2 + \rho_2 u_2^2. \quad (6.2)$$

We use the above Hugoniot-Rankine equations to estimate the changes across the normal shock propagating in the funnel. Because the fluid is inelastic, the volume fraction behind the shock will approach the maximum allowed value. The final velocity behind the shock can be estimated from Eq. 6.1,  $u_2 = (\nu_1 u_1) / \nu_{max}$ . The vertical velocity profile for the normal shock at  $56 \sqrt{\sigma/g}$  is shown in Fig. 6.7a. The velocity in the free stream is accelerated by gravity (red line). Behind the shock the velocity initially decreases. Near the exit of the funnel, the velocity is again accelerated by gravity. The jump conditions accurately predict the initial value behind the shock (redline).

For a strong shock,  $P_2$  is much greater than  $P_1$ . From Eq. 6.2, the pressure change is approximately  $P_2 = j(u_2 - u_1)$ . Using the velocity difference determined above we find an approximation for the final pressure behind the shock. The pressure profile for the normal shock wave at  $56 \sqrt{\sigma/g}$  is shown in Fig. 6.7b. In the free stream the pressure is negligible. Behind the shock the pressure dramatically rises as both the temperature and volume fraction increase. The prediction for the Hugoniot relation is far removed from the measured pressures.

The inability of the jump conditions to capture the full features of the granular flow is unsurprising. In a simple, elastic gas, the flow change due to compression by a piston depends on the incoming flow parameters and the

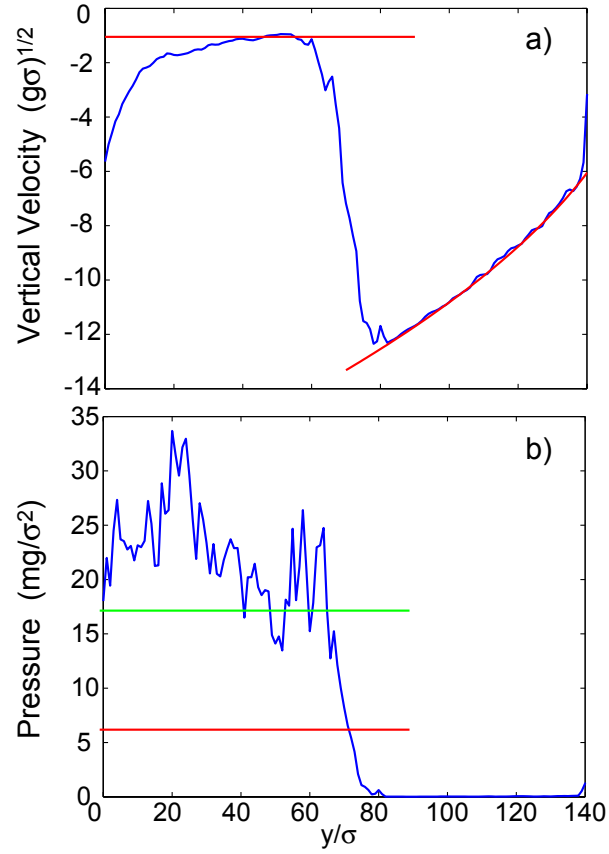


Figure 6.7: The vertical velocity **(a)** and pressure profiles **(b)** taken through the center of the funnel ( $e_0 = 0.9$ ,  $\tau = 56\sqrt{g\sigma}$ ). In the free stream the vertical velocity changes due to gravity. Behind the shock, the flow reaches a constant velocity and the pressure increases. The solid red line indicates the values predicted by the jump conditions and the solid green line indicates the asymptotic pressure predicted by the analytic solution.



velocity of the piston. For a granular gas, the final state is independent of the initial conditions. Inelasticity provides a temperature sink, continuously cooling the gas. The flow behind the shock will cool until the temperature is zero and density has reached the maximum allowed value, independent of the initial conditions or piston velocity. Since the number of particles is conserved in a granular gas, Eq. 6.1 holds and the approximation accurately predicts the velocity of the flow once the maximum volume fraction has been reached. The energy of the flow is not conserved, hence Eq. 6.2 does not hold since the pressure of the flow also depends on temperature.

The temperature in the solid region should decay to zero, however the MD simulation is not designed for solids with zero  $T$ . In the simulation, if two particles collide twice within  $3 \times 10^{-4} \sqrt{g/\sigma}$ , the coefficient of restitution for the second collision is set to 1, preventing further decay of  $T$  in that collision. While the prevented energy loss is small, it may contribute to the disagreement in the pressure term. The temperature in the crystalline region is small compared with the free stream, but is prevented from reaching zero.

## 6.5 Analytical Solution of a set of Inelastic Continuum Equations

Goldshtein *et al.* theoretically examined how inelasticity affected the shock formed by a piston moving into an initially undisturbed granular gas [48, 67]. The resulting flow, similar to our MD study, may be divided into three sections: the undisturbed region, the shock region, and cold, crystalline region

adjacent to the piston. The thickness of the crystalline region increases with time as

$$(u_s - u_p) t \quad (6.3)$$

[46].

In the asymptotic time limit, the researchers found analytic expressions for the shock front velocity and final pressure behind the shock.

$$u_s = \frac{u_p}{1 - \nu_0/\nu_{max}} \quad (6.4)$$

$$P_s = \frac{\rho_o u_p^2}{1 - \nu_0/\nu_{max}}. \quad (6.5)$$

The limiting values of the shock velocity and the shock pressure are surprisingly independent of  $e_0$ , varying only due to the initial density.

We examined the dependence of the normal shock speed as a function of inelasticity. The shock location versus time for 4 different values of  $e_0$  is shown in Fig. 6.8. For smaller values of restitution the shock travels less distance, however the asymptotic shock value  $u_s$  does not depend on  $e_0$  within our fitting error.

To compare with Eq. 6.4 and 6.5, we define  $u_p$  according to Eq. 6.3. Our results show that shock front moves at approximately the same speed as the crystalline region. This is consistent with Eq. 6.4 since  $\nu_0 \ll \nu_{max}$ . The predicted asymptotic pressure behind the shock agrees surprisingly well with the measured value (Fig. 6.7 (greenline)).

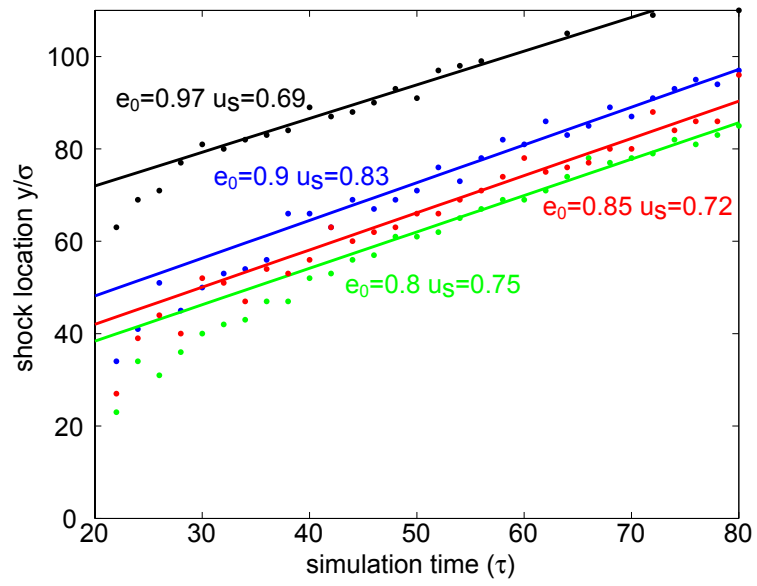


Figure 6.8: The shock location versus time for 4 values of  $e_0$ . The shock front travels fastest while it is developing and eventually settles to an asymptotic value. The solid lines are a fit to the asymptotic region. The final velocity  $u_s$  does not vary systematically with  $e_0$ .

## 6.6 Discussion

The normal shock in the funnel reached an asymptotic steady state where the volume fraction profile propagates without change. In this limit it is possible to apply approximations to the inelastic continuum equations with some success. However, a steady state shock profile is not typical of granular flows. For instance, in the frequently studied vibrated system, a normal shock is created by a piston moving with a time-dependent velocity. The shock continuously changes as it propagates into a fluid with strong spatial gradients [14], see Chapter 2.3. Even when the forcing and flow is steady, such is in gravity driven granular flow past a wedge, the flow behind the oblique shock wave evolves. The presence of gravity causes spatial gradients in the velocity behind the shock. In these cases an approximate or asymptotic solution to the inelastic continuum equations is insufficient; instead the full, compressible and time dependent equations must be solved.

For an elastic fluid, the changes across the shock depend on the upstream flow parameters. The values of  $T$ ,  $\nu$ , and  $P$  in the region behind the shock will change depending on the values in front of the shock. In a granular flow the asymptotic values behind the shock are fixed. The shock will continue to change until  $T$  approaches zero and  $\nu$  reaches  $\nu_{max}$ . Unlike in an elastic gas where the shock is controlled by pressures at the boundaries, a shock in an inelastic fluid is controlled by energy dissipation rate and the maximum allowed volume fraction.

## Chapter 7

### Conclusions and Suggestions for Future Work

We began this work asking whether continuum, hydrodynamic ideas apply to granular flows. Despite the macroscopic size of the particles, lack of spatial and time scale separation, and an energy sink due to inelastic collisions, we found the continuum theories to be in qualitative accord with experiment and MD simulation in each of the three geometries studied. We found quantitative agreement when the continuum theory predictions were independent of the particle properties, as in the shallow water approximation applied to the cylinder wake flow and in the asymptotic behavior of a normal shock propagating in a granular funnel. The inelastic continuum equations captured the qualitative features of experimental measurements from the granular flow past a wedge, but quantitative agreement suffered because frictional interactions between particles and between particles and boundaries were not taken into account in the derivation of the equations. In this chapter I briefly summarize the results of each study and suggest further experiments.

## 7.1 Wake Behind a Cylinder

We found the v-shaped wake behind a cylinder moving through a vibrated granular layer to be well described by a shallow water theory for a surface-tensionless fluid for layer depths studied from  $h = 1\sigma$  to  $6\sigma$ . The shallow water approximation has been assumed in theoretical treatments of granular avalanches and vibrated layers [51], but our measurements provide the first detailed, experimental verification of the applicability of the shallow water equations to granular fluids.

Researchers have suggested that for deeper layers the energy generated when the layer collides with the bottom plate may not travel to the top of the layer [46]. Our studies were restricted to small layer depths by limitations of the experimental apparatus. For deeper layers, the container level was unstable. Replacing the 5 cm<sup>2</sup> air bearing with a larger, 10 cm<sup>2</sup> bearing should make it easier to keep the surface of the layer level allowing future experiments to study deeper layers.

Hugoniot style jump conditions from shallow water theory predict the change in height across a shock on the surface of a fluid. Further measurements of the height profile directly in front of the rod may be compared to these predictions, further testing the applicability of the shallow water theory.

Within the v-shaped wake, we observe an additional diamond like structure that is not captured by the shallow water theory. The wavelength of the diamond pattern scales with the rod velocity and frequency of the shaking, sug-

gesting the pattern is related to the external forcing. How the shaking leads to the diamond structure is not understood. Time resolved height measurements of the wake may explain the diamond formation.

## 7.2 Granular flow past a wedge

We verified that a granular flow falling between two glass plates is supersonic with a mean Mach number greater than 10. While it is often mentioned that granular flows are supersonic, this remains the only measurement of the Mach number in the bulk of an experimental granular fluid. An oblique shock formed at a wedge inserted into the flow. Quantitative comparison between the experiment and a numerical solution of the inelastic continuum equations was hampered by the influence of the side walls in the experiment. However, agreement between the continuum theory and MD simulations without wall friction confirmed the applicability of the hydrodynamics description and highlights the need for frictional effects to be incorporated into the equations.

### 7.2.1 gap thickness

We found that narrowing the plate separation in the experiment reduced the effect of the confining sidewalls. The number of particles falling in the free stream with an acceleration of  $9.8 \text{ (m/s}^2\text{)}$  increased when the gap thickness was decreased from  $1.6\sigma$  to  $1.1\sigma$ . It is not clear how the narrowed gap affects the hotter, denser flow behind the shock. Future experiments should

determine the affect of gap width on the profiles behind the shock.

### **7.2.2 boundary conditions**

Determining the appropriate boundary conditions for granular fluids remains an active and difficult area of research [43, 61, 64, 111]. For our numerical solution of granular flow past the wedge, we empirically determined the heat flux condition at the wedge by measuring the effect in MD simulations. A similar method was employed by Bougieet *al.* [14]. The boundary conditions for a granular fluid are not necessarily similar to the conditions employed in elastic gas flows. In fluid mechanics, the derivation of the boundary conditions assumes the fluid never leaves the boundary, but this does not hold true for granular flows [111]. More experimental measurements on the interactions of granular flows with surfaces are needed.

### **7.2.3 higher dissipation**

The inelastic continuum equations were derived in the limit of small dissipation. Our flow consisted of stainless steel particles with a high coefficient of restitution in order to agree with this assumption. Future experiments should determine how decreasing the coefficient of restitution affects the shock profiles and the agreement with the equations.



### **7.3 Normal shock propagation in a funnel**

Our initial study of a normal shock propagating in a funnel revealed a favorable comparison between MD simulations and an asymptotic solution to a hydrodynamic theory. However, the MD simulation is not designed to model the cold, crystalline flows which formed behind the shock. The most immediate next step is to perform an experiment in the granular funnel geometry and compare results to the hydrodynamic solution. This work is already in progress.

### **7.4 velocity distributions**

The Hugoniot-Rankine relations and the Navier-Stokes equations accurately predict the changes across a normal shock in a fluid of elastic particles. However, the structure of the shock profile and the single particle velocity distribution function within the shock remain unknown [93]. In an elastic gas the shock is too thin and the molecules are too small for standard experimental techniques, making a direct measurement of the distribution function extremely difficult. A direct measurement of the distribution function is possible in a granular fluid. Preliminary analysis of data from experiment and MD simulations suggest the distribution function within the shock is neither Gaussian nor bimodal. Further experiments should yield a functional form of the distribution function and aid the understanding of kinetics in shocks.

## 7.5 Conclusions

Our work on shocks demonstrates that hydrodynamic theories can capture granular phenomena. At some point, the description must fail since it should not apply to quasi static flows where the particles remain in contact. More experiments amenable to direct comparison to theory are needed to further establish the equations, determine better boundary conditions for the equations, and determine the limits of their applicability.

## Appendix

# Appendix 1

## Shallow Water Equations

The hydraulic approximation for fluids assumes the flow is isentropic, inviscid, and incompressible. Applying these assumptions to the inelastic continuum equations derived by Jenkins and Richman, we begin with

$$\nabla \cdot \mathbf{u} = 0 \tag{1.1}$$

$$\rho \frac{\partial \mathbf{u}}{\partial t} + \rho \mathbf{u} \cdot \nabla \mathbf{u} = -\nabla \cdot \underline{\mathbf{P}} - g \hat{\mathbf{z}} \tag{1.2}$$

Additionally, we assume that the flow is irrotational:

$$\nabla \times \mathbf{u} = 0. \tag{1.3}$$

The above equations are identical to those for a fluid in this limit. Following the method laid out by Stoker, we recover the shallow water equation for a fluid [116]:

Let the free surface be described by  $z = \eta(x, y, t)$ . The boundary condition at the top surface,  $z = \eta$  is then:

$$w = \frac{\partial \eta}{\partial t} + u \cdot \frac{\partial \eta}{\partial x} + v \cdot \frac{\partial \eta}{\partial y} \Big|_{z=\eta}, \tag{1.4}$$

and

$$P = 0 \Big|_{z=\eta}. \tag{1.5}$$

For a traditional fluid, the fluid remains in contact with the bottom boundary at  $z = -h$ . At the bottom, the boundary condition is

$$\left( u \frac{\partial h}{\partial x} + v \frac{\partial h}{\partial y} + w \right) |_{z=-h} = 0 \quad (1.6)$$

The shallow water limit requires the changes in the direction perpendicular to the surface ( $\hat{\mathbf{z}}$ ) be much smaller than the changes parallel to the surface ( $\hat{\mathbf{x}}, \hat{\mathbf{y}}$ ). To make the coming expansion evident, we non-dimensionalize the flow in terms of two lengths  $d$  and  $k$ , where  $d$  represents a typical depth and  $k$  a typical length in the horizontal direction. The system is shallow if  $\sigma = d^2/k^2$  is small. In non-dimensional units the independent variables are:

$$\bar{x} = x/k, \bar{y} = y/k, \bar{z} = z/d, \tau = t\sqrt{gd}/k, \quad (1.7)$$

and the dependent variables are:

$$\bar{u} = \frac{u}{\sqrt{gd}}, \bar{v} = \frac{v}{\sqrt{gd}}, \bar{w} = w \frac{d}{k\sqrt{gd}}, \bar{P} = \frac{P}{\rho gd}, \bar{\eta} = \eta/d, \bar{h} = h/d. \quad (1.8)$$

Writing equations A.1 through A.6 in terms of the non-dimensional variables and dropping the bars yields the incompressibility condition:

$$\sigma \frac{\partial u}{\partial x} + \sigma \frac{\partial v}{\partial y} + \frac{\partial w}{\partial z} = 0, \quad (1.9)$$

the momentum flux condition:

$$\sigma \left[ \frac{\partial u}{\partial t} + u \frac{\partial u}{\partial x} + v \frac{\partial u}{\partial y} \right] + w \frac{\partial u}{\partial z} = -\sigma \frac{\partial P}{\partial x}, \quad (1.10)$$

$$\sigma \left[ \frac{\partial v}{\partial t} + u \frac{\partial v}{\partial x} + v \frac{\partial v}{\partial y} \right] + w \frac{\partial v}{\partial z} = -\sigma \frac{\partial P}{\partial y}, \quad (1.11)$$

$$\sigma \left[ \frac{\partial w}{\partial t} + u \frac{\partial w}{\partial x} + v \frac{\partial w}{\partial y} \right] + w \frac{\partial w}{\partial z} = -\sigma \left( \frac{\partial P}{\partial z} + 1 \right), \quad (1.12)$$

and for irrotational flow:

$$\frac{\partial w}{\partial y} = \frac{\partial v}{\partial z}, \quad \frac{\partial u}{\partial z} = \frac{\partial w}{\partial x}, \quad \frac{\partial v}{\partial x} = \frac{\partial u}{\partial y}. \quad (1.13)$$

The surface boundary condition at  $z = \eta$  becomes

$$\sigma \left[ \frac{\partial \eta}{\partial t} + u \frac{\partial \eta}{\partial x} + v \frac{\partial \eta}{\partial y} \right] = w \quad (1.14)$$

and  $P = 0$ . The bottom boundary condition taken at  $z = -h$  is

$$\sigma \left[ u \frac{\partial h}{\partial x} + v \frac{\partial h}{\partial y} \right] + w = 0. \quad (1.15)$$

We then expand all dependent variables in a power series in  $\sigma$ :

$$u = u^{(0)} + \sigma u^{(1)} + \dots \quad (1.16)$$

$$v = v^{(0)} + \sigma v^{(1)} + \dots \quad (1.17)$$

$$w = w^{(0)} + \sigma w^{(1)} + \dots \quad (1.18)$$

$$P = P^{(0)} + \sigma P^{(1)} + \dots \quad (1.19)$$

$$\eta = \eta^{(0)} + \sigma \eta^{(1)} + \dots \quad (1.20)$$

and insert the expansions into Eq.A.9 through A.15. Equating terms of like powers in  $\sigma$  we find to zero order the relations

$$w^{(0)} = 0, \quad (1.21)$$

$$u^{(0)} = u^{(0)}(x, y, t), \quad (1.22)$$

$$v^{(0)} = v^{(0)}(x, y, t), \quad (1.23)$$

$$P^{(0)}(x, y, z, t)|_{z=\eta_0} = 0. \quad (1.24)$$

The vertical component of the velocity is zero, and the velocities parallel to the surface are independent of the vertical coordinate to lowest order.

Collecting terms that are linear in  $\sigma$  yields the equations:

$$\frac{\partial u^{(0)}}{\partial x} + \frac{\partial v^{(0)}}{\partial y} = -\frac{\partial w^{(0)}}{\partial z} \quad (1.25)$$

$$\frac{\partial u^{(0)}}{\partial t} + u^{(0)} \frac{\partial u^{(0)}}{\partial x} + v^{(0)} \frac{\partial u^{(0)}}{\partial y} = -\frac{\partial P^{(0)}}{\partial x} \quad (1.26)$$

$$\frac{\partial v^{(0)}}{\partial t} + u^{(0)} \frac{\partial v^{(0)}}{\partial x} + v^{(0)} \frac{\partial v^{(0)}}{\partial y} = -\frac{\partial P^{(0)}}{\partial y} \quad (1.27)$$

$$\frac{\partial P^{(0)}}{\partial z} + 1 = 0 \quad (1.28)$$

$$\frac{\partial \eta^{(0)}}{\partial t} + u^{(0)} \frac{\partial \eta^{(0)}}{\partial x} + v^{(0)} \frac{\partial \eta^{(0)}}{\partial y} = w^{(1)}, \text{ at } z = \eta^{(0)} \quad (1.29)$$

$$u^{(0)} \frac{\partial h}{\partial x} + v^{(0)} \frac{\partial h}{\partial y} = w^{(1)}, \text{ at } z = -h \quad (1.30)$$

From the zero order approximation, we found  $u^{(0)}$  and  $v^{(0)}$  are independent of  $z$ , so Eq. 1.25 can be easily integrated to give:

$$w^{(1)} = -\left(\frac{\partial u^{(0)}}{\partial x} + \frac{\partial v^{(0)}}{\partial y}\right)z - \left[\frac{\partial (u^{(0)}h)}{\partial x} + \frac{\partial (v^{(0)}h)}{\partial y}\right]_{z=-h}. \quad (1.31)$$

To first order the vertical component of the velocity is linearly dependent on  $z$ . We can also integrate the pressure condition from Eq. 1.28 to get

$$P^{(0)}(x, y, z, t) = \eta^{(0)}(x, y, t) - z, \quad (1.32)$$

which is the hydrostatic pressure relation. Inserting the values for  $P^{(0)}$  and  $w^{(0)}$  into the equations and dropping the superscripts yields the shallow water

equations:

$$\frac{\partial u}{\partial t} + u \frac{\partial u}{\partial x} + v \frac{\partial u}{\partial y} + \frac{\partial \eta}{\partial x} = 0, \quad (1.33)$$

$$\frac{\partial v}{\partial t} + u \frac{\partial v}{\partial y} + v \frac{\partial v}{\partial y} + \frac{\partial \eta}{\partial y} = 0, \quad (1.34)$$

$$\frac{\partial \eta}{\partial t} + \frac{\partial u (\eta + h)}{\partial x} + \frac{\partial v (\eta + h)}{\partial z} = 0 \quad (1.35)$$

The shallow water equations are identical in form and spirit to the equations for a compressible fluid: with the layer height  $h$  and sound speed  $c = \sqrt{\frac{\partial \bar{p}}{\partial \bar{\rho}}} = \sqrt{gh}$ . In order to make the analogy clear, we assume the problem is one dimensional and that  $u, \eta$  and their derivatives are small. Keeping only linear terms from Eqs. 1.33 and 1.35 gives:

$$\frac{\partial u}{\partial t} = -\frac{\partial \eta}{\partial x} \quad (1.36)$$

$$\frac{\partial u (\eta + h)}{\partial x} = -\frac{\partial \eta}{\partial t}. \quad (1.37)$$

Eliminating  $\eta$  from the system of equations gives the wave equation for  $u$  and assuming a flat bottom,

$$\frac{\partial^2 u}{\partial x^2} - \frac{1}{h} \frac{\partial^2 u}{\partial t^2} = 0. \quad (1.38)$$

A wave propagates over the surface with a velocity  $c = \sqrt{h}$  in non-dimensional units, or in real units  $c = \sqrt{gh}$ .



## Bibliography

- [1] G. Ahmadi and M. Shahinpoor. A kinetic model for rapid flows of granular materials. *Int. J. Non-linear Mechanics*, 19(2):177–186, 1983.
- [2] Jean-Luc Aider, Nathalie Sommer, Tareck Raafat, and Jean-Pierre Hulin. Experimental study of a granular flow in a vertical pipe: A spatiotemporal analysis. *Phys. Rev. E*, 59:778, 1998.
- [3] R. Albert, M. A. Pfeifer, A.-L. Barabási, and P. Schiffer. Slow drag in a granular medium. *Phys. Rev. Lett.*, 82(1):205, 1999.
- [4] Y. Amarouchene, J.F. Boudet, and H. Kellay. Dynamic sand dunes. *Phys. Rev. Lett*, 86:4286, 2001.
- [5] John D. Anderson. *Modern Compressible Flow with Historical Perspective*. McGraw-Hill, Boston, 1990.
- [6] Michel Assenheimer and Victor Steinberg. Rayleigh-bénard convection near the gas-liquid critical point. *Phys. Rev. Lett.*, 70:3888, 1993.
- [7] R. A. Bagnold. Experiments on a gravity-free dispersion of large solid spheres in a Newtonian fluid under shear. *Proc. Royal Soc. London*, 49:225, 1954.

- [8] R.P. Behringer. Rayleigh-bénard convection and turbulence in liquid helium. *Rev. Mod. Phys.*, 57:657, 1985.
- [9] C. Bizon, M. D. Shattuck, J. R. de Bruyn, J. B. Swift, W. D. McCormick, and Harry L. Swinney. Convection and diffusion in patterns in oscillated granular media. *J. Stat. Phys.*, 93(3/4):449, 1998. Color pictures of granular convection can be found at <http://chaos.ph.utexas.edu/errata/bizon98a.html>.
- [10] C. Bizon, M. D. Shattuck, and J. B. Swift. Linear stability analysis of a vertically oscillated granular layer. *Phys. Rev. E*, 60(6B):7210, 1999.
- [11] C. Bizon, M. D. Shattuck, J. B. Swift, W. D. McCormick, and Harry L. Swinney. Patterns in 3D vertically oscillated granular layers: Simulation and experiment. *Phys. Rev. Lett.*, 80:57–60, 1998.
- [12] C. Bizon, M. D. Shattuck, J. B. Swift, and Harry L. Swinney. Velocity correlations in driven two-dimensional granular media. In J. Karkheck, editor, *Dynamics: Models and Kinetic Methods for Nonequilibrium Many-Body Systems (in press)*, NATO ASI Series E: Applied Sciences, Dordrecht, 2000. Kluwer Academic publishers.
- [13] L. Bocquet, W. Losert, D. Schalk, T.C. Lubensky, and J.P. Gollub. Granular shear flow dynamics and forces:experiment and continuum theory. *Phys. Rev. E.*, 65:011307, 2001.
- [14] J. Bougie, S. J. Moon, J. B. Swift, and Harry L. Swinney. Shocks in vertically oscillated granular layers. *Phys. Rev. E*, 66:1–9, 2002.

- [15] A.P.J. Breu, H.-M. Ensner, C.A. Kruelle, and I Rehberg. Reversing the Brazil-nut effect: competition between percolation and condensation. *Phys. Rev. Lett.*, 90(4):014302, 2003.
- [16] J. Javier Brey, James W. Dufty, and Andrés Santos. Dissipative dynamics for hard spheres. *J. Stat. Phys.*, 87(5/6):1051, 1997.
- [17] J.J. Brey, M.J. Ruiz-Montero, and F. Moreno. Boundary conditions and normal state for a vibrated granular fluid. *Phys. Rev. E*, 62:5339, 2000.
- [18] Volkhard Buchholtz and Thorsten Pöschel. Interaction of a granular stream with an obstacle. *Granular Matter*, 1:33–41, 1998.
- [19] Teodor Burghilea and Victor Steinberg. Onset of wave drag due to generation of capillary-gravity waves by a moving object as a critical phenomenon. *Phys. Rev. Lett.*, 86(12):2557, 2001.
- [20] F. H. Busse and J. A. Whitehead. Instabilities of convection rolls in a high Prandtl number fluid. *J. Fluid Mech.*, 47:305, 1971.
- [21] C. S. Campbell. Rapid granular flows. *Annu. Rev. Fluid Mech.*, 2:57–92, 1990.
- [22] E. Cerda, F. Melo, and S. Rica. Model for subharmonic waves in granular materials. *Phys. Rev. Lett.*, 79(23):4570–4573, 1998.

- [23] D. Chehata, R. Zenit, and C.R. Wassgren. Dense granular flow around an immersed cylinder. *Physics of Fluids*, 15:1622, 2003.
- [24] F. Chevy and E. Raphaël. Capillary gravity waves: A “fixed-depth analysis”. *Europhys. Lett.*, 61(6):796, 2003.
- [25] Kiam Choo, Michael W. Baker, T. C. A. Molteno, and Stephen W. Morris. The dynamics of granular segregation patterns in a long drum mixer. *Phys. Rev. E*, 58.
- [26] C.A. Coulomb. *Memoires de Mathematiques et de Physique Presentes a l’Academie Royale des Sciences par Divers Savans et Lus dans les Assemblies*, page 343. L’imprimerie Royale, Paris, 1773.
- [27] D.R. Criswell, J.F. Lindsay, and D.L. Reasoner. Seismic and acoustic emissions of a booming sand dune. *Journal of Geophysical Research*, 80:4693, 1975.
- [28] J. Crocker and D.G. Grier. Methods of digital video microscopy for colloidal studies. *Journal of Colloid and Interface Science*, 179:298–310, 1996.
- [29] M. C. Cross and P. C. Hohenberg. Pattern formation outside of equilibrium. *Rev. Mod. Phys.*, 65:851–1112, 1993.
- [30] G.N. Curzon. *Tales of Travel*. Geprge H. Duran, 1923.

- [31] John R. de Bruyn, C. Bizon, M. D. Shattuck, D. Goldman, J. B. Swift, and Harry L. Swinney. Continuum-type stability balloon in oscillated granular layers. *Phys. Rev. Lett.*, 81:1421–1424, 1998.
- [32] John R. de Bruyn, B. C. Lewis, M. D. Shattuck, J. B. Swift, and Harry L. Swinney. Spiral patterns in oscillated granular layers. *Phys. Rev. E*, 63:041305, 2001.
- [33] P. G. de Gennes. Granular matter: a tentative view. *Rev. Mod. Phys.*, 71(2):S374–S382, 1999.
- [34] E. Dubois-Violette, G. Dunrand, E. Guyon, P. Manneville, and P. Pieranski. Instabilities in nematic liquid crystals. In L. Liebert, editor, *Liquid Crystals*, page 147. Academic Press, New York, 1978.
- [35] J. Duran. *Sands, Powders, and Grains: An Introduction to the Physics of Granular Materials*. Springer, Berlin, 2000.
- [36] Jens Eggers and Hermann Riecke. Continuum description of vibrated sand. *Phys. Rev. E*, 59(4):4476, 1999.
- [37] Bryan J. Ennis, John Green, and Reg Davies. The legacy of neglect in the U.S. *Chemical Engineering Progress*, 90:32–43, 1994.
- [38] P. Evesque. Shaking dry powders and grains. *Contemporary Physics*, 33(4):245–261, 1992.

- [39] P. Evesque and J. Rajchenbach. Convective instability in a cohesionless glass bead packing. *C. R. Acad. Sci. Ser. II (Paris)*, 307:223, 1988.
- [40] M. Faraday. On a peculiar class of acoustical figures; and on certain forms assumed by groups of particles upon vibrating elastic surfaces. *Philos. Trans. R. Soc. London*, 121:299–340, 1831.
- [41] Y. Forterre and O. Pouliquen. Longitudinal vortices in granular flows. *Phys. Rev. Lett.*, 86:5886, 2001.
- [42] A.F. Fortes, D.D. Joseph, and T.S. Lundgren. Nonlinear mechanics of fluidization of beds of spherical particles. *J. Fluid Mech.*, page 177:467, 1987.
- [43] I. Goldhirsch. Rapid granular flows. *Annu. Rev. Fluid. Mech.*, 35:267–293, 2003.
- [44] Isaac Goldhirsch. Scales and kinetics of granular flows. *Chaos*, 9:659, 1999.
- [45] D. I. Goldman, J. B. Swift, and Harry L. Swinney. Noise, coherent fluctuations, and the onset of order in an oscillated granular layer. *Phys. Rev. Lett.*, 92:174302, 2004.
- [46] A. Goldshtein, A. Alexeev, and M. Shapiro. Shock waves in granular gases. In T. Poschel and N. Brilliantov, editors, *Granular Gas Dynamics*, pages 188–225. Springer, Berlin, 2003.

- [47] A. Goldshtein, M. Shapiro, and C. Gutfinger. Mechanics of collisional motion of granular materials. Part 4. Expansion wave. *J. Fluid Mech.*, 327:117–138, 1996.
- [48] Alexander Goldshtein and Michael Shapiro. Mechanics of collisional motion of granular materials. Part 1. General hydrodynamic equations. *J. Fluid Mech.*, 282:75–114, 1995.
- [49] Alexander Goldshtein, Michael Shapiro, Leonid Moldavsky, and Mati Fichman. Mechanics of collisional motion of granular materials. Part 2. Wave propagation through vibrofluidized granular layers. *J. Fluid Mech.*, 287:349–382, 1995.
- [50] W. Goldsmith. *Impact*. Edward Arnold Ltd., London, 1960.
- [51] J.M.N.T. Gray, Y.C. Tai, and S. Noelle. Shock waves, dead zones and particle free regions in rapid granular free surface flows. *J. Fluid Mech.*, 491:161, 2003.
- [52] P. K. Haff. Grain flow as a fluid-mechanical phenomenon. *J. Fluid Mech.*, 134:401–430, 1983.
- [53] T.H. Havelock. The propagation of groups of waves in dispersive media, with application to waves on water produced by a traveling disturbance. *Proc. Royal Soc. London A*, 81(549):398–430, 1908.
- [54] H. Hermann, J. P. Hovi, and S. Luding, editors. *Physics of Dry Granular Media*. Kluwer Academic Publishers, Dordrecht, 1998.

- [55] S. Hørluck and P. Dimon. Statistics of shock waves in a two-dimensional granular flows. *Phys. Rev. E*, 60(1):671, 1999.
- [56] S. Horluck and P. Dimon. Grain dynamics in a two-dimensional granular flow. *Phys. Rev. E*, 63:031301, 2001.
- [57] S. Horluck, M. van Hecke, and P. Dimon. Shock waves in two-dimensional granular flow: Effects of rough walls and polydispersity. *Phys. Rev. E.*, 67:021304, 2003.
- [58] H. M. Jaeger, Chu-heng Liu, and Sidney R. Nagel. Relaxation at the angle of repose. *Phys. Rev. Lett.*, 62:40–43, 1989.
- [59] H. M. Jaeger, S. R. Nagel, and R. P. Behringer. Granular solids, liquids, and gases. *Reviews Modern Physics*, 68:1259–1274, 1996.
- [60] J. V. Jelley. *Cerenkov Radiation and Its Applications*. Pergamon Press, New York, 1958.
- [61] J. T. Jenkins. Boundary conditions for rapid granular flow: Flat, frictional walls. *Transactions of the ASME*, 59:120, 1992.
- [62] J. T. Jenkins and E. Askari. Boundary conditions for rapid granular flows: phase interfaces. *J. Fluid Mech.*, 223:497–508, 1991.
- [63] J. T. Jenkins and M. W. Richman. Grad’s 13-moment system for a dense gas of inelastic particles. *Arch. Rat. Mech. Anal.*, 87:355–377, 1985.



- [64] James T. Jenkins and Michel Y. Louge. On the flux of fluctuational energy in a collisional grain flow at a flat, frictional wall. *Phys. Fluids*, 9(10):2835, 1997.
- [65] J.T. Jenkins and E. Askari. Hydraulic theory for a debris flow supported on a collisional shear layer. *Chaos*, 9(3):654–658, 1999.
- [66] Leo P. Kadanoff. Built upon sand: Theoretical ideas inspired by the flow of granular materials. *Rev. Mod. Phys.*, 71(1):435–444, 1999.
- [67] V. Kamenetsky, A. Goldshtein, M. Shapiro, and D. Degani. Evolution of a shock wave in a granular gas. *Physics of Fluids*, 12(11):3036, 2000.
- [68] A. Kudrolli and J. P. Gollub. Patterns and spatiotemporal chaos in parametrically forced surface waves: a systematic survey at large aspect ratio. *Physica D*, 97:133–154, 1996.
- [69] A. Kudrolli and J. Henry. Non-gaussian velocity distributions in excited granular matter in the absence of clustering. *Phys. Rev. E*, 62(2):1489, 2000.
- [70] L.D. Landau. On shock waves at large distances from the place of their origin. In D. Ter Haar, editor, *Collected Papers of L.D. Landau*, pages 437–444. Pergamon Press, 1965.
- [71] L.D. Landau and E.M. Lifshitz. *Fluid Mechanics*. Pergamon Press, Oxford, 1959.

- [72] Kurt Liffman, Guy Metcalf, and Paul Cleary. Granular convection and transport due to horizontal shaking. *Phys. Rev. Lett.*, 79(23):4574, 1997.
- [73] A. Lorenz, C. Tuozzolo, and M.Y. Louge. Measurements of impact properties of small, nearly spherical particles. *Experimental Mechanics*, 37:292, 1997.
- [74] W. Losert, L. Bocques, T.C. Lubensky, and J.P. Gollub. Particle dynamics in sheared granular matter. *Phys. Rev. Lett.*, 85:1428, 2000.
- [75] S. Luding, E. Clément, A. Blumen, J. Rajchenbach, and J. Duran. Anomalous energy dissipation in molecular-dynamics simulations of grains: The “detachment effect”. *Phys. Rev. E*, 50(5):4113–4120, 1994.
- [76] S. Luding, E. Clément, A. Blumen, J. Rajchenbach, and J. Duran. Studies of columns of beads under external vibrations. *Phys. Rev. E*, 49(2):1634–1646, 1994.
- [77] S. Luding, M. Huthmann, S. McNamara, and A. Zippelius. How to handle the inelastic collapse of a dissipative hard-sphere gas with the tc model. *Phys. Rev. E*, 58:3416, 1998.
- [78] C. K. K. Lun. A simple kinetic theory for granular flow of rough inelastic spherical particles. *J. Appl. Mech.*, 54:47, 1987.

- [79] Francisco Melo, Paul Umbanhowar, and Harry L. Swinney. Transition to parametric wave patterns in a vertically oscillated granular layer. *Phys. Rev. Lett.*, 72:172–175, 1994.
- [80] Francisco Melo, Paul B. Umbanhowar, and Harry L. Swinney. Hexagons, kinks, and disorder in oscillated granular layers. *Phys. Rev. Lett.*, 75(21):3838–3841, 1995.
- [81] F.S. Merkt, R.D. Deegan, D.I. Goldman, E.C. Rericha, and H.L. Swinney. Persistent holes in a fluid. *Phys. Rev. Lett.*, 92:184501, 2004.
- [82] Sung Joon Moon, D. I. Goldman, J. B. Swift, and Harry L. Swinney. Role of friction in pattern formation in oscillated granular layers. *Phys. Rev. E*, 69:031301, 2004.
- [83] Sung Joon Moon, M. D. Shattuck, and J. B. Swift. Velocity distributions and correlations in homogeneously heated granular media. *Phys. Rev. E*, 64:31303, 2001.
- [84] M. G. Moore, A. Juel, J. M. Burgess, W. D. McCormick, and H. L. Swinney. Fluctuations and pinch-offs observed in viscous fingering. In I. Visarath, L. Kocarev, T. L. Carroll, B. J. Gluckman, S. Boccaletti, and J. Kurths, editors, *Proceedings of the Seventh Experimental Chaos Conference*, page preprint. 2004.
- [85] D.M. Mueth, G.F. Debregeas, G.S. Karczmar, P.J. Eng, S.R. Nagel, and H.M. Jaeger. Signatures of granular microstructure in dense shear flows.

- Nature*, 406:385–389, 2000.
- [86] Nicolás Mujica and Francisco Melo. Solid-liquid transition and hydrodynamic surface waves in vibrated granular layers. *Phys. Rev. Lett.*, 80(23):5121, 1998.
- [87] T. Mullin. Coarsening of self-organized clusters in binary mixtures of particles. *Phys. Rev. Lett.*, 84:4741, 2000.
- [88] M. Newey, S. Van der Meer, J. Ozik, E. Ott, and W. Losert. Band-in-band segregation of multidisperse granular mixtures. *Europhys. Lett.*, 2003.
- [89] J. Oh and G. Alhers. Thermal-noise effect on the transition to rayleigh-bénard convection. *Phys. Rev. Lett.*, 91:094501, 2003.
- [90] A. Okabe, B. Boots, and K. Sugihara. *Spatial Tessellations*. John Wiley & Sons, New York, 1992.
- [91] J.S. Olafsen and Jeffery S. Urbach. Velocity distributions and density fluctuations in a granular gas. *Phys. Rev. E*, 60(3):4268, 1999.
- [92] Luc Oriat and Eric Lanitz. Subpixel detection of the center of an object using a spectral phase algorithm on the image. *Pattern Recognition*, 31(6):761–771, 1998.
- [93] T. Owada. Structure of normal shock waves: Direct numerical analysis of the boltzmann equation for hard-sphere molecules. *Phys. Fluids A.*, 5(1):217, 1992.

- [94] H. K. Pak, E. Van Doorn, and R. P. Behringer. Effects of gases on granular materials under vertical vibration. *Phys. Rev. Lett.*, 74:4643–4646, 1995.
- [95] B. Plapp. Private communicatoin.
- [96] Thorsten Pöschel. Granular material flowing down an inclined chute: a molecular dynamics simulation. *J. Phys. II France*, 3:27–40, 1993.
- [97] Q. Quyang and H.L. Swinney. Transition from a uniform state to hexagonal and striped turing patterns. *Nature*, 352:610–612, 1991.
- [98] J. Rajchenbach. Granular flows. *Advances in Physics*, 49:229–256, 2000.
- [99] E. Raphaël and P.-G. de Gennes. Capillary gravity waves caused by a moving disturbance: wave resistance. *Phys. Rev. E*, 53(4):3448, 1996.
- [100] P.M. Reis and T. Mullin. Granular segregation as a critical phenomenon. *Phys. Rev. Lett.*, 89:244301, 2002.
- [101] E. C. Rericha, C. Bizon, M. D. Shattuck, and Harry L. Swinney. Shocks in supersonic sand. *Phys. Rev. Lett.*, 88:014302–1–4, 2002.
- [102] O. Reynolds. On the dilatency of media composed of rigid particles in contact. *Phil. Mag.*, 20:469–481, December 1885.
- [103] P.J. Roache. *Computational Fluid Dynamics*. Hermosa Publishers, Albuquerque, 1976.

- [104] A. Rosato, K. J. Strandburg, F. Prinz, and R. H. Swendsen. Why the Brazil nuts are on top: Size segregation of particulate matter by shaking. *Phys. Rev. Lett.*, 58(10):1038–1040, 1987.
- [105] Daniel H. Rothman. Oscillons, spiral waves, and stripes in a model of vibrated sand. *Phys. Rev. E*, 57(2):R1239–42, 1998.
- [106] F. Rouyer and N. Menon. Velocity fluctuations in a homogeneous 2d granular gas in steady state. *Phys. Rev. Lett.*, 85(17):3676, 2000.
- [107] Hidetsugu Sakaguchi and Helmut R. Brand. Standing wave localized squares in pattern-forming nonequilibrium systems. *J. de Phys. II*, 7(10):1325–30, 1997.
- [108] S.B. Savage and K. Hutter. The dynamics of avalanches of granular materials from initiation to runout. part i: analysis. *Acta Mechanica*, 86:201–223, 1991.
- [109] Stuart B. Savage. Streaming motions in a bed of vibrationally fluidized dry granular material. *J. Fluid Mech.*, 194:457–478, 1988.
- [110] N. Sela, I. Goldhirsch, and S. H. Noskowicz. Kinetic theoretical study of a simply sheared two-dimensional granular gas to Burnett order. *Phys. Fluids*, 8(9):2337–2353, 1996.
- [111] M.D. Shattuck. New boundary conditions for granular fluids. *preprint*, 2004.

- [112] Troy Shinbrot. Competition between randomizing impacts and inelastic collisions in granular pattern formation. *Nature*, 389(6651):574–6, 1997.
- [113] L.E. Silbert, G.S. Grest, and S.J. Plimpton. Boundary effects and self-organization in dense granular flows. *Phys. Fluids*, 14(8):2637–2646, 2002.
- [114] R. Soto and M.M. Mansour. Granular systems on a vibrating wall: the hydrodynamic boundary condition. *Physica A*, 327:88–93, 2003.
- [115] M. Stenberg and K. Nilsson. Fast tracking of point-symmetric objects. *Proc. SPIE San Jose*, 3028:38–47, 1997.
- [116] J.J. Stoker. *Water waves*. institute of mathematical sciences, New York University, New York, 1957.
- [117] J. Swift and P.C. Hohenberg. Hydrodynamic fluctuation at the convective instability. *Phys. Rev. A*, 15:319, 1977.
- [118] Harry L. Swinney and E.C. Rericha. Pattern formation and shock waves in granular gases. In F. Mallamace and E. Stanley, editors, *The Physics of Complex Systems (New Advances and Perspectives)- The International School of Physics Enrico Fermi*,. Italian Physical Society, 2004.
- [119] M-L. Tan and I. Goldhirsch. Rapid granular flows as mesoscopic systems. *Phys. Rev. Lett.*, 81(14):3022, 1998.

- [120] Sarath G. K. Tennakoon and R. P. Behringer. Vertical and horizontal vibration of granular materials: Coulomb friction and a novel switching state. *Phys. Rev. Lett.*, 81(4):794–797, 1998.
- [121] Lev Tsimring and Igor Aronson. Localized and cellular patterns in a vibrated granular layer. *Phys. Rev. Lett.*, 79(2):213–216, 1997.
- [122] Paul B. Umbanhowar, Francisco Melo, and Harry L. Swinney. Periodic, aperiodic, and transient patterns in vibrated granular layers. *Physica A*, 249:1–9, 1998.
- [123] L. vanel, D. Howell, D. Clark, R.P. Behringer, and E. Clement. Memories in sand: Experimental tests of construction history on stress distributions under sandpiles. *Phys. Rev. E*, 60:R5040, 1999.
- [124] C. T. Veje, Daniel W. Howell, and R. P. Behringer. Kinematics of a two-dimensional granular Couette experiment at the transition to shearing. *Phys. Rev. E*, 59(1):739, 1999.
- [125] C.T. Veje and P. Dimon. Two-dimensional granular flow in a small-angle funnel. *Physical Review E*, 54:4329, 1996.
- [126] Shankar C. Venkataramani and Edward Ott. Spatio-temporal bifurcation phenomena with temporal period doubling: patterns in vibrated sand. *Phys. Rev. Lett.*, 80:3498, 1998.



- [127] O. R. Walton. Numerical simulation of inelastic, frictional particle-particle interactions. In M. C. Roco, editor, *Particulate Two-Phase Flow*, pages 884–911. Butterworth-Heinemann, Boston, 1993.
- [128] S. Warr, G.T.H. Jacques, and J.M. Huntley. Tracking the translational and rotational motion of granular particles: use of high-speed photography and image processing. *Powder Technology*, 81:41–56, 1994.
- [129] C.R. Wassgren, J.A. Cordova, R. Zenit, and A. Karion. Dilute granular flow around an immersed cylinder. *Phys. Fluids*, 15(11):3318, 2003.
- [130] K. Wieghardt. Forces in granular flow. *Mech. Res. Comm.*, 1:3–7, 1974.
- [131] Mingming Wu, Guenter Ahlers, and David S. Cannell. Thermally induced fluctuations below the onset of Rayleigh-Bénard convection. *Phys. Rev. Lett.*, 75(9):1743, 1995.
- [132] J. Von Zan, J. Kreft, D. Goldman, D. Miracle, J.B. Swift, and H. Swinney. Crucial role of sidewalls in velocity distributions in quasi-2d granular gases. *preprint*, 2004.
- [133] T. Zhou and L. P. Kadanoff. Inelastic collapse of three particles. *Phys. Rev. E*, 54(1):623–628, 1996.
- [134] O. Zik, J. Stavans, and Y. Rabin. Mobility of a sphere in vibrated granular media. *Europhys. Lett.*, 17:315–319, 1992.

## Vita

Erin Colleen Rericha was born in Dallas, Texas on May 1, 1975, the son of David M. Rericha and Mary Ann Rericha. She received the Bachelor of Science degree in Physics from Texas A&M University. She was accepted and began graduate studies at the University of Texas in 1997. Erin had a great time in graduate school and is looking forward to future endeavors.

Permanent address: 1513 Pease Rd Apt. 4  
Austin, Texas 78758

This dissertation was typeset with  $\text{\LaTeX}^\dagger$  by the author.

---

<sup>†</sup> $\text{\LaTeX}$  is a document preparation system developed by Leslie Lamport as a special version of Donald Knuth's  $\text{\TeX}$  Program.